

UNIVERSITY OF BRASILIA  
FACULTY OF TECHNOLOGY  
DEPARTMENT OF ELECTRICAL ENGINEERING

HITLESS RATE AND BANDWIDTH SWITCHING IN  
DYNAMICALLY RECONFIGURABLE COHERENT  
OPTICAL SYSTEMS

VALERY NOBL ROZENTAL

ADVISOR: DARLI AUGUSTO DE ARRUDA MELLO

DOCTORAL THESIS IN  
ELECTRICAL ENGINEERING

PUBLICATION: PPGENE.TD - 107/16

BRASILIA/DF: JANUARY - 2016.



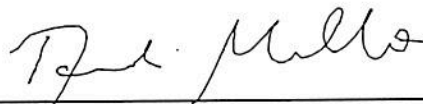
UNIVERSIDADE DE BRASÍLIA FACULDADE DE  
TECNOLOGIA DEPARTAMENTO DE  
ENGENHARIA ELÉTRICA

HITLESS RATE AND BANDWIDTH SWITCHING IN DYNAMICALLY  
RECONFIGURABLE COHERENT OPTICAL SYSTEMS

VALERY NOBL ROZENTAL

TESE DE DOUTORADO SUBMETIDA AO DEPARTAMENTO DE ENGENHARIA ELÉTRICA DA  
FACULDADE DE TECNOLOGIA DA UNIVERSIDADE DE BRASÍLIA, COMO PARTE DOS  
REQUISITOS NECESSÁRIOS PARA A OBTENÇÃO DO GRAU DE DOUTOR.

APROVADA POR:



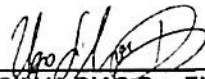
---

DARLI AUGUSTO DE ARRUDA MELLO, Dr., ENE/UnB  
(ORIENTADOR)



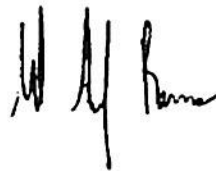
---

ANDRÉ NOLL BARRETO, Dr., ENE/UnB  
(EXAMINADOR INTERNO)



---

UGO SILVA DIAS Dr., ENE/UNB  
(EXAMINADOR INTERNO)



---

MURILO ARAUJO ROMERO, Dr., EESC/USP  
(EXAMINADOR EXTERNO)



---

MIQUEL GARRICH ALABARCE, Dr., CPqD  
(EXAMINADOR EXTERNO)

Brasília, 25 de janeiro de 2016.

## **FICHA CATALOGRÁFICA**

ROZENTAL, VALERY N.

Hitless Rate and Bandwidth Switching in Dynamically Reconfigurable Coherent Optical Systems.

xix, 107p., 297 mm (ENE/FT/UnB, Doutor, Engenharia Elétrica 2016).

Tese de Doutorado -

Universidade de Brasília. Faculdade de Tecnologia.

Departamento de Engenharia Elétrica.

- |                                    |                                      |
|------------------------------------|--------------------------------------|
| 1. Redes ópticas elásticas         | 2. Sistemas ópticos coerentes        |
| 3. Processamento digital de sinais | 4. Transceptores ópticos adaptativos |
| 5. Chaveamento de taxa sem impacto | 6. Redução de consumo de potência    |
| I. ENE/FT/UnB                      | II. Título (série)                   |

## **REFERÊNCIA BIBLIOGRÁFICA**

ROZENTAL N., V. (2016). Hitless Rate and Bandwidth Switching in Dynamically Reconfigurable Coherent Optical Systems.

Tese de Doutorado em Engenharia Elétrica, Departamento de Engenharia Elétrica, Universidade de Brasília, Brasília, DF, 107p.

## **CESSÃO DE DIREITOS**

NOME DO AUTOR: Valery Nobl Rozental.

TÍTULO DA TESE DE DOUTORADO: Hitless Rate and Bandwidth Switching in Dynamically Reconfigurable Coherent Optical Systems.

GRAU / ANO: Doutor / 2016

É concedida à Universidade de Brasília permissão para reproduzir cópias desta tese de doutorado e para emprestar ou vender tais cópias somente para propósitos acadêmicos e científicos. O autor reserva outros direitos de publicação e nenhuma parte desta tese de doutorado pode ser reproduzida sem a autorização por escrito do autor.

---

Valery Nobl Rozental  
Rua do Sol 148, Ed. Margarida 11  
Campinas - SP - Brasil.

## RESUMO

Grande parte de pesquisa em comunicações ópticas visa melhorar a eficiência de rede, otimizando o uso de banda e reduzindo consumo de potência. Os paradigmas emergentes, tais como a grade de frequências flexível, métodos sofisticados de chaveamento óptico e desfragmentação espectral, atribuem propriedades adaptativas para redes futuras, permitindo seu auto-ajuste às condições de transmissão e tráfego variáveis. De fato, as estatísticas de tráfego agregado em pontos de troca de tráfego da Internet exibem fortes flutuações ao decorrer do dia, sendo o valor médio em torno de 70%, e valor mínimo em torno de 20% do valor pico. No entanto, os sistemas ópticos atuais operam o seu lado linha na taxa nominal, o que leva a um elevado consumo de potência, desperdício de recursos espectrais, e saturação prematura de redes. No intuito de suportar as características de redes flexíveis pela camada física, os transceptores ópticos de próxima geração devem ser capazes de ajustar suas taxas de transmissão e ocupação espectral de acordo com as demandas de tráfego variáveis. No entanto, um chaveamento convencional de taxa de transmissão requer interrupção de serviço, altamente indesejável na perspectiva das operadoras.

Neste escopo, as principais contribuições dessa tese são dois métodos de chaveamento *online* sem impacto (*hitless*) da taxa de transmissão, que permitem reduzir o consumo de potência associado ao processamento digital de sinais durante períodos de baixo tráfego. O primeiro método foi desenvolvido para transceptores, cujos moduladores são alimentados por sinais binários combinados eletronicamente, e atende, principalmente, a cenários de alocação estática de banda. Aqui, a redução de taxa é realizada por meio de repetição de símbolos transmitidos, e o bloco equalizador convencional do receptor é substituído por uma estrutura multi-ramo, em que cada ramo da estrutura opera em uma taxa específica. A perda de sincronização durante chaveamento é evitada utilizando a saída do ramo ativo como sequência de treinamento para o ramo destino. O método pode, adicionalmente, atender à alocação dinâmica de banda, contanto que exista um mecanismo de cooperação entre transceptores ópticos e multiplexadores de inserção-extração ópticos reconfiguráveis. Neste caso, o ajuste espectral do sinal pode ser obtido por meio de uma filtragem óptica pelas chaves seletoras de frequência que suportam operação em grade flexível.

O segundo método foi desenvolvido para transceptores com módulos de processamento digital de sinais no lado transmissor. O chaveamento de taxa é obtido por meio de aumento e redução de número de amostras por símbolo transmitido, mantendo fixa a taxa de conversão digital-analógica. Neste caso, uma mudança de taxa de símbolo

implica, também, em um ajuste correspondente da banda do sinal. Assim, o método pode suportar propriedades de alocação dinâmica de banda das redes elásticas. Nós demonstramos que, se o chaveamento de taxa e banda do sinal é realizado em passos intermediários suficientemente pequenos, o equalizador dinâmico do lado receptor consegue acompanhar as mudanças do sinal, mantendo a sincronização do sistema.

O primeiro método foi validado em um arranjo experimental com transmissão a 100 Gb/s de um sinal modulado por chaveamento de fase e quadratura multiplexado em polarização, e processamento digital de sinais *offline*. Ademais, realizamos simulações computacionais extensas, incluindo formatos de modulação por chaveamento de fase e quadratura e modulação de amplitude em quadratura de ordem 16, e investigamos o desempenho do método para sinais não-retorna-a-zero e retorna-a-zero, gerados no domínio óptico, e sinais Nyquist, gerados digitalmente. Os transientes de erros, que aparecem durante chaveamento para taxas mais altas, são evitados usando sequências de treinamento do equalizador suficientemente longas (acima de 40.000 símbolos). O método mostrou-se robusto contra a dispersão dos modos de polarização e ruído de fase dentro de especificações aceitáveis. A principal vantagem deste método é que ele permite reduzir o consumo de potência associado ao processamento digital de sinais para compensação da dispersão cromática. Os resultados mostraram que uma redução pela metade da taxa de símbolos produz uma redução de em torno de 55% na complexidade computacional, devido à elevada duração de símbolo e aprimoramento da qualidade de sinal. Uma redução adicional de taxa para um quarto da taxa nominal permite desligar o equalizador da dispersão cromática, exceto em caso de pulsos Nyquist, em que o ganho em complexidade está em torno de 80%.

O segundo método também foi validado em um arranjo experimental com transmissão a 100 Gb/s de um sinal modulado por chaveamento de fase e quadratura multiplexado em polarização e processamento digital de sinais *offline*, utilizando um conjunto para desenvolvimento do conversor analógico-digital. Ao contrário da proposta anterior, este método suporta alta granularidade com apenas um aumento marginal de complexidade computacional. Os resultados experimentais de redução e aumento de taxa em dez passos discretos não apresentaram transientes de erros, garantindo transmissão ininterrupta. O método pode ser usado para reduzir o consumo de potência devido à redução de vazão de dados após a interpolação do lado receptor. Adicionalmente, o consumo pode ser altamente reduzido em sistemas que suportam múltiplos esquemas de correção de erros, aproveitando o aprimoramento da qualidade do sinal devido à redução de taxa de símbolos. Assim, um código corretor de erros complexo do tipo *soft-decision*, usado na taxa de transmissão nominal, pode ser substituído por um código do tipo *hard-decision*, com complexidade computacional reduzida.

## ABSTRACT

Much of the latest research in optical communications is directed towards increasing network efficiency, optimizing bandwidth usage and reducing power consumption. Emerging paradigms, such as flexible frequency grid, sophisticated optical switching methods and spectral defragmentation, attribute adaptive properties to future networks, enabling them to adjust to the changing transmission and traffic conditions. To support these features, next-generation optical transponders must be capable of adjusting their transmission rate and bandwidth occupation according to the time-varying traffic demands. However, conventional rate-switching requires service interruption, which is highly undesirable from the operators' standpoint.

Our contributions in the proposed thesis consist of two methods for hitless online rate switching that allow to reduce power consumption, associated with digital signal processing, during low traffic periods. The first method is designed for transponders with binary-signal-driven transmit-side modulators, and targets primarily static bandwidth allocation scenarios. Here, rate reduction is achieved by symbol repetition, and a conventional receive-side equalizer block is replaced by a multi-branch structure, where each branch operates at a specific transmission rate. Synchronization loss is avoided by using the output of the active branch as a training sequence for the target-rate branch. The method can also support dynamic bandwidth allocation, provided there is a cooperation mechanism between the optical transponders and the reconfigurable add-drop multiplexers. Here, signal spectral adjustment can be obtained via optical filtering by flex-grid-enabled wavelength-selective switching.

The second method targets transponders with transmit-side digital signal processing. Rate changing is achieved by increasing/reducing the number of samples per transmitted symbol, while maintaining a fixed digital-to-analog conversion rate. Changing the symbol rate also implies in corresponding signal bandwidth adjustment, so that the method can support dynamic bandwidth allocation features of the next-generations elastic optical networks. We show that if the rate and bandwidth switching is performed in sufficiently small discrete intermediate steps, the receive-side dynamic equalizer successfully tracks signal changes, maintaining system synchronism.

## PALAVRAS-CHAVE

- Redes ópticas elásticas
- Sistemas ópticos coerentes
- Processamento digital de sinais
- Transceptores ópticos adaptativos
- Chaveamento de taxa sem impacto
- Redução de consumo de potência



## Contents

<b>1</b>	<b>INTRODUCTION</b>	<b>1</b>
1.1	EVOLUTION OF OPTICAL COMMUNICATIONS . . . . .	1
1.2	TOWARDS FLEXIBLE OPTICAL NETWORKS . . . . .	4
1.3	ADAPTIVE OPTICAL TRANSCEIVERS . . . . .	6
1.3.1	General description . . . . .	6
1.3.2	Conventional versus DSP-capable transmitter architecture for rate-flexible transmission . . . . .	7
1.4	MOTIVATION BEHIND THIS WORK . . . . .	9
1.5	OVERVIEW OF THE RELATED WORK . . . . .	12
1.6	OUR CONTRIBUTIONS AND OUTLINE . . . . .	13
<b>2</b>	<b>OPTICAL TRANSMISSION</b>	<b>15</b>
2.1	THE TRANSMITTER . . . . .	15
2.2	OPTICAL CHANNEL . . . . .	16
2.2.1	Fiber propagation in linear regime . . . . .	16
2.2.2	Fiber propagation in nonlinear regime . . . . .	21
2.3	THE RECEIVER . . . . .	24
<b>3</b>	<b>DIGITAL SIGNAL PROCESSING IN COHERENT OPTICAL RE-</b>	
	<b>CEIVERS</b>	<b>29</b>
3.1	DESKEW . . . . .	30
3.2	ORTHONORMALIZATION . . . . .	31
3.3	CD ESTIMATION . . . . .	32
3.4	CD COMPENSATION . . . . .	34
3.5	SYMBOL SYNCHRONIZATION . . . . .	34
3.5.1	Timing error detector . . . . .	35
3.5.2	Loop filter and NCO . . . . .	37
3.5.3	Interpolator . . . . .	38
3.6	DYNAMIC EQUALIZATION . . . . .	38
3.6.1	DE architecture . . . . .	38

3.6.2	Adaptive equalization . . . . .	39
3.7	CARRIER RECOVERY . . . . .	43
3.7.1	Frequency offset compensation . . . . .	44
3.7.2	Phase noise estimation . . . . .	44
3.8	NONLINEAR IMPAIRMENTS COMPENSATION . . . . .	46
3.8.1	Digital backpropagation . . . . .	47
3.8.2	Split-step Fourier method . . . . .	48
<b>4</b>	<b>DIGITAL-DOMAIN CD COMPENSATION AND COMPLEXITY ANALYSIS</b>	<b>50</b>
4.1	CD EQUALIZER DESIGN . . . . .	50
4.1.1	Equalizer length estimation . . . . .	50
4.1.2	Time-domain equalizer design . . . . .	52
4.1.3	Frequency-domain equalizer design . . . . .	56
4.2	CD COMPENSATION COMPLEXITY ANALYSIS . . . . .	56
4.3	COMPLEXITY GAIN OF THE SYMBOL-REPETITION-BASED RATE SWITCHING . . . . .	58
4.3.1	Simulation setup . . . . .	59
4.3.2	Results and discussion . . . . .	60
<b>5</b>	<b>RATE SWITCHING IN COHERENT OPTICAL SYSTEMS WITH CONVENTIONAL TRANSMITTERS</b>	<b>67</b>
5.1	OPERATION PRINCIPLE . . . . .	67
5.2	SYMBOL REPETITION FOR DIFFERENT PULSE SHAPES . . . . .	69
5.2.1	Non-return-to-zero pulses . . . . .	69
5.2.2	Return-to-zero pulses . . . . .	70
5.2.3	Nyquist pulses . . . . .	71
5.3	RATE SWITCHING INVESTIGATION BY COMPUTER SIMULATIONS . . . . .	73
5.3.1	Simulation setup . . . . .	73
5.3.2	Results and discussion . . . . .	74
5.4	EXPERIMENTAL VALIDATION . . . . .	77
5.4.1	Experimental Setup . . . . .	77
5.4.2	Results and discussion . . . . .	79
<b>6</b>	<b>RATE AND BANDWIDTH SWITCHING IN COHERENT OPTICAL SYSTEMS WITH DSP-CAPABLE TRANSMITTERS</b>	<b>82</b>
6.1	OPERATION PRINCIPLE . . . . .	82

6.1.1	Synchronous rate switching architecture . . . . .	82
6.1.2	Small-step outage mitigation . . . . .	83
6.2	EXPERIMENTAL SETUP AND PROCEDURE . . . . .	86
6.3	RESULTS AND DISCUSSION . . . . .	87
6.4	BANDWIDTH ADJUSTMENT FOR NETWORK OPTIMIZATION .	90
6.5	IMPLEMENTATION CONSIDERATIONS . . . . .	91
<b>7</b>	<b>CONCLUSION</b>	<b>95</b>
	<b>REFERENCES</b>	<b>97</b>

## List of Tables

4.1	Simulation parameters for CD compensation complexity analysis. . . .	59
4.2	Computational complexity for CD equalization [Tops/s]; $N_{\text{FFT}} = 8192$ ; Accumulated CD = 70 ns/nm; BER = $3.8 \times 10^{-3}$ . . . . .	65
4.3	Computational complexity for CD equalization [Tops/s]; $N_{\text{FFT}} = 4096$ ; Accumulated CD = 70 ns/nm; BER = $3.8 \times 10^{-3}$ . . . . .	65
4.4	Computational complexity for CD equalization [Tops/s]; $N_{\text{FFT}} = 8192$ ; Accumulated CD = 70 ns/nm; No penalty operation. . . . .	65
4.5	Computational complexity for CD equalization [Tops/s]; $N_{\text{FFT}} = 4096$ ; Accumulated CD = 70 ns/nm; No penalty operation. . . . .	65
5.1	Simulation parameters for repetition-based rate switching numeric in- vestigation. . . . .	73
5.2	Lengths of the bulk equalizers [taps]. . . . .	78
6.1	Rate and bandwidth adjustment exemplary parameters. . . . .	92

## List of Figures

1.1	Capacity $\times$ distance evolution of optical systems: Roman numerals indicate system generation; MMF – multi-mode fiber; SMF – single-mode fiber; EDFA – erbium-doped fiber amplifier; WDM – wavelength division multiplexing; DM – chromatic dispersion management; FEC – forward error correction; Raman amp. – Raman amplification; Pol-mux – polarization multiplexing; DSP – digital signal processing; Space-Div-Mux – space division multiplexing. . . . .	3
1.2	Adaptive optical transceiver. . . . .	6
1.3	Multilevel optical signal generation. MZM: Mach-Zehnder modulator; PBC: polarization beam combiner. . . . .	7
1.4	a) Daily and (b) weekly statistics of the aggregate Internet traffic between autonomous systems in Brazil [33]. . . . .	10
1.5	Aggregate traffic at the London Internet Exchange point (LINX) [34]. . . . .	11
2.1	Single-carrier transmitter processing block diagram. . . . .	15
2.2	Intersymbol interference produced by CD. . . . .	18
2.3	Pulse spreading and polarization plane rotation due to birefringence. . . . .	20
2.4	Coherent quadrature receiver. . . . .	25
2.5	Polarization-diversity receiver. . . . .	27
3.1	Chain of coherent receiver DSP algorithms for information recovery. . . . .	29
3.2	Sample mapping for GTED-based CD estimation. . . . .	32
3.3	Digital timing recovery system. ADC – analog-to-digital converter; NCO – numerically-controlled oscillator; TED – timing error detector (Adapted from [79,85]). . . . .	35
3.4	Operating principle of the GTED: (a) correct sampling ( $\Delta\tau = 0$ ); (b) late sampling ( $\Delta\tau > 0$ ); advanced sampling ( $\Delta\tau < 0$ ). . . . .	36
3.5	Typical S-curve. . . . .	36
3.6	PI controller of the loop filter. . . . .	37
3.7	$2 \times 2$ MIMO “butterfly”-structured dynamic equalizer. . . . .	39

3.8	Skew compensating DE structures: (a) real $4 \times 4$ MIMO [89]; (b) complex $4 \times 2$ MIMO [90]. . . . .	39
3.9	Blind phase search algorithm. (a) Block diagram; (b) Test block internal architecture. . . . .	46
4.1	Tap weights of an MSE-based dynamic equalizer for different pulse shapes: (a) NRZ; (b) RZ with 50% duty cycle; (c) Nyquist with roll-off factor = 0.2. . . . .	52
4.2	(a) Tap weights of a TD CD equalizer, designed using Equation (4.9); (b) Phase response for $N_{CD} = N_{max}$ and $N_{CD} = 3N_{max}$ . . . . .	54
4.3	Time-domain CD equalizer magnitude (left column) and group delay (right column) response for: (a,b) 50-km propagation; (c,d) 500-km propagation; (e,f) 1500-km propagation. . . . .	55
4.4	a) FFT size optimization for $N_{CD} = 340$ ; (b) Optimal FFT size vs. overlap. . . . .	58
4.5	Simulation setup for overlap impact investigation. . . . .	60
4.6	BER versus overlap size of the FD CD equalizer at 28 GBd for (a) NRZ-, (b) 50% duty cycle RZ-, and (c) Nyquist RC-shaped signals. . . . .	61
4.7	BER versus overlap size of the FD CD equalizer at 14 GBd for (a) NRZ-, (b) 50% duty cycle RZ-, and (c) Nyquist RC-shaped signals. . . . .	62
4.8	BER versus overlap size of the FD CD equalizer at 7 GBd for (a) NRZ-, (b) 50% duty cycle RZ-, and (c) Nyquist RC-shaped signals. . . . .	63
5.1	Receive-side DSP block architecture for symbol-repetition-based rate switching. . . . .	68
5.2	Rate switching sequence. . . . .	69
5.3	Rate switching sequence. . . . .	70
5.4	Effect of the anti-aliasing lowpass filter on RZ signals. . . . .	71
5.5	Nyquist-shaped symbols with: (a) x2 repetitions, (b) x4 repetitions. Power spectral density: (c) without symbol repetition, (d) x2 repetitions, (e) x4 repetitions. . . . .	71
5.6	Bandwidth adjustment scheme for conventional Tx systems. AWG – arrayed waveguide grating; PS – power splitter; WSS – wavelength-selective switch. Insets: (a) PSD at the Tx output; (b) PSD after optical-domain spectral shaping. . . . .	72
5.7	OSNR X BER reference curves (before rate switching): (a) NRZ, (b) RZ 50%, (c) Nyquist; (d) Laser linewidth <i>versus</i> BER. . . . .	75

5.8	Error transients for a 7 → 14 GBd switching of an RZ-shaped 16QAM signal for different lengths training periods: (a) 5,000 symbols; (b) 10,000 symbols; (c) 20,000 symbols; (d) 40,000 symbols. . . . .	76
5.9	Symbol-repetition-based rate switching robustness against DGD for NRZ (a,b); RZ 50% (c,d); and Nyquist (e,f) pulses. Left column (a,c,e): B1→B2→B1 GBd switching. Right column (b,d,f): B2→B3→B2 GBd switching. OSNR = 14 dB for QPSK; OSNR = 20 dB for 16QAM. . . . .	77
5.10	Experimental setup for validation of rate switching in conventional Tx systems. . . . .	78
5.11	(a) Switching pattern observation in a single capture of a real-time oscilloscope. (b) Power spectral density traces of individual sequences, as captured by OSA. . . . .	80
5.12	BER versus low-pass filter length: (a) Baseline performance for individual sequences in a B2B scenario – BER averaged over 10 data captures; BER for the rate switching pattern 28→14→7→14→28 GBd for (b) CD = 10 ns/m; (c) CD = 20 ns/m; (d) CD = 30 ns/m; (e) CD = 40 ns/m; (f) CD = 50 ns/m. Solid lines indicate results after down-switching, and dashed lines indicate results after up-switching. . . . .	81
6.1	(a) DSP for rate switching transmitter. Insets: real part of an arbitrary 16QAM signal (blue); same signal portion after upsampling by factor of 1.5 (red) . . . . .	83
6.2	Electrical bandwidth of the interpolator-produced raised-cosine-shaped 32-, 24- and 16-GBd QPSK signals. . . . .	83
6.3	Simulation results of 16 to 32 GBd single-step switching for a PM-16QAM signal: (a) temporal evolution of X-pol. in-phase signal component; (b) The EVM computed over 100 symbols. . . . .	84
6.4	Simulation results of 16 to 32 GBd 10-step switching for a PM-16QAM signal: (a) temporal evolution of X-pol. in-phase signal component; (b) The EVM computed over 100 symbols. . . . .	85
6.5	Experimental setup for validation of rate switching in DSP-capable Tx systems. . . . .	86
6.6	Experimental procedure for sequence alignment. . . . .	87
6.7	X-pol I component at OSNR = 16 dB for (a) 32→16 GBd switching and (b) 16→32 GBd switching. . . . .	88
6.8	100-symbol averaged EVM for (c) 32→16 and (d) 16→32 GBd. . . . .	89
6.9	Individual constellation plots for (a) 32 and (b) 16 GBd; (c) PSD at the receiver for 32 and 16 GBd. . . . .	89

6.10	Bandwidth release/allocation using symbol rate switching & push-pull defragmentation. (a) Nominal rate operation no available bandwidth between N4-N5 for service request C. (b) Symbol rate reduction induces reduction of the occupied bandwidth. (c) Push-pull defragmentation releases bandwidth for service request C. Inset: aggregate traffic at the London Internet Exchange point (LINX) [34]. . . . .	90
6.11	Interpolation of a single sample at $t_\mu$ from four data samples by a 3 <sup>rd</sup> order polynomial. . . . .	91
6.12	Interpolation of a single sample at $t_\mu$ from four data samples by a 3 <sup>rd</sup> order polynomial. . . . .	93
6.13	Farrow structure for 3 <sup>rd</sup> -order polynomial interpolator (adapted from [121]). . . . .	94



## LIST OF ACRONYMS

AD	<i>Analog to Digital</i>
ADC	<i>Analog to Digital Converter</i>
AoD	<i>Architecture-on-demand</i>
ASE	<i>Amplified Spontaneous Emission</i>
ASIC	<i>Application-specific Integrated Circuit</i>
ASK	<i>Amplitude Shift Keying</i>
AWGN	<i>Additive White Gaussian Noise</i>
BER	<i>Bit Error Rate</i>
BPSK	<i>Binary Phase Shift Keying</i>
CapEx	<i>Capital Expenditure</i>
CD	<i>Chromatic Dispersion</i>
CMA	<i>Constant Modulus Algorithm</i>
CMOS	<i>Complementary Metal Oxide Semiconductor</i>
CNLSE	<i>Coupled Nonlinear Schrödinger Equation</i>
C/D/C	<i>Colorless / Directionless / Contentionless</i>
DAC	<i>Digital-to-Analog Converter</i>
DBP	<i>Digital Backpropagation</i>
DC	<i>Direct Current</i>
DD	<i>Decision-directed</i>
DD-LMS	<i>Decision-directed Least Mean Squares</i>
DE	<i>Dynamic Equalizer</i>
DFT	<i>Discrete Fourier Transform</i>
DGD	<i>Differential Group Delay</i>
DK	<i>Development Kit</i>
DSP	<i>Digital Signal Processing</i>
EDFA	<i>Erbium Doped Fiber Amplifier</i>
EVM	<i>Error Vector Magnitude</i>
FD	<i>Frequency-domain</i>
FEC	<i>Forward Error Correction</i>
FFT	<i>Fast Fourier Transform</i>
FIR	<i>Finite Impulse Response</i>
FPGA	<i>Field Programmable Gate Array</i>

FWM	<i>Four-wave Mixing</i>
GbE	<i>Gigabit Ethernet</i>
GSOP	<i>Gram-Schmidt Orthogonalization Procedure</i>
GTED	<i>Gardner Timing Error Detector</i>
GVD	<i>Group Velocity Dispersion</i>
I	<i>In-phase</i>
IFFT	<i>Inverse Fast Fourier Transform</i>
iFWM	<i>Intra-channel Four-wave Mixing</i>
IP	<i>Internet Protocol</i>
ISI	<i>Intersymbol Interference</i>
ITU	<i>International Telecommunication Union</i>
ITU-T	<i>International Telecommunication Union Standardization Sector</i>
iXPM	<i>Intra-channel Cross-phase Modulation</i>
LCoS	<i>Liquid Crystal on Silicon</i>
LiNbO <sub>3</sub>	<i>Lithium Niobate</i>
LINX	<i>London Internet Exchange Point</i>
LMS	<i>Least Mean Squares</i>
LO	<i>Local Oscillator</i>
LP	<i>Low-pass</i>
LPF	<i>Low-pass Filter</i>
LUT	<i>Lookup Table</i>
MGTED	<i>Modified Gardner Timing Error Detector</i>
MEMS	<i>Micro-electro-mechanical System</i>
MIMO	<i>Multiple-Inputs Multiple-Outputs</i>
MMF	<i>Multi-mode Fiber</i>
MMSE	<i>Minimum Mean Square Error</i>
mQAM	<i>Quadrature Amplitude Modulation of Order “m”</i>
MSE	<i>Mean Square Error</i>
MZM	<i>Mach-Zehnder Modulator</i>
NCO	<i>Numerically-controlled Oscillator</i>
NLI	<i>Nonlinear Interference</i>
NLSE	<i>Nonlinear Schrödinger Equation</i>
NRZ	<i>Non-return-to-zero</i>
ODU	<i>Optical Data Unit</i>
O-E-O	<i>Opto-electro-optical</i>
OFDM	<i>Orthogonal Frequency-division Multiplexing</i>

OIF	<i>Optical Internetworking Forum</i>
OpEx	<i>Operational Expenditure</i>
OPU	<i>Optical Payload Unit</i>
OSA	<i>Optical Spectrum Analyzer</i>
OSNR	<i>Optical Signal-to-noise Ratio</i>
OTN	<i>Optical Transport Network</i>
OTU	<i>Optical Transport Unit</i>
PAM	<i>Pulse Amplitude Modulation</i>
PBC	<i>Polarization Beam Combiner</i>
PBS	<i>Polarization Beam Splitter</i>
PI	<i>Proportional-integral</i>
PM	<i>Polarization Division Multiplexing</i>
PM-IQ	<i>Polarization Multiplexed In-phase and Quadrature</i>
PMD	<i>Polarization Mode Dispersion</i>
Pol-Mux	<i>Polarization Multiplexing</i>
PPG	<i>Pulse Pattern Generator</i>
PRBS	<i>Pseudorandom Binary Sequence</i>
PS	<i>Power Spectral Density</i>
PSD	<i>Power Splitter</i>
PSP	<i>Principal States of Polarization</i>
PSK	<i>Phase-Shift Keying</i>
PU	<i>Phase Unwrapper</i>
Q	<i>Quadrature</i>
QAM	<i>Quadrature Amplitude Modulation</i>
QPSK	<i>Quadrature Phase Shift Keying</i>
RC	<i>Raised Cosine</i>
RDE	<i>Radius-directed Equalizer</i>
ROADM	<i>Reconfigurable Optical Add-drop Multiplexer</i>
RSA	<i>Routing &amp; Spectrum Allocation</i>
Rx	<i>Receiver</i>
RZ	<i>Return-to-zero</i>
SBS	<i>Stimulated Brillouin Scattering</i>
SE	<i>Spectral Efficiency</i>
SMF	<i>Single-mode Fiber</i>
SNR	<i>Signal-to-noise Ratio</i>
SOPMD	<i>Second-order Polarization Mode Dispersion</i>
SPM	<i>Self-phase Modulation</i>

SRS	<i>Stimulated Raman Scattering</i>
SSFM	<i>Split-step Fourier Method</i>
TD	<i>Time-domain</i>
TED	<i>Timing Error Detector</i>
TIA	<i>Transimpedance Amplifier</i>
Tx	<i>Transmitter</i>
VPS	<i>Variable Power Splitter</i>
WDM	<i>Wavelength Division Multiplexing</i>
WSS	<i>Wavelength-selective Switch</i>
XPM	<i>Cross-phase Modulation</i>

## LIST OF PUBLICATIONS ASSOCIATED WITH THE THESIS

- V. N. Rozental, S. M. Rossi, A. Chiuchiarelli, T. C. Lima, J. D. Reis, J. R. F. de Oliveira and D. A. A. Mello: “Gradual symbol rate switching for synchronous operation of flexible optical transceivers”. *IEEE Photonics Technology Letters*, vol. 28, issue 4, February 2016.
- V.N. Rozental, V. Parahyba, J. D. Reis, J. R. F. Oliveira and D. A. A. Mello, “Digital-domain chromatic dispersion compensation for different pulse shapes: practical considerations.” In *SBMO/IEEE MTT-S International Microwave and Optoelectronics Conference (IMOC)*, 3-6 November 2015.
- V. N. Rozental and D. A. A. Mello: “Hitless rate switching for dynamically-reconfigurable optical systems”. *IEEE Photonics Journal*, vol. 7, n. 2, April 2015.
- V. N. Rozental, G. Bruno, M. Camera and D. A. A. Mello: “Novel equalizer architecture for hitless rate switching in energy-efficient optical systems”. In: *Optical Fiber Communications Conference (OFC)*, paper Th4D.6, 2014.
- D. A. A. Mello, V. N. Rozental, T. C. Lima, F. C. Pereira, A. N. Barreto, M. Camera and G. Bruno: “Adaptive optical transceivers: concepts and challenges”. *Journal of Communications and Information Systems*, vol. 29, no. 1, May 2014.
- V. N. Rozental, G. Bruno, G. Lombardi, R. Grosso, A. Alping and D. A. A. Mello: “Cognitive power management in 100G optical transponders”. In: *International Conference on Transparent Optical Networks (ICTON)*, paper We.D1.3, 2012.

## **PATENT APPLICATIONS ASSOCIATED WITH THE THESIS**

- “Circuito e Método de Mudança Síncrona de Taxa e Banda do Sinal em Transceptores Ópticos Coerentes (Circuit and Method for Synchronous Signal Rate and Bandwidth Variation in Coherent Optical Transceivers)” Inventor: V. N. Rozental, BR10 2015 014189-0 Filed by CPqD to INPI, Brazil, on 16/06/2015.
- “An Optical Receiver,” Inventor: V. N. Rozental PCT/EP2013/071420. Filed by Ericsson on 14/10/2013.

# Chapter 1 INTRODUCTION

This chapter establishes the contextual background for the rest of the work. We begin by briefly discussing the optical communication systems evolution from the first generation intensity-modulated multi-mode fiber links, until the currently commercialized 100 Gb/s coherent systems. Next, we address the strategies for increasing the efficiency of optical networks through adaptivity and flexibility, and discuss the emerging enabling technologies. We begin with the network level considerations, and arrive to the flexible transceiver description, presenting the literature review on the latest work. We present the motivation that drove this work, and conclude the chapter by stating our contributions and the structure of this thesis.

## 1.1 EVOLUTION OF OPTICAL COMMUNICATIONS

The telecommunications boom of the last decades has been effectively shaping the contemporary society, changing behavioral patterns, driving public opinion and global economy. Reliable communications enable the development of new, more and more bandwidth-intensive applications, such as video-on-demand and online gaming, which in turn drive the need for ever growing transmission requirements. This revolution was namely possible due to developments in optical fiber communications. Perhaps, the most important role of fiber communications lays within the long-haul and ultra-long-haul transmission that constitutes the Internet backbone, spreading across continents via terrestrial and submarine optical cables.

The success of optical fibers as a signal propagation medium is due to their high transmission capacity, given by the bandwidth  $\times$  distance product [1]. Modern long-haul optical systems use a transmission window of about 12.5 THz. High propagation distances are ensured by the extremely low attenuation,  $\alpha$ , with a flat profile over the transmission window. For standard (single-mode) fibers, the International Telecommunications Union (ITU) requires that attenuation be below 0.3 dB/km at 1550 nm [2], while some commercially available fibers reach remarkable values below 0.18 dB/km [3].

Fiber communication systems can be classified according to the employed tech-

nology. In the following, we adopt the classification methodology of [1]. The first generation multimode fiber systems, where signal power is split into different propagation modes causing signal degradation, operated at wavelengths around 800 nm. Those systems had a typical rate of 45 Mb/s, requiring an opto-electro-optical (O-E-O) signal regeneration after every 10 km of transmission [1]. Creation of the single-mode fibers, along with the semiconductor InGaAsP lasers, transmitting at around 1300 nm, originated the second generation of optical systems, eliminating modal dispersion, and operating at a fiber attenuation region of 0.5 dB/km. In the late 80's, those systems achieved transmission rates of 1.7 Gb/s, with O-E-O regeneration after every 50 km [1]. Third generation optical systems migrated to the transmission window around 1500 nm, characterized by the lowest attenuation values, and used narrow spectral width laser sources, reducing dispersion. Fourth generation of optical systems began with the invention of erbium-doped fiber amplifiers (EDFAs), which allowed two major improvements: firstly, EDFA technology increased the transparent reach (that is, the signal propagation distance without the O-E-O regeneration) in orders of magnitude, drastically reducing the system costs; and secondly, EDFA's wide amplification band allowed wavelength division multiplexing (WDM) of numerous optical channels on a single fiber. Coherent detection systems can be classified as the fifth generation of optical systems. Their emergence was driven by the advances in microelectronics, especially, by the development of ultra-high-speed and wide bandwidth analog-to-digital converters (ADCs). Coherent detection linearly maps the field of the optical signal to the electronic domain, as opposed to the square-law detection of the earlier systems, based solely on the signal intensity information. Linear mapping preserves the signal phase information, allowing to employ high-order modulation formats, and increase the spectral efficiency (SE). At the same time, it allows the use of conventional digital signal processing (DSP) techniques to mitigate optical channel impairments.

The evolution of optical communications is depicted in Figure 1.1, adapted from [4], and [5]. The capacity  $\times$  distance product has shown approximately a fourfold increase every decade until the year of 2000 (dashed blue), originating the so-called "Optical Moore's Law". In addition to the generation-marking disruptive technologies, several incremental technologies were introduced. Those include chromatic dispersion management, development of dispersion-shifted fibers, Raman amplification, and others. As can be appreciated from Figure 1.1, single mode fibers cannot ensure the same network capacity growth to follow the Moore's Optical Law, indicating a need for technological breakthroughs. Some authors appoint to the space-division multiplexing to be the next generation disruptive technology [5, 6].

To complete the overview of optical system evolution, we conclude with a discussion



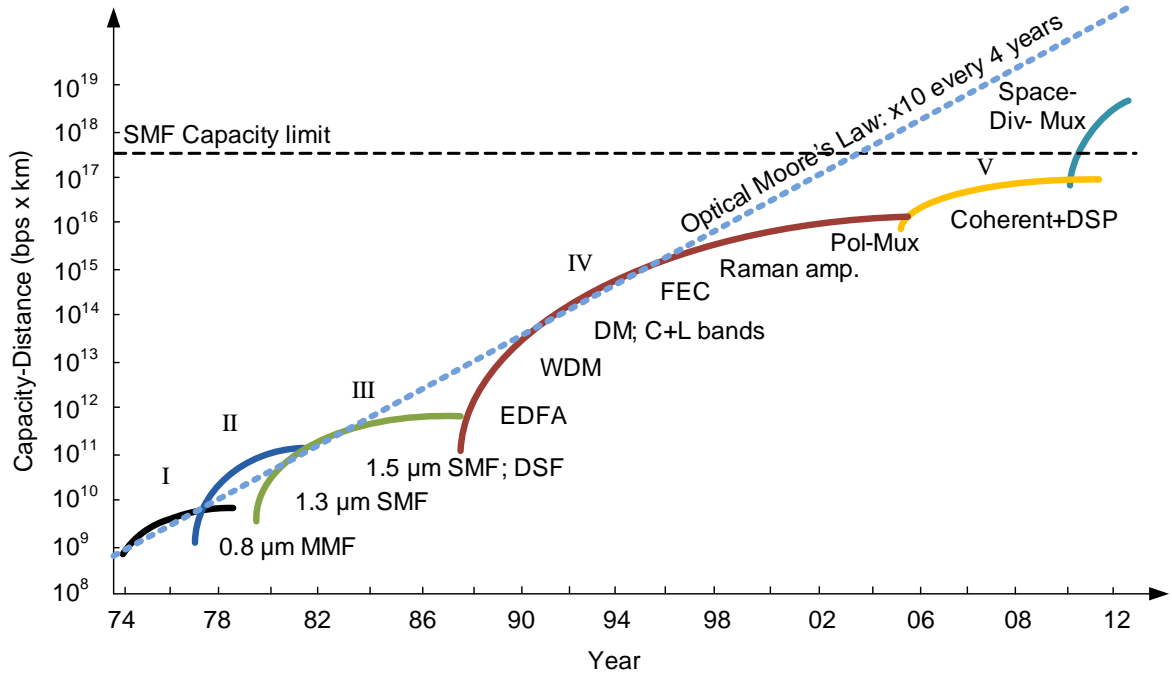


Figure 1.1: Capacity  $\times$  distance evolution of optical systems: Roman numerals indicate system generation; MMF – multi-mode fiber; SMF – single-mode fiber; EDFA – erbium-doped fiber amplifier; WDM – wavelength division multiplexing; DM – chromatic dispersion management; FEC – forward error correction; Raman amp. – Raman amplification; Pol-mux – polarization multiplexing; DSP – digital signal processing; Space-Div-Mux – space division multiplexing.

on their capacity limits. A “down-to-earth” approach for finding the capacity limits was proposed in [7]. The authors assumed an optically-routed network configuration, where the receiver does not possess the information about the out-of-band optical field, corresponding to the co-propagating channels that interact with the channel of interest. This interaction, hence, imposes limitations on the achievable spectral efficiency, known as the nonlinear capacity limit [8]. With the otherwise quite broad assumptions (ideal in-band nonlinear compensation, low noise-figure amplifiers, etc.), authors produced by simulation a set of SE curves for different link lengths. A combination of the results in [7] with a 12.5-THz transmission window yields a maximum capacity for a single-mode fiber of  $\approx 5.5 \times 10^{17}$  bps x km.

## 1.2 TOWARDS FLEXIBLE OPTICAL NETWORKS

Along with the struggle for capacity, network efficiency is an important concern for the next generation optical systems. Here, the goal is to optimize the quality of service while reducing deployment, component and operational costs, referred to as the capital and operational expenditures (CapEx and OpEx). Additional concern is the constantly growing energy consumption associated with the information technology and communication systems [9].

In this context, a major paradigm shift was the adoption of the fine-granularity spectral grid (flex-grid), where signal bandwidth is assembled by adding up several 12.5-GHz slices [10], as opposed to the standard fixed 50-GHz WDM grid. Adopted mainly to support the 400 Gb/s and beyond subcarrier-multiplexed optical channels, flex-grid is driving the development of flexible network components, allowing setting up channels of different bandwidths, and vice versa, properly size the bandwidth for a specific channel [11]. Optical parallelism provided by subcarrier multiplexing allows to overcome electronics bandwidth and speed limitations, emerging for  $\geq 400\text{G}$  data rates. A set of subcarriers that passes through the optical network as a single entity is commonly referred to as superchannels [12]. Flex-grid supports superchannels with different number of subcarriers, allowing trade-offs between transmission rate and spectral occupation.

In the network plane, mesh-topology networks adopt the mixed-line-rate transmission [13], where different rate and spectral content channels co-propagate on the same fiber. Traditional opaque and transparent network architectures are being replaced by the more flexible translucent architecture. In the early opaque networks, all signals underwent O-E-O regeneration at every network node. Transparent networks, on the contrary, allow signals to cross intermediate nodes via express optical paths. The drawback of transparent networks is that when a signal requires regeneration at an intermediate node due to its poor quality, it must be locally dropped and processed at the IP level, before being added back to the network. In the translucent architecture, the incoming signal either transparently bypasses the intermediate nodes via optical switching, or, in case of a poor signal quality, it is locally regenerated at dedicated regenerators, sparing the IP level processing. However, the IP-level processing of transparent networks has the advantage of enabling traffic grooming – a method for efficient mapping of low-speed traffic requests onto a high-capacity lightpath [14].

For complex networks, dynamic channel routing & spectrum allocation (RSA) methods play a crucial role in system performance, and, hence, are being extensively studied

(e.g., [15], [16]). The cost function for RSA optimization may be based on several parameters, where usually the goal is to reduce the service request blocking probability, while minimizing the overall network cost and/or power consumption. To reduce spectrum blocking, where service request is rejected because there are no sufficiently wide spectral windows available, defragmentation techniques are being developed. Defragmentation refers to joining available spectral fragments by frequency shifting the existing signals. Some of the defragmentation methods proposed in the literature are the make-before-brake method, where new lightpaths are established on alternative routes before releasing the original paths [17], and the push-pull method, based on dynamic lightpath frequency retuning [18]. Another technique for coping with the network dynamicity is the spectrum expansion/contraction, where neighboring channels share spectral slots, occupying and releasing them according to the requirements. Spectrum expansion/contraction and defragmentation may be further combined through the dynamic cooperative spectrum sharing policies [19].

The core device of an optical network node is a reconfigurable optical add-drop multiplexer (ROADM) that locally aggregates and extracts selected optical channels to/from the network. Additionally, an ROADM establishes the lightpaths for different wavelength channels by optical switching. To provide a full optical layer reconfigurability, the new-generation ROADMs must be flex-grid-compatible, and support the colorless, directionless, and contentionless (C/D/C) properties: colorless property means that any wavelength signal can be assigned to any ROADM add/drop port [20]; directionless property allows routing a signal generated in any transceiver to any ROADM egress port; and contentionless property means avoiding contention of resources. For example, to avoid contention by wavelength, multiple signals that share the same wavelength cannot interfere with each other inside the ROADM. From the design perspective it means that multiple signals with overlapping spectra are not multiplexed onto a single fiber. An attractive alternative for the hard-wired static ROADM architecture, whose physical implementation becomes extremely cumbersome for high-degree C-D-C functionality support, is the architecture-on-demand (AoD) [21]. In AoD, there exist component modules for optical (de)multiplexers, spectrum selective switches, couplers and splitters, interconnected by an optical backplane, based on movable micro-electro-mechanical systems (MEMS) mirrors, or liquid crystal on silicon (LCoS) technologies. Thus, a tailored for the required functionality architecture can be dynamically synthesized [22].

## 1.3 ADAPTIVE OPTICAL TRANSCEIVERS

### 1.3.1 General description

In the physical layer of future networks, the key component is an adaptive optical transceiver<sup>1</sup>, schematically represented in Figure 1.2 (adapted from [23, 24]). To reduce CapEx, the transceiver must support variable transmission rates, and be agnostic towards the optical route. The transceiver must extract relevant channel information,

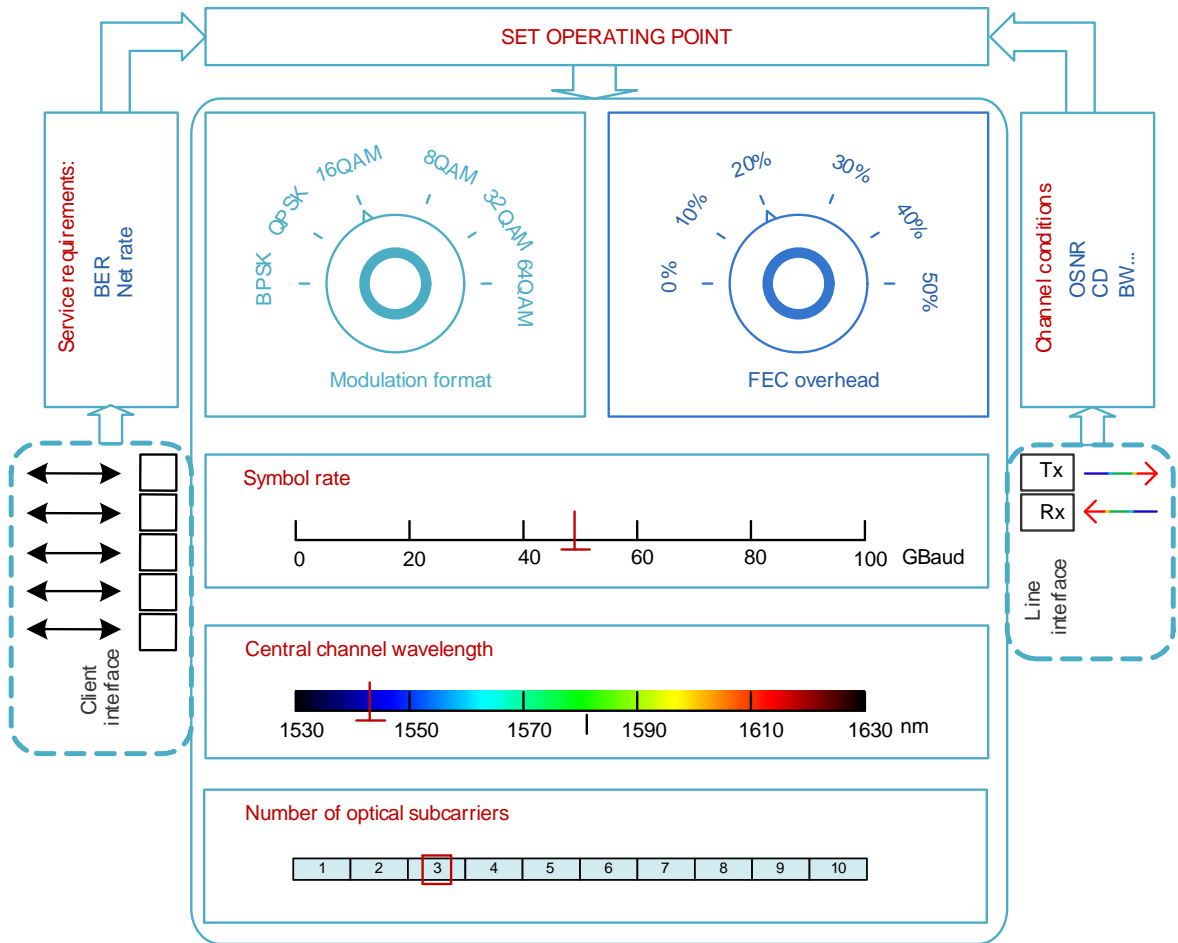


Figure 1.2: Adaptive optical transceiver.

such as the signal-to-noise ratio (SNR) and the accumulated chromatic dispersion (CD), from the incoming line interface signal (right-hand side panel of Figure 1.2), while receiving the performance requirements, such as the required bit error rate (BER) and

<sup>1</sup>Also referred to as transponder, because of the optical-to-optical conversion functionality, when client optical signals are converted to different rate/wavelength line optical signals. In this work we use both terms interchangeably.

the net bitrate specifications from the control plane (left-hand side panel of Figure 1.2). Based on this information, the adaptive transceiver sets the operating point, which, while fulfilling the system requirements, optimizes some cost function, e.g., reduces power consumption. By operating point, we refer to the set of parameters that define the transceiver performance, in particular, number of optical carriers, symbol rate, modulation format, chain of signal processing algorithms, and forward error correction (FEC) code rate [24,25]. The optimization may be local, where the power consumption of the proper transceiver is minimized, or alternatively, it may be a part of an intelligent management system that minimizes the whole network power consumption [25]. Additionally, to support the flexible network-level operation, the transceiver must constantly monitor its client interface transmission requirements, negotiating spectrum release/request with the control plane in accordance with the traffic fluctuations, and dynamically optimize its operating point.

### 1.3.2 Conventional versus DSP-capable transmitter architecture for rate-flexible transmission

Multilevel constellations in optical transmitters may be constructed using either binary or DSP-produced driving signals. The basic architecture for both cases is depicted in Figure 1.3.

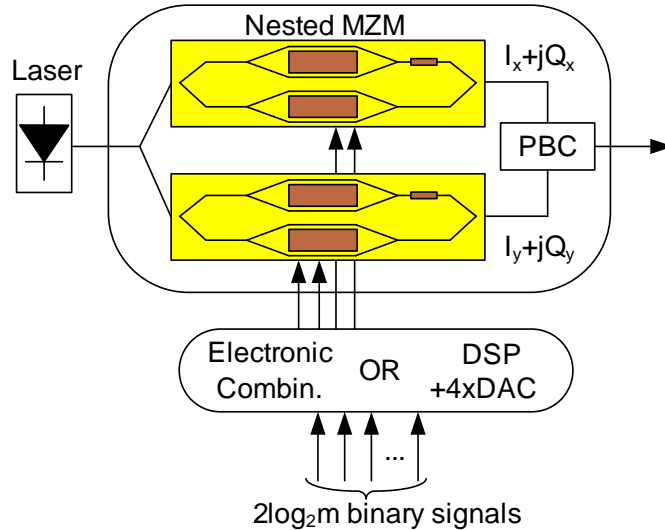


Figure 1.3: Multilevel optical signal generation. MZM: Mach-Zehnder modulator; PBC: polarization beam combiner.

The core building block of this architecture is the nested Mach-Zehnder modulator

(MZM), indicated in yellow in Figure 1.3. Nested MZM maps electrical field of the driving signals onto optical domain, generating a quadrature-amplitude-modulated (QAM) output. Two such structures, whose outputs are polarization-multiplexed (PM) by the polarization beam combiner (PBC), constitute a polarization-multiplexed in-phase & quadrature (PM-IQ) modulator structure.

To generate PM-mQAM signals, where  $m$  is the cardinality of the digital alphabet, the binary-signal-driven architecture combines  $2\log_2 m$  binary streams in the electronic domain (using corresponding attenuation patterns), to produce four  $\log_2 m/2$ -pulse-amplitude-modulated (PAM) signals that drive the I and Q modulator arms for each polarization. Alternatively, multilevel constellations from binary signals may be generated by more complex optical structures that require  $\log_2 m/2$  PM-IQ modulators, and two  $1:\log_2 m/2$  variable power splitters (VPSs) [26]. Different modulation formats are generated by activating the corresponding number of PM-IQ modulators, and adjusting the attenuation pattern of the VPSs. In the rest of the thesis we will refer to the binary-signal-driven optical transmitters as the conventional ones<sup>1</sup>.

Conversely, a DSP-driven transmitter relies on DSP capabilities, where pulse format and constellation are shaped in digital domain, following by a digital-to-analog converter (DAC) that generates modulator driving signals.

Both architectures present certain advantages in comparison to one another. The conventional architecture is simpler, because it avoids transmit-side DSP capabilities, and costly ultra-high-speed, wide-bandwidth, and high resolution ADCs. On the other hand, DSP allows to generate Nyquist-shaped and orthogonal-frequency-division-multiplexed (OFDM) signals, improving spectral efficiency (SE). This feature is extremely important in the context of 400G and 1T channels employing optical parallelism (that is more than one optical carrier per connection). Additionally, DSP allows to electronically generate (sub)carriers, provided there are sufficient processing and bandwidth capacity.

Both schemes have been used in the literature as candidates for rate adaptive transmission. Thus, for conventional architecture, Rival and Morea proposed two schemes for modifying a 100G PM-QPSK transmitter for transmitting rates of 28, 56 and 112 Gb/s. The first scheme, described in [27], suggested to constrain the modulating signals via software so as to obtain PM binary phase shift keying (BPSK) and a single-polarization (SP)-BPSK modulation formats, and lower transmission rates. The second scheme [28], introduced mechanical switches that disable parts of the transmitter, yielding identical changes in rates and modulation format. An alternative scheme

---

<sup>1</sup>Though, we must bear in mind that DSP-capable transmitters are likely to become the new standard within a few years.

was proposed and fabricated in a hybrid integration of silica planar lightwave circuits and LiNbO<sub>3</sub> phase modulators in [29]. This scheme was based on two modulation stages, includes four MZMs per polarization, and supported the following modulation formats: QPSK, 8PSK, 8QAM and 16QAM. Two tunable couplers and a phase shifter were used to set the desired modulation format. Another two-stage conventional modulation scheme was proposed in [30], generating BPSK, QPSK, 8QAM and 16QAM. The scheme included a dual-drive MZM in the first stage, and a dual-parallel MZM in the second stage. Different modulation formats are created by adjusting the driving and bias voltages of the MZMs in both stages.

Likewise, many transmission experiments use digital waveform generation. Freude *et al.* demonstrated an 8-modulation formats transmitter, set by software-controlled field-programmable gate array (FPGA), allowing format switching within 5 ns [31]. Modulation formats were switched within a single clock cycle (5 ns at 28 GBd), by rewriting the FPGA look-up tables content. A conceptual software-defined multi-rate transceiver was presented in [32], being, essentially, a concatenation of several multilevel-signal-driven PM-IQ modulators. Authors left open choices for number, modulation formats and spacing of the subcarriers, referring to spectral efficiency vs. reach trade-offs. It should be mentioned, that in spite of the aforementioned benefits of the DSP-driving signal transmitter architecture, it usually requires high computational power and complex hardware, as well as superior quality driver amplifiers [30].

## 1.4 MOTIVATION BEHIND THIS WORK

Figures 1.4(a,b) show the daily and the weekly aggregate Internet traffic at the traffic exchange points between the autonomous systems networks in the metropolitan regions of Brazil [33]. The traffic rates fluctuate between  $\sim 260$  Gb/s during nighttime, and  $\sim 1.4$  Tb/s at the peak values. European traffic exchange points depict similar patterns. As an example, Figure 1.5 shows daily Internet aggregate traffic fluctuations at the London Internet Exchange point (LINX) [34], ranging from  $\sim 0.9$  to  $\sim 3$  Tb/s. Observe that the traffic is lower than 1 Tb/s for approximately 3.5 hours, and lower than 2 Tb/s for approximately 10 hours.

Additional sources of the network traffic fluctuation include addition/removal of clients, maintenance operations, optical restoration in case of failures, *ad hoc* service requirements (as in data center backup operations), large scale social events, and more.

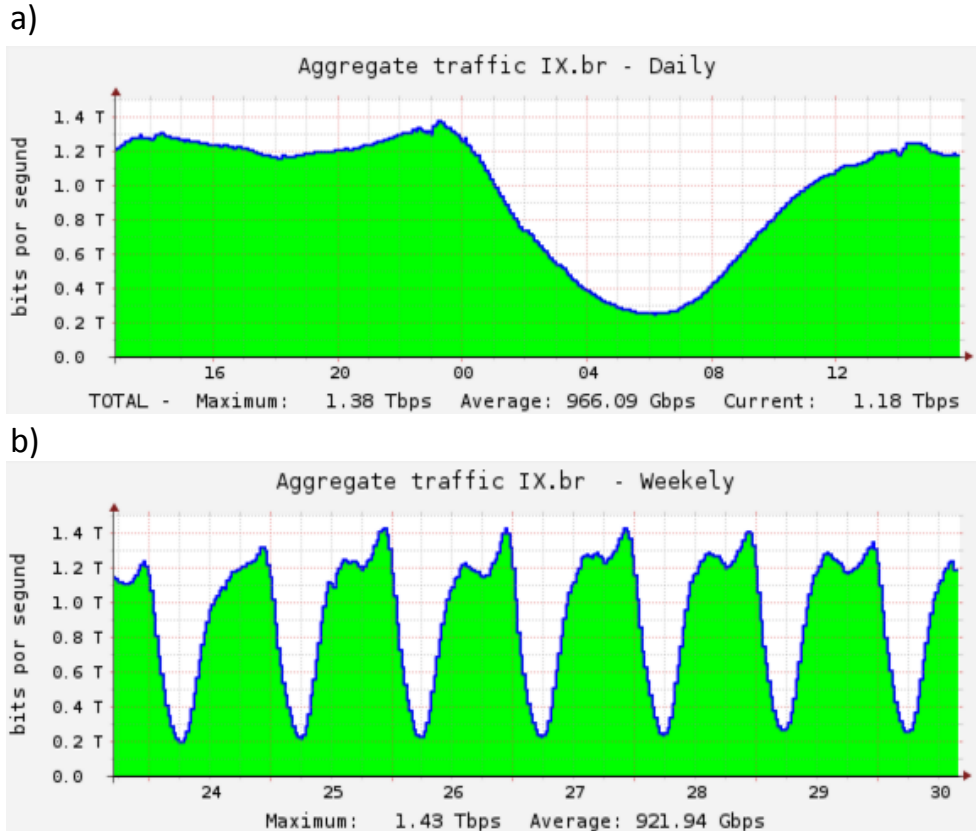


Figure 1.4: a) Daily and (b) weekly statistics of the aggregate Internet traffic between autonomous systems in Brazil [33].

Naturally, dimensioning the network to accommodate the highest traffic load – as done in conventional networks nowadays – results in spectral resource waste and unnecessary power consumption. This situation leads to premature network saturation and high operational costs. In order to increase the efficiency, future networks must be able to adjust to the changing transmission and network conditions.

While transponder architectures discussed in Section 1.3.2 mostly regard modulation format switching, which is an important feature for variable length optical links support, it is the symbol rate adjustment that enables energy and bandwidth savings when traffic load is considerably lower than the system nominal transmission rate. Energy savings can be achieved by reducing the size of the CD compensation bulk equalizer, whose length is inversely proportional to the square of the symbol rate [35]. Occupied bandwidth, in turn, is directly proportional to the symbol rate, and so its excess can be released to the network control plane, as discussed in Section 6.4.

Although dynamic rate and bandwidth adjustment functionalities are envisioned by the flexible networking paradigms, to the best of our knowledge, no technological solution for hitless symbol rate switching during transmission has previously been of-



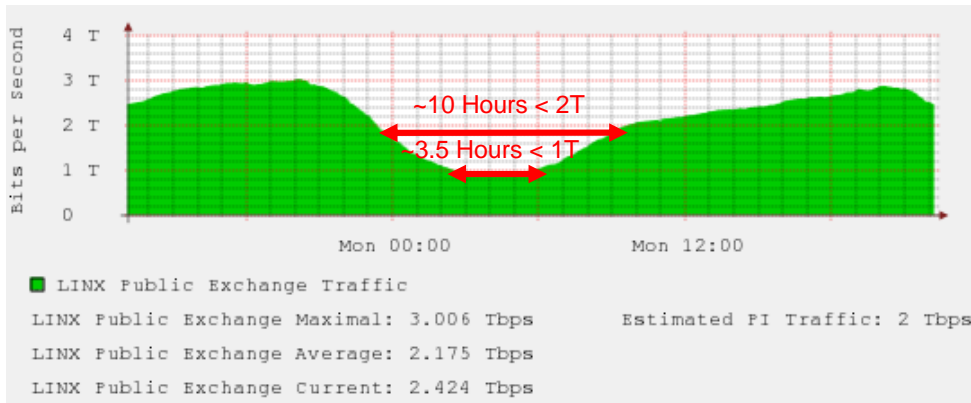


Figure 1.5: Aggregate traffic at the London Internet Exchange point (LINX) [34].

ferred in the literature.<sup>1</sup> Some works mention clock tuning of the electronic blocks [36], but this kind of synchronization would be extremely difficult to achieve online. Therefore, network operators have concerns about switching the symbol rate, because the transponder would have to be completely reinitialized. Evidently, there is a need for technological solutions for hitless symbol rate and bandwidth adjustment, to support flexible and power efficient networking.

While online rate switching is not yet supported by the client side 10/40/100 Gigabit Ethernet and line the side OTN protocols, many recent publications, e.g., [11, 37], anticipate transport layer support for dynamic rate adjustment capabilities. In this context, such developments as the recent kick-off of the OIF’s Flex Ethernet project [38], as well as the ODUflex ITU-T recommendation [39], are encouraging indicators.

Finally, to stress the relevance of our work, we would like to quote “Optical Network Design and Planning,” by Jane M. Simmons [40]:

“...the flexibility of a bandwidth-programmable transponder allows it to adjust to diurnal changes of that connection to optimize the use of the network capacity. Programmable transponders also offer the possibility of saving energy...” “... if the required data rate of a connection is reduced (e.g., due to time of day), the transponder can be programmed to support a lower rate with lower power consumption.”

<sup>1</sup>By hitless switching we refer to changing transponder operation point online without the need for system resynchronization, so that it is imperceptible from the client side.

## 1.5 OVERVIEW OF THE RELATED WORK

Much of the related work was cited throughout the previous sections, within the relevant context. In this section we focus exclusively on works that involve online transmission rate and/or bandwidth variation.

Several paradigm changing papers address the necessity of developing rate-adaptive mechanisms in future systems, and the importance of making the corresponding upgrades to the transport and networking protocols. In addition to the earlier quoted Jane M. Simmons [40], we can cite a notorious paper by M. Jinno, et al., “Spectrum-efficient and scalable elastic optical path network: architecture, benefits, and enabling technologies” [41]. Another work by M. Jinno, et al., “Elastic and adaptive optical networks: possible adoption scenarios and future standardization aspects” [37], discusses practical ways of extending the ITU-T G.709 recommendation [42] to include flex-rate optical channels. O. Gerstel et al., in “Elastic optical networking: a new dawn for the optical layer?” discusses bandwidth-sliceable transceivers, and required extensions to the OTN and Ethernet standards. In the context of this thesis, these papers refute a possible line of critique, that suggests that our proposed methods cannot be accommodated by current-state client- and line-side protocols.

An important line of research within rate variation is the code-rate-adaptive transmission, where the FEC overhead is adjusted according to the channel conditions. Here, we can cite the following papers: M. Arabaci, et al., “Nonbinary LDPC-coded modulation for rate-adaptive optical fiber communication without bandwidth expansion,” that simulates transmission rates between 100 Gb/s and 300 Gb/s in steps of 26.67 Gb/s, while running at a fixed symbol rate and occupying a fixed bandwidth [43]; G. Gwang-Hyun, L. Klak and J. M. Kahn, “Rate-adaptive coding for optical fiber transmission systems,” that simulates several intermediate transmission rates varying from 10 to 100 Gb/s [44]; and D. Mello et al., “Optical networking with variable-code-rate transceivers,” that simulates several intermediate transmission rates varying from  $\sim 100$  to  $\sim 500$  Gb/s for several values of transparent reach [45].

Online rate switching was recently demonstrated via computer simulations by Z. Zhang, C. Li, in “Hitless Multi-rate Coherent Transceiver,” where the authors used additional digital signal processing modules, adjusting the transmission rate by changing modulation order [46].

Both code-rate and modulation format adaptation result in important signal quality (reach), rate, and complexity trade-offs. However, those schemes are designed to operate at constant symbol rate, and so, cannot be used to release excess bandwidth

to the network plane. Conversely, a concept of bandwidth-scalable (alternatively, bandwidth-variable) transceiver targets bandwidth adjustment. Bandwidth-variable transceiver can selectively activate/deactivate optical or electrical subcarriers within superchannels. Several works explore this line of research; for example: “Bandwidth-scalable long-haul transmission using synchronized colorless transceivers and efficient wavelength-selective switches,” by D. Barros, et al. [47]; “Variable-bandwidth superchannels using synchronized colorless transceivers”, by M. Sharif and J. M. Kahn [48]; “Demonstration of real-time Ethernet to reconfigurable superchannel data transport over elastic optical network,” by S. Yan, et al. [49]. Naturally, this solution is very different from the methods based on symbol rate switching, as proposed in this thesis. For instance, it requires a plurality of subcarriers, and cannot adjust rate/bandwidth in a single-carrier transmission. Also, it is not clear how transients, produced when subcarriers are switched on and off, would affect the performance in WDM scenario. Symbol rate switching methods of this thesis do not provoke instant signal power jumps, so that transients are avoided. On the other hand, switching off part of subcarriers may, in principle, yield higher power savings, depending on the degree of optical parallelism, propagation distance and other factors. It should be noted, nevertheless, that the two approaches are not mutually exclusive, and can successfully complement each other. In this case one would operate at the channel level, and the other, at the subcarrier level.

## 1.6 OUR CONTRIBUTIONS AND OUTLINE

In this work we offer two main contributions in the context of the earlier discussed online symbol rate and bandwidth adjustment; specifically:

- Symbol rate switching method, with bandwidth adjustment for coherent optical systems with conventional transmitters, based on symbol repetitions.
- Gradual symbol rate and bandwidth adjustment method for coherent optical systems with DSP-capable transmitters.

The first contribution concerns conventional systems without transmit-side DSP functionalities. We propose a novel receive-side equalizer architecture for symbol rate switching to enhance optical systems energy efficiency under low client traffic. We also introduce a switching method that keeps track of frame and bit synchronization,

ensuring hitless operation. This contribution namely targets the currently deployed fixed-grid long and ultra-long-haul optical systems. Alternatively, it can be employed in flex-grid networks, where bandwidth adjustment to the symbol rate can be performed in optical domain by flex-grid-enabled wavelength-selective switches.

The second contribution addresses the transmit-side DSP-enabled systems, with digitally shaped optical signals. We propose a novel hitless rate switching method, which, in addition to power savings, also adjusts signal bandwidth, maintaining constant spectral efficiency. The method only requires minor adjustments to the common transponder DSP blocks architectures. Here, the key idea is to perform the adjustments in small discrete steps, allowing the dynamic equalizer at the receiver to track signal changes. This contribution is mostly beneficial in the flex-grid scenario. Both architectures are validated by computer simulation and experimentally.

We also offer the following secondary contributions:

- In the scope of frequency-domain CD equalization, we conduct computer simulations to infer practical values for the overlap length for different optical pulse shapes, considering the interplay of the pulse shape and the intrinsic system optical and electrical filtering. The obtained results may be used as guidelines for design, and trading off OSNR margin and computational complexity. We use the analysis to estimate complexity and power consumption gain of the symbol-repetition-based rate switching;
- In the scope of the gradual rate and bandwidth adjustment in systems with DSP-capable transmitters, we address the implementation feasibility from the hardware standpoint.

This thesis is structured as follows. Chapter 2 describes the main phenomena of optical transmission, addressing the impairments resulting from fiber propagation. Chapter 3 reviews the coherent detection principles and the chain of the receive-side DSP algorithms. Chapter 4 presents CD equalizer design approaches and computational complexity analysis, assessing the potential gain of the symbol-repetition-based rate switching. Chapter 5 presents the equalizer architecture and a method for hitless rate switching in dynamically reconfigurable optical systems with conventional signal generation (first major contribution). The chapter further presents computer simulation and experimental validation procedures and discusses the obtained results. Chapter 6 addresses the method for rate and bandwidth adjustment in dynamically reconfigurable systems with digitally-shaped signals (second major contribution), presenting the results of validation by computer simulation. Lastly, Chapter 7 summarizes the thesis.

## Chapter 2 OPTICAL TRANSMISSION

In its essence, a long-haul optical transmission system is composed of a transmitter (Tx) and a receiver (Rx), connected by several 80-100-km spans of optical fiber, interleaved with optical amplifiers. This arrangement is necessary because, unlike in other transmission media, signals in optical fibers are greatly deteriorated by nonlinear effects for high launch power values, and therefore, amplification must be distributed along the optical link. In this chapter we address the transmitter and receiver architectures for long-haul coherent optical systems, and review the linear and nonlinear fiber propagation impairments. This insight is essential for the subsequent discussion on Rx digital signal processing of Chapter 3.

### 2.1 THE TRANSMITTER

Figure 2.1 shows a generic single-carrier transmit-side processing block diagram, which may substantially vary in a particular implementation.

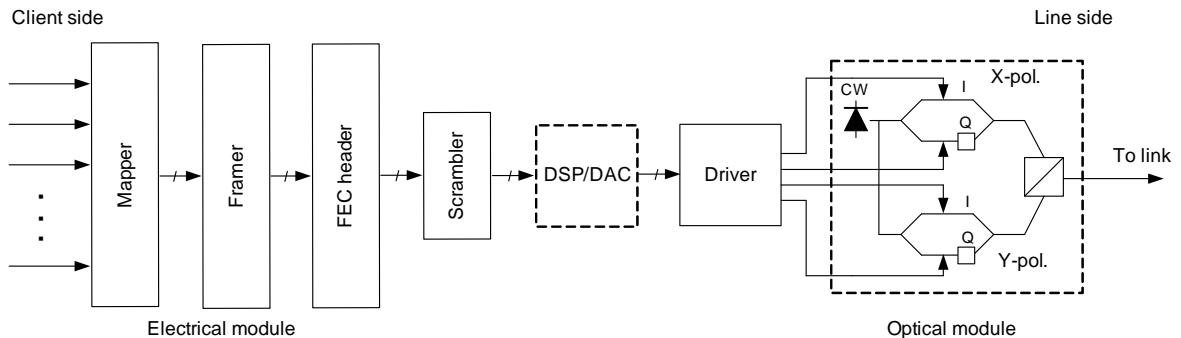


Figure 2.1: Single-carrier transmitter processing block diagram.

At the client side, the information received through the client interface(s) is mapped into several bit streams. Depending on the desired application, different client protocol types, such as 10/40/100GbE, OTU2, etc., may be supported. Client frames are clock-synchronized, multiplexed and mapped onto optical payload units (OPU) that undergo framing procedures, where protocol headers and FEC overhead are added to

form the optical transport unit frames (OTUk). The highest standardized line rate supported until now by the optical transport network (OTN) protocol is 100 Gb/s, for which,  $k = 4$  [42]. The resulting data streams are scrambled to ensure random-like transition distribution. In binary-driven transmitters, the signals are next adjusted by the driver to appropriate modulation voltages, to directly drive the in-phase (I) and quadrature (Q) components for orthogonal polarizations X-pol. and Y-pol. of the PM-IQ modulators. In Figure 2.1 we show only a single PM-IQ modulator, though, their number in binary-driven transmitters is set to support the highest modulation format, as discussed in Section 1.3.2. A multilevel-signal-driven architecture further includes a DSP block, whose function is to map binary strings onto the desired modulation format constellations, and perform pulse shaping. Nyquist-shaped signals are commonly preferred, due to their highest spectral efficiency. The DSP block is followed by a wide-bandwidth DAC, usually supporting a simple zero-order sample & hold operation [50], to generate continuous MZM driving signals.

## 2.2 OPTICAL CHANNEL

A signal launched into an optical fiber suffers from several propagation effects with both linear and nonlinear characteristics. Linear effects include signal attenuation, polarization rotation, chromatic and polarization mode dispersions, and polarization dependent loss. Main nonlinear effects are self and cross-phase modulation, four-wave mixing, Raman and Brillouin scattering. Unlike the linear effects, those are power-dependent, and produce new frequency components. Additionally, propagation over several spans leads to amplifier-generated noise accumulation, degrading signal quality. In the following, we review the main fiber propagation effects.

### 2.2.1 Fiber propagation in linear regime

#### 2.2.1.1 Polarization-independent propagation effects

Equation 2.1, known as the nonlinear Schrödinger equation (NLSE), models the propagation of optical pulses inside single-mode fibers [1]:

$$\frac{\partial A}{\partial z} = -\frac{\alpha}{2}A - \beta_1 \frac{\partial A}{\partial t} - \frac{j\beta_2}{2} \frac{\partial^2 A}{\partial t^2} + \frac{\beta_3}{6} \frac{\partial^3 A}{\partial t^3} + j\gamma|A|^2 A. \quad (2.1)$$

Here,  $A(z, t)$  is the slowly varying amplitude of the pulse envelope,  $\alpha$  is the fiber attenuation constant,  $\gamma$  is the fiber nonlinear coefficient,  $z$  and  $t$  are the distance and time variables. Also,  $\beta_{1,2,3}$  are the Taylor expansion coefficients of the propagation constant,  $\beta$ :

$$\beta(\omega) \approx \beta_0 + \beta_1(\Delta\omega) + \frac{\beta_2}{2}(\Delta\omega)^2 + \frac{\beta_3}{6}(\Delta\omega)^3 + \dots, \quad (2.2)$$

where  $\Delta\omega = \omega - \omega_0$ , being  $\omega_0$  the optical carrier angular frequency. The first term on the right-hand side of Equation (2.1) accounts for signal attenuation. In the second term,  $\beta_1$  is the inverse of the group velocity, accounting for the propagation delay. This term is commonly omitted during analysis, assuming that the reference time frame is moving at the pulse group velocity. The third term includes the so-called group-velocity dispersion (GVD) parameter,  $\beta_2$ , indicating the chromatic dispersion. The  $\beta_3$ -related term accounts for the dispersion slope, whose contribution becomes significant for WDM systems, where it causes slight changes in the GVD values of different channels. Since dispersion slope within a single channel usually has a negligible effect, we disregard this term in the following discussion. The last term of Equation (2.1) accounts for the Kerr nonlinearities, and will be treated in later sections.

#### *Fiber attenuation and optical noise*

The solution for the first term on the right-hand side of Equation (2.1) is given by the Beer's law:  $A(z) = A(0) \cdot \exp\{-\alpha z/2\}$ , or in terms of signal power [1]:

$$P(z) = P(0) \cdot \exp\{-\alpha z\}. \quad (2.3)$$

This exponential power loss is commonly compensated for by the in-line erbium-doped fiber amplifiers (EDFAs), positioned after every 80-100 km of optical fiber. Signal amplification is achieved due to the phenomenon of stimulated emission of radiation by atoms in the presence of electromagnetic field [51]. An undesired side-effect of the amplification process is the amplified spontaneous emission (ASE), that generates optical noise. Optical amplifiers are characterized by their noise figure, the ratio between the input and the output signal-to-noise ratios (SNRs), referring to electric power, generated when optical signal is converted into electric current [1]:

$$F = \frac{\text{SNR}_{in}}{\text{SNR}_{out}}. \quad (2.4)$$

The optical SNR (OSNR) at the end of the optical link with constant amplifier spacing may be computed by the power budget equation [52]:

$$\text{OSNR}_{\text{dB}} = P_{\text{TX}} - F - 10 \log_{10}(N_s) - \alpha_{\text{dB}} \cdot L_s - 10 \log_{10}(h\nu B_{\text{ref}}), \quad (2.5)$$

where  $P_{\text{TX}}$  is the transmitted signal power,  $N_s$  is the number of fiber spans,  $L_s$  is the span length,  $h$  is the Planck constant,  $\nu$  is the carrier frequency, and  $B_{\text{ref}}$  is the reference optical bandwidth, typically 12.5 GHz. Due to its quasi-constant power spectral density within the channel bandwidth, ASE is commonly modeled as additive white Gaussian noise.

### *Chromatic dispersion*

To obtain the solution of Equation (2.1) with respect to the CD-related term on the right-hand side, it is convenient to transform the equation to the frequency domain via the Fourier transform:

$$\left\{ \frac{\partial A}{\partial z} = -\frac{j\beta_2}{2} \frac{\partial^2 A}{\partial t^2} \right\} \xleftrightarrow{F} \left\{ \frac{\partial \tilde{A}}{\partial z} = \frac{j\beta_2}{2} \omega^2 \tilde{A} \right\}, \quad (2.6)$$

where  $\tilde{A}$  is the Fourier transform of  $A$ , and  $\omega$  is the angular frequency. Here, we used the time-domain differentiation property of the Fourier transform [53]. The solution of the differential equation on the right-hand side of Equation (2.6) is:

$$\tilde{A}(z, \omega) = \tilde{A}(0, \omega) \exp\left(\frac{j\beta_2 z}{2} \omega^2\right). \quad (2.7)$$

Thus, dispersive fiber behaves like an all-pass filter with non-linear phase response. This response transforms into temporal spreading of the pulses, leading to signal degradation by intersymbol interference (ISI), as shown in Figure 2.2.

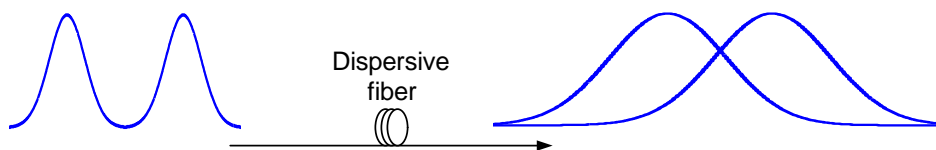


Figure 2.2: Intersymbol interference produced by CD.



Chromatic dispersion in optical fibers is commonly characterized by the dispersion parameter,  $D$ , given by:

$$D = -\frac{2\pi c}{\lambda^2}\beta_2, \quad (2.8)$$

where  $c$  is the speed of light, and  $\lambda$  is the carrier wavelength.

### 2.2.1.2 Polarization-dependent propagation effects

#### *First-order PMD*

Under perfect conditions, an arbitrarily polarized signal would maintain its state of polarization (SoP) during fiber propagation. In real fibers, however, geometry irregularities, deformations due to non-uniform mechanical stress and temperature variations provoke polarization-dependent temporal and spacial changes in fiber refractive index, known as fiber birefringence, inducing polarization mode dispersion (PMD). It is convenient to separate between linear and circular types of birefringence [54]. In short linearly birefringent elements it is possible to identify two orthogonal states of polarization with slightly different refractive indices, called principal states of polarization (PSPs), or eigenpolarizations [55]. Projections onto the PSPs of an arbitrarily polarized signal would suffer a mutual delay, called differential group delay (DGD), given by:

$$\Delta\tau = \frac{z\Delta n}{c} = \frac{z\Delta\beta}{\omega_0}, \quad (2.9)$$

where  $\Delta n$  and  $\Delta\beta$  are the differences between the PSPs' refractive indices and propagation constants,  $z$  is the length of the birefringent element,  $c$  is the speed of light, and  $\omega_0$  is the optical carrier angular frequency. Signal state of polarization would periodically evolve due to DGD, with cycles corresponding to phase differences of  $\omega_0\Delta\tau = k2\pi$  ( $k \in \mathbb{N}$ ) between the PSP components.

Circular birefringence results namely from fiber torsion, and is characterized by the difference in the refractive indices for the left-hand and right-hand circularly polarized waves [54]. The torsion rate is defined as [54]:

$$T = \frac{\delta}{z}, \quad (2.10)$$

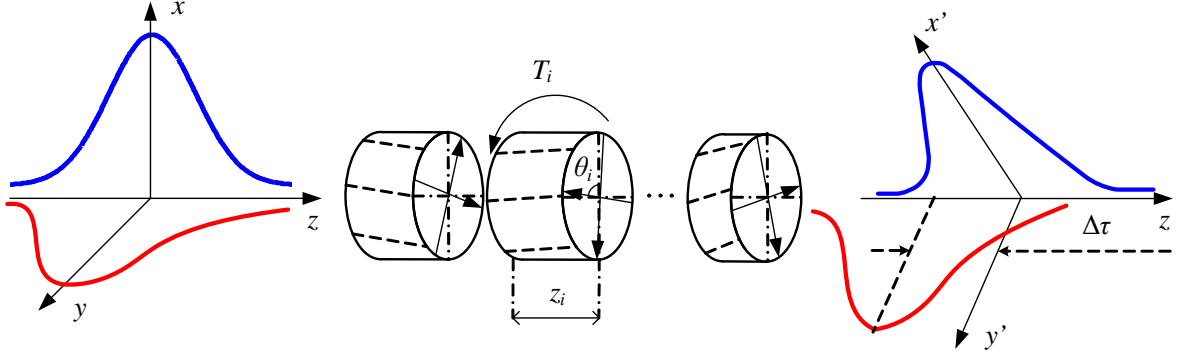


Figure 2.3: Pulse spreading and polarization plane rotation due to birefringence.

where  $\delta$  is the torsion angle. The effect of circular birefringence is a complete rotation of the polarization plane, proportional to the torsion.

In long fibers, the effect of PMD is commonly characterized by the so-called wave-plate model [56], where optical fiber is modeled as a concatenation of numerous birefringent elements (Figure 2.3), each described by the Jones matrix [57]:

$$U_i = \begin{bmatrix} \cos \theta_i & -\sin \theta_i \\ \sin \theta_i & \cos \theta_i \end{bmatrix} \begin{bmatrix} e^{j\Delta\beta z_i/2} & 0 \\ 0 & e^{-j\Delta\beta z_i/2} \end{bmatrix} \begin{bmatrix} \cos \theta_i & \sin \theta_i \\ -\sin \theta_i & \cos \theta_i \end{bmatrix}. \quad (2.11)$$

In Equation (2.11),  $\theta_i$  and  $z_i$  are the fast PSP axis orientation and the length of the  $i$ -th element. Additionally, each element has its polarization plane arbitrarily rotated by  $\Delta\psi_i$ , due to torsion.

To account for PMD, the propagation equation (Equation (2.1)) can be transformed into vector form as follows<sup>1</sup>, assuming that the birefringence is linear, and that the orientation of PSPs is frequency-independent [58]:

$$\frac{\partial \mathbf{A}}{\partial z} = -\frac{\alpha}{2} \mathbf{A} - \Theta(z) \left[ \frac{\Delta\beta_0}{2} \mathbf{A} - \frac{\Delta\beta_1}{2} \frac{\partial \mathbf{A}}{\partial t} \right] - \frac{j\beta_2}{2} \frac{\partial^2 \mathbf{A}}{\partial t^2}, \quad (2.12)$$

where  $\mathbf{A} = [A_x(t, z)A_y(t, z)]^T$  is the vector whose components are the optical field envelopes polarized along the X and Y axis,  $\Theta$  is a  $\theta$ -radian rotation matrix, and  $\Delta\beta_{0,1}$  coefficients are Taylor series expansions of  $\Delta\beta$ . Polarization mode coupling is introduced by  $\Theta$ , accounting for the SOP rotation and the DGD [59].

The changes in PSP and propagation constants along the fiber result in a stochastic behavior of the overall fiber DGD, whose probability density function is approximated by the Maxwellian distribution [60]:

<sup>1</sup>Considering only the linear portion of the propagation equation.

$$p(\Delta\tau) = \frac{32}{\pi^2} \frac{\Delta\tau^2}{\langle\Delta\tau\rangle^3} \exp\left\{-\frac{4\Delta\tau^2}{\pi\langle\Delta\tau\rangle^2}\right\}. \quad (2.13)$$

In Equation (2.13),  $\langle\Delta\tau\rangle$  is the average DGD value, proportional to  $\sqrt{z}$  rather than  $z$ , as in the case of short birefringent elements (see Equation (2.9) for comparison). Thus, an optical signal at the receiver suffers from time-varying DGD, and has constantly changing polarization state and orientation.

### *Second-order PMD*

In the above analysis we treated the optical signal as a monochromatic wave at the carrier frequency, resulting in the first-order PMD model. Birefringence, however, is frequency-dependent and has a non-negligible variation within the signal spectrum, especially for high symbol rates. This variation originates the second-order PMD (SOPMD), defined as the derivative with respect to frequency of the PMD vector  $\mathbf{\Omega} = \Delta\tau(\omega)\hat{q}$ , where  $\hat{q}$  is the unit vector in the fast PSP direction [61]:

$$\text{SOPMD} = \frac{d\mathbf{\Omega}(\omega)}{d\omega} = \frac{d\Delta\tau(\omega)}{d\omega}\hat{q} + \Delta\tau(\omega)\frac{d\hat{q}(\omega)}{d\omega}. \quad (2.14)$$

The first term on the right-hand side of Equation (2.14) is parallel to the PSP, and has a physical meaning of a polarization-dependent chromatic dispersion. The second term is orthogonal to the PSP, and has a physical meaning of inducing signal depolarization [62]. The polarization-dependent chromatic dispersion is a stochastic process, modeled by the following probability density function [62]:

$$p(\Delta\tau_\omega) = \frac{\pi}{4\mu^2} \text{sech}^2\left(\frac{\pi\Delta\tau_\omega}{2\mu^2}\right), \quad (2.15)$$

where  $\Delta\tau_\omega = d\Delta\tau(\omega)/d\omega$ , and  $\mu^2$  is given by:

$$\mu^2 = \frac{\pi}{8} \langle\Delta\tau\rangle^2. \quad (2.16)$$

## **2.2.2 Fiber propagation in nonlinear regime**

The response of an optical fiber becomes nonlinear for intense electromagnetic fields, resulting in nonlinear impairments [63]. Nonlinear effects occur due to the change in the refractive index of the fiber with signal intensity (nonlinear refraction), or due to

inelastic scattering phenomena. Nonlinear refraction is mainly governed by the third-order susceptibility, and is responsible for the, so called, Kerr nonlinearities,<sup>1</sup> which include self-phase modulation (SPM), cross-phase modulation (XPM), and four-wave mixing (FWM). Inelastic scattering, in turn, is responsible for such impairments as stimulated Brillouin scattering (SBS), and stimulated Raman scattering (SRS) [65]. In the following, we concentrate on Kerr nonlinearities as the most relevant for signal propagation study.

To have a better insight on the influence of nonlinearities, let us consider the NLSE with omitted group-velocity-related terms:

$$\frac{\partial A(t, z)}{\partial z} = -\frac{\alpha}{2}A(t, z) + j\gamma|A(t, z)|^2A(t, z), \quad (2.17)$$

$$= -\frac{\alpha}{2}A(t, z) + j\gamma \exp(-\alpha z)|A(t, 0)|^2A(t, z), \quad (2.18)$$

where in the last expression we used the Beer's law (see Section 2.2.1.1). The solution to Equation (2.18) is given by [66]:

$$A(t, z) = A(t, 0) \exp\left(-\frac{\alpha}{2}z + j\gamma|A(t, 0)|^2 L_{eff}(z)\right), \quad (2.19)$$

where

$$L_{eff}(z) = \frac{1 - \exp(-\alpha z)}{\alpha} \quad (2.20)$$

is the fiber effective length that satisfies:

$$P_{in}L_{eff}(L) = \int_{z=0}^L P(z)dz. \quad (2.21)$$

Equation (2.19) shows that the effect of nonlinear impairments is an intensity-dependent phase rotation  $\phi_{NL} = \gamma|A(t, 0)|^2L_{eff}(z)$ . If  $A(t, z)$  represents a single optical channel, this effect is known as self-phase modulation. Observe that SPM is memoryless in a sense that it only depends on the instant signal value. Time-domain phase rotation results in broadening of the signal spectral content.

In PM system, nonlinear polarization coupling occurs, leading to the so-called polarization cross-talk, which, for large birefringence fibers (which is true for single-mode fibers in long-haul scenario), may be modeled as [56]:

$$\frac{\partial}{\partial z} \begin{pmatrix} A_x \\ A_y \end{pmatrix} = -\frac{\alpha}{2} \begin{pmatrix} A_x \\ A_y \end{pmatrix} + j\gamma \begin{pmatrix} |A_x|^2 + \frac{2}{3}|A_y|^2 & 0 \\ 0 & |A_y|^2 + \frac{2}{3}|A_x|^2 \end{pmatrix}. \quad (2.22)$$

---

<sup>1</sup>Named after John Kerr, who discovered them in 1877 [64].

Finally, the vectorial form of NLSE for a single-field transmission, also known as the coupled NLSE (CNLSE) is given by [59, 67]:

$$\begin{aligned} \frac{\partial \mathbf{A}}{\partial z} = & -\frac{\alpha}{2} \mathbf{A} - \Theta(z) \left[ \frac{\Delta\beta_0}{2} \mathbf{A} - \frac{\Delta\beta_1}{2} \frac{\partial \mathbf{A}}{\partial t} \right] - \frac{j\beta_2}{2} \frac{\partial^2 \mathbf{A}}{\partial t^2} \\ & + j\gamma \left[ |\mathbf{A}|^2 \mathbf{A} - \frac{1}{3} (\mathbf{A}^H \sigma_3 \mathbf{A}) \sigma_3 \mathbf{A} \right], \end{aligned} \quad (2.23)$$

where  $\sigma_3$  is the Pauli spin matrix:

$$\sigma_3 = \begin{bmatrix} 0 & -j \\ j & 0 \end{bmatrix}, \quad (2.24)$$

and  $\mathbf{A}$  and  $\Theta$  are defined as in Equation (2.12).

In WDM systems, two additional phenomena occur due to the co-propagating channels. First one is the cross-phase modulation, where co-propagating channels exercise phase rotation on one another. The second one is the four-wave mixing, where mixing products from three co-propagating waves at angular frequencies  $\omega_1, \omega_2$  and  $\omega_3$  generate a fourth wave at  $\omega_4$ , being  $\omega_4 = \omega_1 \pm \omega_2 \pm \omega_3$  [65]. In order to build up along the fiber, both effects require phase matching between the involved channels.

Disregarding the polarization coupling effects for simplicity, the nonlinear Schrödinger equation for the  $n^{\text{th}}$  channel in a WDM system can be written as [56]:

$$\begin{aligned} \frac{\partial A_n}{\partial z} = & - \underbrace{\frac{\alpha}{2} A_n}_{\text{Attenuation}} - \underbrace{(\beta_{1,n} - \beta_{1,ref}) \frac{\partial A_n}{\partial t}}_{\text{Delay}} - \underbrace{\frac{j\beta_{2,n}}{2} \frac{\partial^2 A_n}{\partial t^2}}_{\text{Dispersion}} + \underbrace{\frac{j\beta_{3,n}}{6} \frac{\partial^3 A_n}{\partial t^3}}_{\text{Dispersion slope}} \\ & + j\gamma A_n \left\{ \underbrace{|A_n|^2}_{\text{SPM}} + 2 \underbrace{\sum_{i=1, i \neq n}^N |A_i|^2}_{\text{XPM}} \right\} \\ & + \underbrace{j\gamma \sum_{n=i+j-k; i, j \neq k} A_i A_j A_k^* \exp(-j\Delta k z)}_{\text{FWM}}. \end{aligned} \quad (2.25)$$

where  $\beta_{1,ref}$  is the propagation constant of the reference channel for the retarded time frame, and  $\Delta k$  is the phase constant, given by:

$$\Delta k = -\beta_2(\omega_i - \omega_k)(\omega_j - \omega_k) - \beta_3(\omega_i - \omega_k)(\omega_j - \omega_k)((\omega_i + \omega_j)/2 - \omega_0). \quad (2.26)$$

It is important to observe that Equation (2.1) can be seen as equivalent of Equation (2.25) if the, so called, total field approach is used, where  $A = A_1 + A_2 + \dots A_N$ . Conversely, different spectral portions of the same signal in a single-channel transmission

also interact through XPM and FWM. Those interactions are sometimes referred to as the intra-channel XPM (iXPM) and intra-channel FWM (iFWM) [59].

Although previous discussion helps to understand the nonlinear mechanisms, in general, linear and nonlinear impairments interplay during propagation, and cannot be treated separately. The NLSE (Equation (2.1)) cannot be solved analytically, and so, numerical methods are commonly used to model nonlinear propagation. Two methods that are found in the literature are the split-step Fourier method (SSFM) [63], and Volterra series transfer function [68]. The most renowned split-step Fourier method will be presented later in Chapter 3, in the scope of nonlinear compensation by DSP.

Recently, the so called, Gaussian noise model of the nonlinear impairments (NLI) in dispersion unmanaged links was proposed in [69], later validated by extensive simulations and experiments [70]. In its essence, the model states that the effect of NLI could be modeled as excess additive Gaussian noise. Therefore, the nonlinear noise can be added to ASE noise, and its impact on system performance could be assessed through a modified signal-to-noise-ratio. The great advantage of this model is that it allows to statistically characterize optical signal without resorting to complex and long numerical simulations. Also, one of the consequences of the model is that it allows to obtain optimal signal launch power, so that the OSNR (including linear and nonlinear noise contributions) is maximized. Nevertheless, due to its stochastic nature, the model cannot be explored to compensate for the nonlinearities.

## 2.3 THE RECEIVER

A typical coherent receiver comprises the following subsystems: a front-end receiver, implemented in integrated photonics, whose function is to convert optical signal to electrical domain; a radio-frequency analog module, containing transimpedance amplifiers; an application-specific integrated circuit (ASIC)-implemented module with analog-to-digital converters and DSP blocks; and an ASIC module (or modules) that contains a FEC decoder and transport/network-level functionalities. In this section we address the front-end receiver, leaving a detailed explanation of the DSP blocks for the next chapter.

The front-end of a polarization-diversity optical receiver linearly maps optical field to the electrical domain. Additionally, it performs a passband-to-baseband (or to intermediate frequency) down-conversion. In polarization-multiplexed systems, this is

commonly done by an array of two quadrature receivers, whose architecture is illustrated in Figure 2.4.

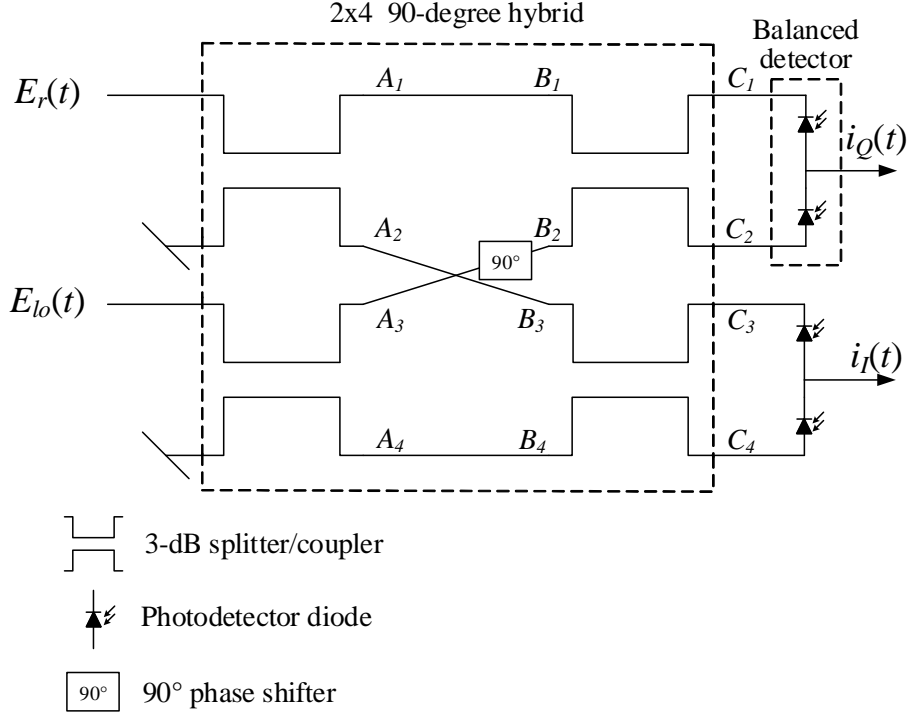


Figure 2.4: Coherent quadrature receiver.

The optical fields of the received signal,  $E_r(t)$ , and the local oscillator,  $E_{lo}(t)$ , are divided by two power splitters, whose transfer function is given by [71]:

$$\mathbf{H}_{coupler} = \frac{1}{\sqrt{2}} \begin{bmatrix} 1 & 1 \\ 1 & -1 \end{bmatrix}, \quad (2.27)$$

to be combined within a 2x4 90-degree optical hybrid. Hence, the fields in  $A_1$ - $A_4$  and  $B_1$ - $B_4$  (see Figure 2.4) are:

$$E_{A_1}(t) = \frac{1}{\sqrt{2}} E_r(t), \quad (2.28)$$

$$E_{A_2}(t) = \frac{1}{\sqrt{2}} E_r(t), \quad (2.29)$$

$$E_{A_3}(t) = \frac{1}{\sqrt{2}} E_{lo}(t), \quad (2.30)$$

$$E_{A_4}(t) = \frac{1}{\sqrt{2}} E_{lo}(t), \quad (2.31)$$

and

$$E_{B_1}(t) = \frac{1}{\sqrt{2}}E_r(t), \quad (2.32)$$

$$E_{B_2}(t) = \frac{j}{\sqrt{2}}E_{lo}(t), \quad (2.33)$$

$$E_{B_3}(t) = \frac{1}{\sqrt{2}}E_r(t), \quad (2.34)$$

$$E_{B_4}(t) = \frac{1}{\sqrt{2}}E_{lo}(t), \quad (2.35)$$

respectively. Subsequent coupling yields:

$$E_{C_1}(t) = \frac{1}{2}E_r(t) + \frac{j}{2}E_{lo}(t), \quad (2.36)$$

$$E_{C_2}(t) = \frac{1}{2}E_r(t) - \frac{j}{2}E_{lo}(t), \quad (2.37)$$

$$E_{C_3}(t) = \frac{1}{2}E_r(t) + \frac{1}{2}E_{lo}(t), \quad (2.38)$$

$$E_{C_4}(t) = \frac{1}{2}E_r(t) - \frac{1}{2}E_{lo}(t). \quad (2.39)$$

Finally, two balanced detectors produce the output photocurrents:

$$\begin{aligned} i_Q(t) &= R|E_{C_1}|^2 - R|E_{C_2}|^2 \\ &= R\left|\frac{1}{2}E_r(t) + \frac{j}{2}E_{lo}(t)\right|^2 - R\left|\frac{1}{2}E_r(t) - \frac{j}{2}E_{lo}(t)\right|^2, \end{aligned} \quad (2.40)$$

$$\begin{aligned} i_I(t) &= R|E_{C_3}|^2 - R|E_{C_4}|^2 \\ &= R\left|\frac{1}{2}E_r(t) + \frac{1}{2}E_{lo}(t)\right|^2 - R\left|\frac{1}{2}E_r(t) - \frac{1}{2}E_{lo}(t)\right|^2, \end{aligned} \quad (2.41)$$

where  $R$  is the photodetector responsivity. The electric fields of the received signal and the LO are [71]:

$$E_r(t) = [A_s(t)e^{j\phi_s(t)} + n_s(t)]e^{j\omega_c t}, \quad (2.42)$$

$$E_{lo}(t) = [A_{lo} + n_{lo}(t)]e^{j\omega_{lo} t}, \quad (2.43)$$

where  $A_s(t)$  and  $\phi_s(t)$  are the amplitude and the phase of the optical signal;  $A_{lo}$  is the LO amplitude; and  $\omega_c$  and  $\omega_{lo}$  are the optical carrier and the LO angular frequencies. Also,  $n_s(t)$  and  $n_{lo}(t)$  are the signal and the LO noise processes. Using the identity:

$$|z + k|^2 = |z|^2 + |k|^2 + 2\Re\{zk^*\}, \quad z, k \in \mathbb{Z}, \quad (2.44)$$



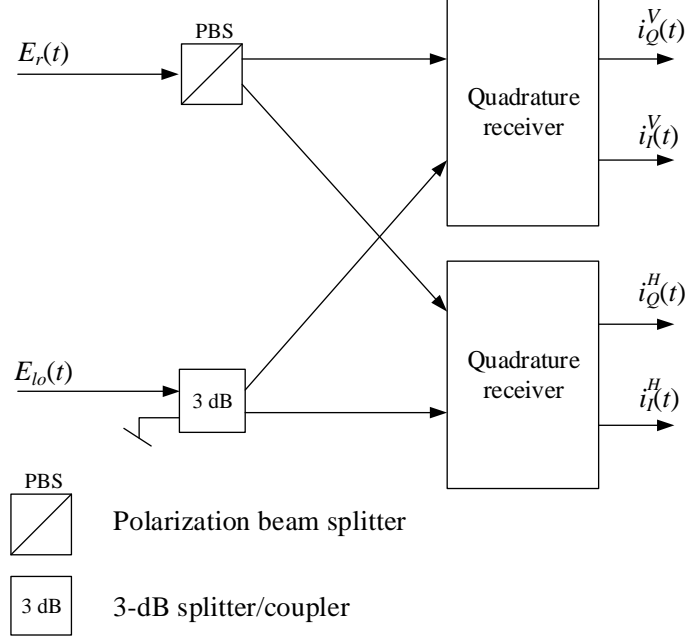


Figure 2.5: Polarization-diversity receiver.

with  $\Re\{\cdot\}$  denoting the real part of  $\{\cdot\}$ , and neglecting shot and thermal noise components, yields:

$$i_Q(t) = R A_{lo} A_s(t) \sin(\omega_{IF} + \phi_s(t)) + R \Re \{ [A_{lo} n_s(t) + A_s(t) n_{lo}(t) e^{j\phi_s(t)}] e^{j(\omega_{IF} + \frac{\pi}{2})} \}, \quad (2.45)$$

$$i_I(t) = R A_{lo} A_s(t) \cos(\omega_{IF} + \phi_s(t)) + R \Re \{ [A_{lo} n_s(t) + A_s(t) n_{lo}(t) e^{j\phi_s(t)}] e^{j\omega_{IF}} \}, \quad (2.46)$$

where  $\omega_{IF}$  represents the intermediate frequency, defined as the beat frequency of  $\omega_c$  and  $\omega_{lo}$ .

In practical systems, the LO power is usually much higher (about 15 dB) than signal power, and  $\sigma_{n_s}^2 \gg \sigma_{n_{lo}}^2$ , so that:

$$A_{lo} n_s(t) + A_s(t) n_{lo}(t) e^{j\phi_s(t)} \approx A_{lo} n_s(t). \quad (2.47)$$

Thus, further assuming homodyne reception (that is,  $\omega_{IF} = 0$ ):

$$i_Q(t) \approx R A_{lo} A_s(t) \sin(\phi_s(t)) + R \Re \{ A_{lo} n_s(t) e^{j\frac{\pi}{2}} \}, \quad (2.48)$$

$$i_I(t) \approx R A_{lo} A_s(t) \cos(\phi_s(t)) + R \Re \{ A_{lo} n_s(t) \}. \quad (2.49)$$

In this way, the phase information,  $\phi_s(t)$ , is mapped onto the  $i_I$  e  $i_Q$  photocurrents, corresponding to the in phase and quadrature components of the received signal, and the LO-spontaneous emission beat noise has Gaussian distribution.

As mentioned, a polarization-diversity receiver, depicted in Figure 2.5, uses an array of two quadrature receiver structures. Here, a polarization beam splitter (PBS) separates the horizontally- (H) and the vertically- (V) polarized signal components, which carry information of both polarization tributaries, X-pol. and Y-pol., due to the arbitrary polarization rotation within the fiber (see Section 2.2.1.2). Thus, the polarization-diversity receiver output contains four (real-valued) electrical photocurrents,  $i_I^V(t)$ ,  $i_Q^V(t)$ ,  $i_I^H(t)$  and  $i_Q^H(t)$ .

## Chapter 3 DIGITAL SIGNAL PROCESSING IN COHERENT OPTICAL RECEIVERS

The four front-end outputs,  $i_I^V(t)$ ,  $i_Q^V(t)$ ,  $i_I^H(t)$  and  $i_Q^H(t)$ , are current-to-voltage-converted by a set of transimpedance amplifiers (TIAs), and digitized by a set of analog-to-digital converters (ADCs). Commonly, ADC sample rate is  $2R_s$  (being  $R_s$  the symbol rate), though, an oversampling rate of 3/2 is, generally, sufficient for CD and first-order PMD compensation [72]. Ultra-high-speed systems often dispense the use of anti-aliasing filters prior to digitalization, because bandwidth limitations of the analog devices (photodetectors, TIAs, ADCs) implicitly perform low-pass (LP) filtering. The resulting signals undergo a chain of DSP procedures to extract the transmitted information, as depicted in Figure 3.1.

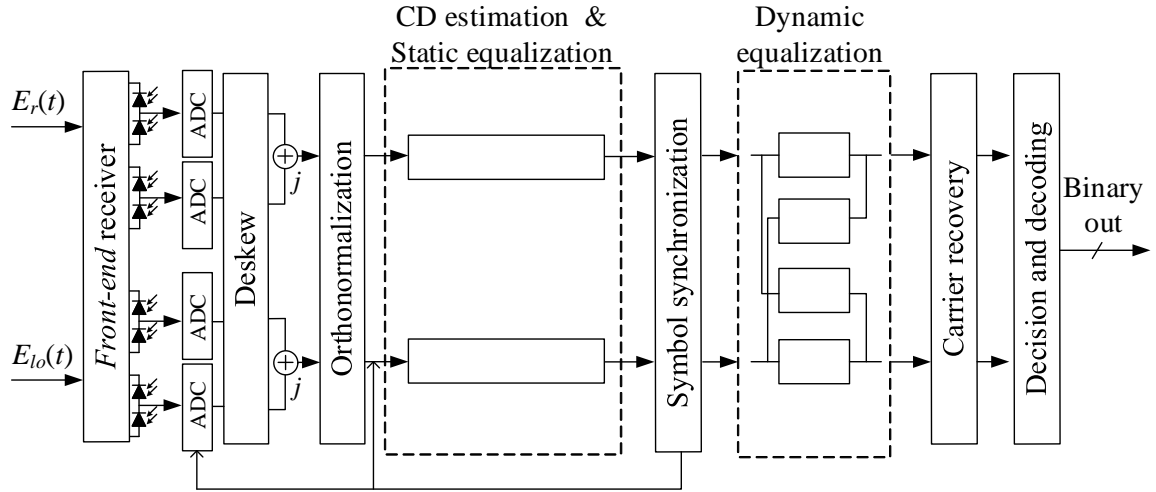


Figure 3.1: Chain of coherent receiver DSP algorithms for information recovery.

First, the deskew block compensates for possible length mismatches in optical or electrical paths of the four ADC outputs. Those mismatches result in signals' temporal misalignment, known as skew, which may arise due to imperfections in the manufacturing process, or design spacial constraints. The resulting digital streams are pairwise combined into two complex signals corresponding to the V and H polarization tributaries, and undergo an orthonormalization process, designed to eliminate any residual DC components, and compensate for amplitude imbalances and optical hybrid imperfections. The following subsystem estimates and compensates for the accumulated CD. Here, both estimation and compensation functionalities are grouped within the

same block, because they are typically implemented by the same hardware. Symbol synchronization compensates for the difference between the Tx and the Rx (in particular, ADC) clock frequencies and phase offset, as well as for a low-frequency (typically, of several hundreds of kHz) jitter<sup>1</sup> components. Timing error detection requires inter-symbol interference (ISI) compensation, and thus performed after static (or dynamic) equalization. Timing error correction, however, may be performed prior to (distributed system), or after (single block) static equalization using digital interpolators and fine ADC clock tuning, depending on latency considerations for a particular design. The following multiple-in multiple-out (MIMO) dynamic equalizer separates the two polarization-multiplexed signals, compensates for any residual CD and polarization-dependent propagation effects, and filters out noise to maximize SNR. Carrier recovery block compensates for the frequency offset between the optical carrier and the LO, and for the phase noise, generated by Tx and Rx lasers. Finally, the decision and decoding subsystem recovers the transmitted binary streams for subsequent error correction and network-layer management. Naturally, the description in Figure 3.1 may substantially vary for a particular implementation.

In the rest of this chapter, we review the main features and algorithms behind the DSP blocks.

### 3.1 DESKEW

Skew values are usually known from the design characteristics, or measured in lab prototypes, and, in general, do not require estimation. The deskew block consists of finite impulse response (FIR) filters that temporally align signal components, commonly, by implementing the Lagrangian interpolation [74], described hereafter.

Given  $N + 1$  signal values  $s_0 \dots s_N$  at instants  $t_0 \dots t_N$ , where  $N$  is the order of the interpolation polynomial, the signal value at an arbitrary instant  $t$  ( $t_0 \leq t \leq t_N$ ) is computed as:

$$s_t = \sum_{n=0}^N L_n(t) s_n, \quad (3.1)$$

---

<sup>1</sup>Timing jitter is commonly defined as the short term variations of the significant instants of a digital signal from their ideal positions in time [73].

where the weighting functions,  $L_n$ , are given by:

$$L_n = \prod_{m=0, m \neq n}^N \frac{t - t_m}{t_n - t_m}. \quad (3.2)$$

Note that Equation 3.1 is seamlessly implemented by a transversal filter structure with tap weights computed using Equation 3.2. Typically, 4- or 5-tap structures are used.

### 3.2 ORTHONORMALIZATION

Ideally, the I and Q components at the receiver output are statistically uncorrelated. Nevertheless, front-end imperfections may provoke amplitude and phase mismatches that destroy I-Q orthogonality, penalizing system performance [75]. These imperfections include unbalanced splitting ratios, inaccuracies of the  $90^\circ$  phase shifter, and mismatching between the photodetector responsivity values.

After eliminating the possible residual DC by subtracting the mean signal values, estimated, e.g., via moving average filters, the I and Q signal components undergo the Gram-Schmidt orthogonalization procedure (GSOP) for each polarization. The received I and Q signal components, seen as vectors in a two-dimensional signal-space, are converted by GSOP into orthonormal basis functions,  $\phi_1$  and  $\phi_2$ , as [76]:

$$\phi_1[k] = \frac{i_I[k]}{\|i_I[k]\|}, \quad (3.3)$$

$$\phi_2[k] = \frac{i_Q[k] - \hat{i}_Q[k]}{\|i_Q[k] - \hat{i}_Q[k]\|}, \quad (3.4)$$

where

$$\hat{i}_Q[k] = \langle i_Q[k], \phi_1[k] \rangle = E\{i_Q[k] \phi_1[k]\} \quad (3.5)$$

is the projection of  $i_Q[k]$  onto the unidimensional subspace spanned by  $\phi_1[k]$ ,  $\mathcal{S}_1 = \text{span}\{\phi_1[k]\}$ . In Equations (3.3-3.4),  $\|\mathbf{x}\| = \sqrt{E\{\mathbf{x}^2\}}$  is the *norm* of  $\mathbf{x}$ .

The idea behind the GSOP is as follows: the first vector,  $i_I[k]$  (alternatively,  $i_Q[k]$ ) is taken as the reference basis function after its normalization (see Equation (3.3)). Since  $\hat{i}_Q[k] \in \mathcal{S}_1$ , it follows, according to the *Projection Theorem* [76], that  $(i_Q[k] - \hat{i}_Q[k]) \perp \mathcal{S}_1$ . From Equation (3.4),  $\phi_2[k]$  is normalized, and satisfies:  $\phi_2[k] \perp \phi_1[k]$ .

### 3.3 CD ESTIMATION

Normally, CD estimation is performed upon the system start-up, or after optical signal rerouting, as during failure. As a consequence, *pro tempore*, the DSP is not required to support online CD estimation that would be performed in parallel without interfering with the steady-state system operation. This led to development of the, so-called, scanning algorithms for CD estimation, because, in spite of increasing system start-up time, they allow to take advantage of the existing CD-compensation hardware. These algorithms scan over a range of preset dispersion values, adjusting the CD equalizer accordingly, in attempt to minimize a certain cost function. As an example, we describe a time-error-detection (TED)-based scanning algorithm, proposed in [77]. In particular, the authors use a Gardner time error detector (GTED) [78], whose operation principle is explained later in Section 3.5.1. The advantage of this algorithm is that, in addition to the CD compensation, it also uses the TED hardware, further increasing hardware efficiency.

The GTED requires a sampling rate of two samples per symbol, and uses three signal samples to produce a single error estimate. Thus, an  $i$ -th block of  $N+1$  samples,  $[y_0^i, y_1^i, \dots, y_N^i]$  yields  $N/2$  individual error estimates,  $[e_1^i, e_2^i, \dots, e_{N/2}^i]$ , as depicted in Figure 3.2.

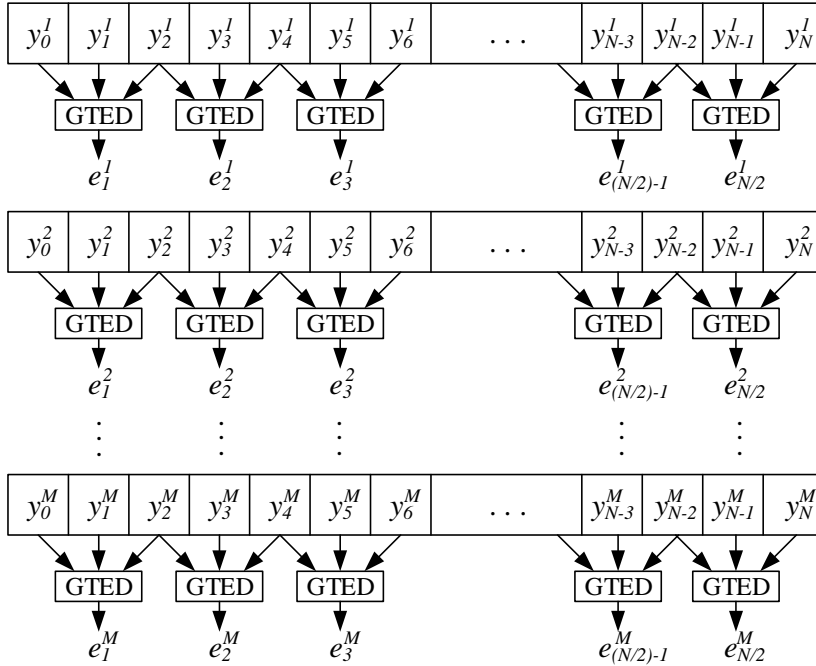


Figure 3.2: Sample mapping for GTED-based CD estimation.

Scanning through the range of accumulated CD values aims to minimize the fol-

lowing cost function:

$$J_{\text{CDE-GTED}} = \sum_{i=1}^M \left[ \frac{2}{N} \sum_{j=1}^{N/2} \left( e_j^i - \frac{2}{N} \sum_{k=1}^{N/2} e_k^i \right)^2 \right]. \quad (3.6)$$

Observe that the expression between the square brackets in Equation (3.6) is simply the variance of the  $i$ -th error vector  $[e_1^i, e_2^i, \dots, e_{N/2}^i]$ . In order to converge, GTED requires that there be no, or little ISI; thus it is sensitive to CD, and requires that most of the accumulated CD be compensated. For example, in PM-QPSK non-return-to-zero (NRZ) systems, the accumulated CD tolerance of GTED is about 300 ps/nm [79], and should be much smaller for Nyquist pulses with weakly pronounced transitions characteristic.

The key idea behind the algorithm is that, in presence of CD, individual GTEDs produce random error estimations, and so, the variance in Equation (3.6) is high. Conversely, when CD is compensated, individual error estimates  $[e_1^i, e_2^i, \dots, e_{N/2}^i]$  converge to a single value, resulting in a steep drop of the variance. The external summation in  $i$  over  $M$  values in Equation (3.6) is designed to reduce the effect of the changes in timing error within the data block, as would occur if instead of  $M$  blocks of  $N+1$  samples, a single  $M \times (N+1)$ -sample length block were used.

A different scan-based CD estimation technique uses the error signal of the constant-modulus algorithm (see Section 3.6.2.3) as the cost function [80]. The constant-modulus algorithm (CMA) is used to blindly (that is, without using a training sequence) update the dynamic equalizer (DE) coefficients. Since DE length is usually much smaller than the CD-induced pulse broadening, CMA is unable to converge, unless the accumulated CD is almost fully compensated. Alternatively, in [81] it was shown that signal peak-to-average power ratio (PAPR) increases with the accumulated CD, and thus, can also be used as a CD-minimizing cost function.

The scanning technique can also be optimized for faster performance. Thus, in [80], the scanning is performed in two steps: coarse scanning with scan-step of a few hundreds of ps/nm; and fine scanning around value found in the first step, with scan-step of a few dozens of ps/nm.

Although the increased CD estimation time of the scanning algorithms appears to comply with startup specifications of the state-of-the-art systems, it is likely that advanced networking features would soon require fast online CD estimation with much tighter performance specifications. In this scope, a notable work by Sui et al. proposed a single-step estimation algorithm using the signal power auto-correlation [82]. Essentially, the authors demonstrated that there exists a mathematical dependency between the time delay that corresponds to the maximum value of the signal power auto-correlation function and accumulated CD.

### 3.4 CD COMPENSATION

Chromatic dispersion compensation is performed by static (also known as bulk) equalizers, separately for each polarization. Generally speaking, the equalizers are designed to invert the CD transfer function of Equation (2.7), and can be implemented either in time, or frequency domain. In-depth analysis of the CD equalizer design, as well as the computational complexity implications, are later presented in Chapter 4.

### 3.5 SYMBOL SYNCHRONIZATION

The purpose of symbol synchronization in digital communications is to interpolate the signal value at the instants of maximum eye opening, to maximize noise immunity [83]. Since the ADC and Tx symbol clocks run independently, two types of synchronization errors are produced: the timing (phase) error, and the clock (frequency) error. The timing error arises when the ADC clock is precisely frequency-synchronized with the symbol clock (or multiple of the symbol clock for oversampled signals), but with a constant phase shift, manifested as a fix sample timing error,  $\Delta\tau$ . This type of synchronism error is not of a concern for systems that employ fractionally-spaced adaptive equalization, because equalizer filters seamlessly interpolate the optimal sampling instants. Conversely, the clock error results from the small frequency offsets between the symbol and ADC clocks, commonly characterized in parts-per-million (ppm). Here, the deviation from the optimal sampling instant constantly increases, and eventually leads to equalizer convergence failure. Additionally, deterministic and random components of the clock jitter introduce short term sampling time variations [84], penalizing signal quality.

A typical digital feedback-based symbol synchronization system, depicted in Figure 3.3 (adapted from [79, 85]), consists of a sample buffer, implemented as a serial-in, parallel-out shift register, digital interpolator, timing error detector (TED), a loop filter, and a numerically-controlled oscillator. In the following, we describe the operation principle of these blocks.



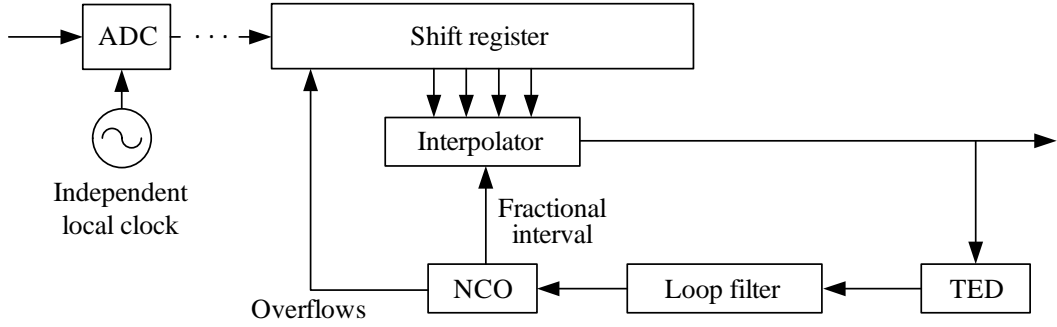


Figure 3.3: Digital timing recovery system. ADC – analog-to-digital converter; NCO – numerically-controlled oscillator; TED – timing error detector (Adapted from [79,85]).

### 3.5.1 Timing error detector

The timing error detector provides the tendency and the direction of the timing error, rather than the exact value [79]. In coherent optical systems, a common choice is the earlier mentioned Gardner algorithm [78], due to its computational simplicity and immunity to carrier phase. In addition, it only requires an oversampling rate of two samples per symbol.

The Gardner error signal for the  $n$ -th symbol is computed as [78]:

$$\begin{aligned} e_n &= y_{2k-1}^I (y_{2k}^I - y_{2k-2}^I) + y_{2k-1}^Q (y_{2k}^Q - y_{2k-2}^Q) \\ &= \Re \{ y_{2k-1}^* (y_{2k} - y_{2k-2}) \}, \quad n = 2k. \end{aligned} \quad (3.7)$$

In Equation (3.7),  $y^{I:Q}$  are the asynchronous TED input samples for the I and Q signal components, and  $n; k$  are the symbol and sample temporal indices, respectively. The algorithm was developed for BPSK- and QPSK-modulated signals, though it is also employed for mQAM with some performance penalties. In its essence, GTED relies on the symmetry of the BPSK signal around the maxima/minima values. The complete derivation of the algorithm is extensively described in [78].

The operating principle of GTED is shown in Figure 3.4, for a  $-1 \rightarrow 1$  transition of a band-limited BPSK signal, marking the samples  $y_{2k-2}$ ,  $y_{2k-1}$ , and  $y_{2k}$ . For  $\Delta\tau = 0$  (correct sampling),  $\Delta\tau > 0$  (late sampling), and  $\Delta\tau < 0$  (advanced sampling), depicted in Figures 3.4(a-c), respectively:

$$e_n = 0 \cdot (1 - (-1)) = 0; \quad (3.8)$$

$$e_n = 0.2 \cdot (0.8 - (-0.8)) = 0.32 > 0; \quad (3.9)$$

$$e_n = -0.2 \cdot (0.8 - (-0.8)) = -0.32 < 0. \quad (3.10)$$

Timing error detector is commonly characterized by the so-called S-curve, obtained by sweeping  $\Delta\tau$  over the interval  $[-0.5T, 0.5T]$ , being  $T$  the symbol period. An

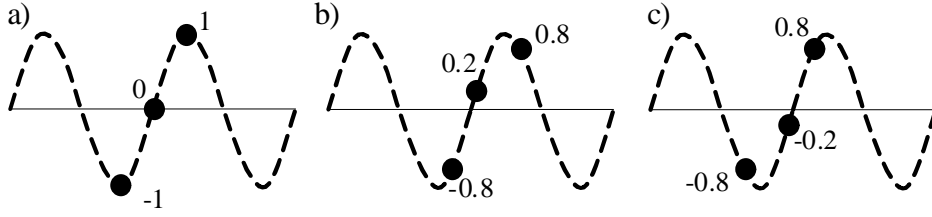


Figure 3.4: Operating principle of the GTED: (a) correct sampling ( $\Delta\tau = 0$ ); (b) late sampling ( $\Delta\tau > 0$ ); advanced sampling ( $\Delta\tau < 0$ ).

illustrative S-curve is depicted in Figure 3.5. The robustness of GTED depends on the amplitude of the S-curve, affected by the residual CD and PMD; and thus, time variant. Observe that  $\Delta\tau$  cannot be inferred uniquely from the S-curve.

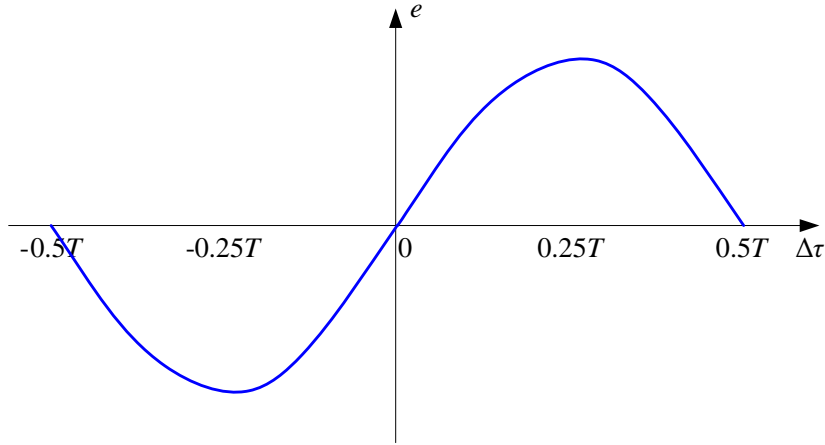


Figure 3.5: Typical S-curve.

While GTED has a satisfactory performance for NRZ and RZ pulses, it is severely degraded by Nyquist pulse shaping, especially for small roll-off values [86], requiring more robust solutions for transmit-side DSP-enabled transponders. One such solution, a modified Gardner detector (MGTED), was proposed in [87]. The error signal for MGTED is computed as:

$$\begin{aligned}
 e_n &= y_{2k-1}y_{2k-1}^*(y_{2k}y_{2k}^* - y_{2k-2}y_{2k-2}^*) \\
 &= |y_{2k-1}|^2(|y_{2k}|^2 - |y_{2k-2}|^2), \quad n = 2k.
 \end{aligned} \tag{3.11}$$

Contrary to the GTED, the MGTED shows best performance at roll-off values near zero, gradually degrading as roll-off increases [87].

### 3.5.2 Loop filter and NCO

Even when averaged over many samples, the GTED presents phase noise, due to jitter, PMD, and non-linear behavior of the S-curve. To extract stable components, a loop filter that implements a proportional-integral (PI) controller, shown in Figure 3.6, is commonly employed [79]. The PI controller consists of two branches, where the proportional branch multiplies the GTED error by a constant, and the integral branch, implemented recursively, cumulatively adds all of the branch past values. The loop filter output (also referred to as the control word [85]) for the  $n$ -th symbol is given by:

$$W_n = e_n k_p + k_i \sum_{l=0}^{n-1} e_{n-l}. \quad (3.12)$$

The control word,  $W_n$  has a physical meaning of synchronizer's estimate of the average frequency of interpolation, expressed relative to the sampling frequency [85]. The design of the proportional and integral branch parameters,  $k_p$  and  $k_i$ , determines the stability of the symbol synchronization block, its convergence speed and frequency response.

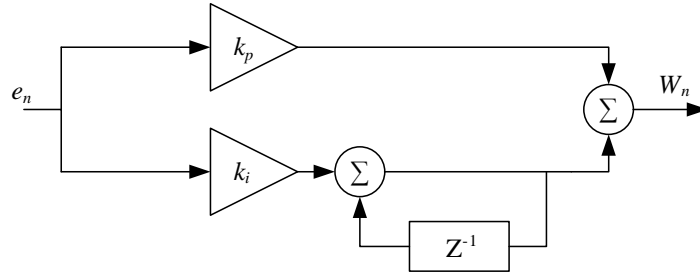


Figure 3.6: PI controller of the loop filter.

The numerically-controlled oscillator translates the control word into a fractional interval,  $\mu_n \in [0, 1)$ , to feed the numerical interpolator, computed as [85]:

$$\mu_n = \frac{\text{NCO}_n}{W_n}, \quad (3.13)$$

where  $\text{NCO}_n$  is given by the difference equation:

$$\text{NCO}_n = [\text{NCO}_{n-1} - W_{n-1}]_{\text{mod } 1}, \quad (3.14)$$

The  $\text{mod } 1$  operation ensures that  $\mu_n$  is always in  $[0, 1)$ , shifting the buffer via the overflows signal (see Figure 3.3).

### 3.5.3 Interpolator

The principle of digital interpolator implementation was earlier discussed in Section 3.1. Commonly, third order Lagrange polynomials are used (4-tap FIR structure), which, for a desired fractional interval  $\mu$ , resume in the following filter tap weights [88]:

$$\begin{aligned}
 w_{-2} &= \frac{(\mu+1)\mu(\mu-1)}{6} = \frac{1}{6}\mu^3 - \frac{1}{6}\mu; \\
 w_{-1} &= \frac{(\mu+1)\mu(\mu-2)}{-2} = -\frac{1}{2}\mu^3 + \frac{1}{2}\mu^2 + \mu; \\
 w_0 &= \frac{\mu(\mu-1)(\mu-2)}{2} = \frac{1}{2}\mu^3 - \mu^2 - \frac{1}{2}\mu + 1; \\
 w_1 &= \frac{\mu(\mu-1)(\mu-2)}{-6} = -\frac{1}{6}\mu^3 + \frac{1}{2}\mu^2 - \frac{1}{3}\mu,
 \end{aligned} \tag{3.15}$$

where the interpolation instant is  $t = (i + \mu)T_{sa}$ , being  $i \in \{-2, -1, 0, 1\}$  the tap index, and  $T_{sa}$  the sample period.

## 3.6 DYNAMIC EQUALIZATION

### 3.6.1 DE architecture

The role of the dynamic equalizer is to extract the two polarization tributaries, X-pol. and Y-pol., from their linear combinations; to compensate for the polarization-dependent propagation impairments, as well as any residual CD; and to filter out additive noise. Commonly, a complex  $2 \times 2$  multiple-in & multiple-out (MIMO) “butterfly” structure, composed of four time-domain FIR N-tap transversal filters,  $\mathbf{w}_{ij}$ ,  $i, j \in \{X, Y\}$ , is employed, as depicted in Figure 3.7. Here,  $X_{in}, Y_{in}$ , are complex inputs:  $X_{in} = X_{in}^I + jX_{in}^Q$  and  $Y_{in} = Y_{in}^I + jY_{in}^Q$ .

With the increase of the symbol rate and use of Nyquist pulses, the skew-induced imbalances between the four signal components became more disruptive, leading to development of MIMO structures with additional degrees of freedom for fine skew compensation. Figures 3.8(a-b) show a real-valued  $4 \times 4$  MIMO [89], and a complex-valued  $4 \times 2$  [90] structures. Here, the key idea is to decouple the I and Q signal components within the equalizer, to allow them to converge to optimal mutual delay. Additional care must be taken during earlier static equalization, so as not to result in

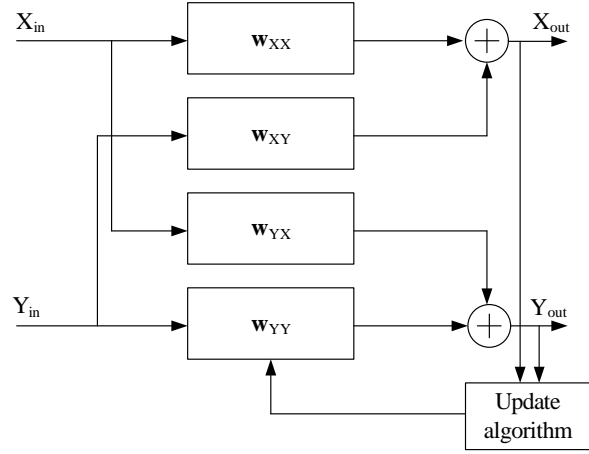


Figure 3.7:  $2 \times 2$  MIMO “butterfly”-structured dynamic equalizer.

an undesirable I-Q mixing [90].

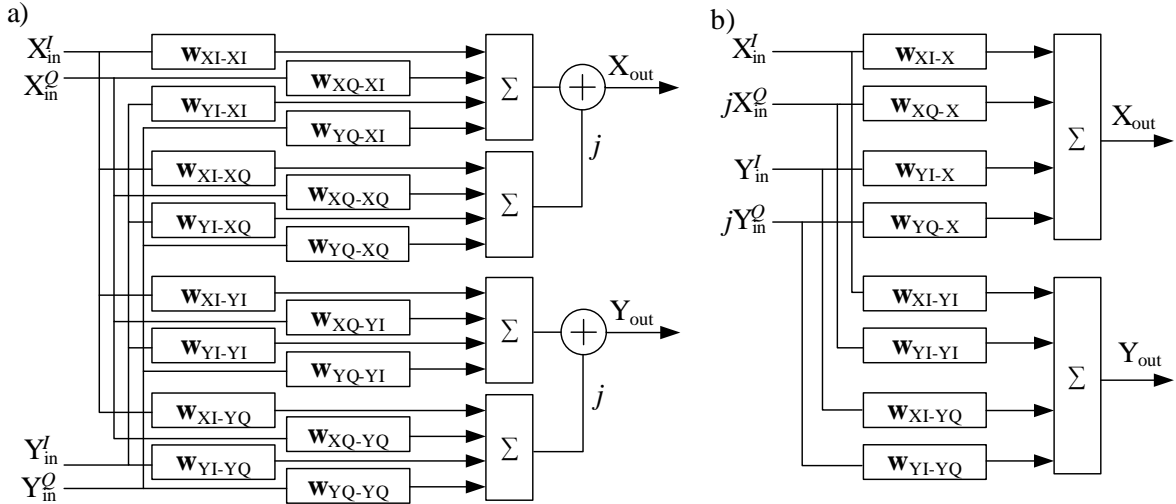


Figure 3.8: Skew compensating DE structures: (a) real  $4 \times 4$  MIMO [89]; (b) complex  $4 \times 2$  MIMO [90].

### 3.6.2 Adaptive equalization

Due to the stochastic nature of the optical channel, coherent systems rely on adaptive equalization that allows to track temporal signal changes. In the following we describe two of the most commonly used in long- and ultra-long-haul systems adaptive algorithms, namely, the decision-directed least mean squares (DD-LMS), and the constant modulus algorithm (CMA). They belong to the class of unsupervised algorithms, in a sense that they do not require a training sequence for equalization.

### 3.6.2.1 Stochastic steepest descent method

Both algorithms are implemented via the iterative stochastic gradient (or steepest) descent method for equalizer coefficient update, given by [91]:

$$\mathbf{w}_k = \mathbf{w}_{k-1} - \mu \nabla J_{k-1}(\mathbf{w}), \quad (3.16)$$

where  $\mathbf{w}_k = [w_k \ w_{k-1} \ \cdots \ w_{k-N+1}]^T$  is the vector of the equalizer tap weights at the  $k$ -th instant, and  $J(\mathbf{w})$  is the algorithm-dependent cost function we wish to minimize. The step-size,  $\mu$ , controls algorithm stability, and provides a trade-off between equalizer tracking capabilities and the residual error magnitude. The key idea behind the stochastic descent is that the gradient of the cost function be approximated by its instant estimated values. That is:

$$\nabla J(\mathbf{w}) \approx E \{ \nabla J_k(\mathbf{w}) \}, \quad k = \{0, 1, \dots, \infty\}. \quad (3.17)$$

### 3.6.2.2 MMSE criterion and DD-LMS algorithm

An equalizer is optimal in a minimum mean square error (MMSE) sense, when, given transmitted and equalized signals  $a_k$  and  $y_k$ , it minimizes the cost function:

$$J_{MSE} = E \{ |a_{k-d} - y_k|^2 \} = E \{ |e_k|^2 \}, \quad (3.18)$$

where  $d$  is an arbitrary delay (further omitted for simplicity of notation).

Let  $\mathbf{x}_k = [x_k \ x_{k-1} \ \cdots \ x_{k-N+1}]^T$  be the  $N$ -sample vector of the received signal prior to equalization, and assume a static channel (that is, after convergence  $\mathbf{w}_k = \mathbf{w}_l = \mathbf{w}$ ), so that:

$$y_k = \sum_{i=0}^{N-1} \omega_i^* x_{k-i} = \mathbf{w}^H \mathbf{x}_k. \quad (3.19)$$

Thus, from Equations (3.18-3.19),

$$\begin{aligned} J_{MSE} &= E \{ (a_k - \mathbf{w}^H \mathbf{x}_k)(a_k - \mathbf{w}^H \mathbf{x}_k)^* \}, \\ &= E \{ |a_k|^2 - a_k \mathbf{w}^H \mathbf{x}_k - \mathbf{w}^H \mathbf{x}_k a_k^* + \mathbf{w}^H \mathbf{x}_k \mathbf{x}_k^H \mathbf{w} \}, \end{aligned} \quad (3.20)$$

or, alternatively:

$$J_{MSE} = \sigma_a^2 - \mathbf{p}^H \mathbf{w} - \mathbf{w}^H \mathbf{p} + \mathbf{w}^H \mathbf{R}_x \mathbf{w}. \quad (3.21)$$

In Equation (3.21)  $\sigma_a^2$  is the transmitted signal variance,  $\mathbf{R}_x = E \{ \mathbf{x}_k \mathbf{x}_k^H \}$  is the autocorrelation matrix of the equalizer input, and  $\mathbf{p} = E \{ \mathbf{x}_k a_k^* \}$  is the cross correlation

vector between the transmitted signal and the equalizer input. Additional manipulation yields [92]:

$$J_{MSE} = \sigma_a^2 - \mathbf{p}^H \mathbf{R}_x^{-1} \mathbf{p} + (\mathbf{R}_x \mathbf{w} - \mathbf{p})^H \mathbf{R}_x^{-1} (\mathbf{R}_x \mathbf{w} - \mathbf{p}). \quad (3.22)$$

Observe that in Equation (3.22) the filter coefficient vector,  $\mathbf{w}$ , only appears in the last term, which is non-negative, since  $\mathbf{R}_x$  (and hence,  $\mathbf{R}_x^{-1}$ ), is positive semi-definite (i.e.,  $\mathbf{v}^H \mathbf{R}_x^{-1} \mathbf{v} \geq 0 \quad \forall \mathbf{v} \neq 0$ ). Therefore,  $J_{MSE}$  is minimized when  $\mathbf{R}_x \mathbf{w} - \mathbf{p} = 0$ , yielding the renowned Wiener filter, optimal in the MMSE sense [93]:

$$\mathbf{w}_{optimal} = \mathbf{R}_x^{-1} \mathbf{p}. \quad (3.23)$$

From Equation (3.21) it follows that

$$\begin{aligned} \nabla J_{MSE} &= \frac{\partial}{\partial \mathbf{w}} \{ \sigma_a^2 - \mathbf{p}^H \mathbf{w} - \mathbf{w}^H \mathbf{p} + \mathbf{w}^H \mathbf{R}_x \mathbf{w} \}, \\ &= -2\mathbf{p} + 2\mathbf{R}_x \mathbf{w}. \end{aligned} \quad (3.24)$$

Since only a limited set of data samples is available at each iteration, the stochastic gradient descent method approximates the autocorrelation matrix and the cross correlation vector of Equation (3.24) by the instant values. Namely,  $\mathbf{R}_x \approx \mathbf{x}_k \mathbf{x}_k^H$ , and  $\mathbf{p} \approx \mathbf{x}_k a_k^*$ . In this way,

$$\begin{aligned} \nabla J_{MSE} &= -2\mathbf{p} + 2\mathbf{R}_x \mathbf{w} \\ &\approx 2\mathbf{x}_k \mathbf{x}_k^H \mathbf{w}_{k-1} - 2\mathbf{x}_k a_k^* \\ &= -2\mathbf{x}_k e_k^*, \end{aligned} \quad (3.25)$$

being  $e_k = a_k - \mathbf{w}_{k-1}^H \mathbf{x}_k$  the *a priori* filtering error [92]. By substituting Equation (3.25) in Equation (3.16) we obtain the LMS algorithm:

$$\mathbf{w}_k = \mathbf{w}_{k-1} + \mu \mathbf{x}_k e_k^*, \quad (3.26)$$

where the multiplicative factor 2 was absorbed within  $\mu$ .

The LMS algorithm uses signal phase information for error computation, as seen from Equation (3.18). The pronounced phase-noise, present in high-speed optical systems, has devastating impact on the equalizer performance, requiring extra handling. One approach that eliminates phase information from error computation is to align the phase of the transmitted symbol with the phase of the received symbol after equalization:

$$e_k = a_k e^{j\phi_k} - y_k, \quad y_k = |y_k| e^{j\phi_k}, \quad (3.27)$$

resulting in the *phaseless* LMS algorithm.

Another approach is to implement phase recovery within the equalizer iterative loop, and correct the phase of the equalized symbol at the error computation [94]:

$$e_k = a_k - e^{-j\varphi_k} y_k, \quad (3.28)$$

where  $e^{-j\varphi_k}$  is the estimated via phase tracking angular back-rotation.

To convert the standard LMS to non-data-aided decision-directed algorithm, minimum distance criterion based estimates,  $\hat{a}_k$ , of the transmitted symbols are used for error calculation:

$$\hat{a}_k = \arg \min_{a \in \{A\}} |a - y_k|. \quad (3.29)$$

In Equation (3.29),  $A$  is the mQAM constellation alphabet. The drawback of the DD-LMS is that it requires some degree of equalization to make correct symbol decisions with high probability, failing as a system start-up algorithm. Therefore, it is a common practice to initialize the system with a different, more robust algorithm (e.g., conventional data-aided LMS, or CMA), and after initial convergence switch to DD-LMS.

### 3.6.2.3 Constant Modulus Algorithm

The CMA was independently proposed by Godard in 1980, and by Treichler & Agee in 1983 [95, 96]. The CMA bases on the cost function:

$$J_{CMA} = E \{ (|y_k|^p - R_p)^2 \}, \quad (3.30)$$

where  $p$  is a positive integer (commonly, 2), and  $R_p$  is a positive constant known as the  $p^{th}$ -order dispersion, defined by Godard as:

$$R_p = \frac{E \{|a_k|^{2p}\}}{E \{|a_k|^p\}}, \quad (3.31)$$

to obtain unitary gain. Nevertheless, the choice of  $R_p$  does not affect algorithm convergence properties. The rationale behind Godard's choice was that ISI never results solely in a phase rotation, and thus, would be detected by a cost function:

$$J_{MSE'} = E \{ (|y_k|^2 - |a_n|^2)^2 \} \quad (3.32)$$

(we assumed  $p = 2$ ), which is a type of a phaseless MSE criterion, also known as the amalgamated MSE [97]. The author showed that under the assumption of constellation symmetry, and data symbols being stationary and uncorrelated, Equations (3.30, 3.32)



only differ by an additive constant. Intuitively,  $J_{CMA}$  penalizes deviations from a constant modulus, as suggested by the name.

The corresponding gradient for  $p = 2$  is given by [95, 96]<sup>2</sup>:

$$\begin{aligned}
\nabla J_{CMA} &= \frac{\partial}{\partial \mathbf{w}} \left\{ E \left\{ (|y_k|^2 - R_2)^2 \right\} \right\}, \\
&= 2E \left\{ (|y_k|^2 - R_2) \frac{\partial}{\partial \mathbf{w}} (y_k y_k^*) \right\}, \\
&= 2E \left\{ (|y_k|^2 - R_2) \frac{\partial}{\partial \mathbf{w}} (\mathbf{w}^H \mathbf{x}_k \mathbf{x}_k^H \mathbf{w}) \right\}, \\
&= 2E \left\{ (|y_k|^2 - R_2) 2 \mathbf{x}_k \mathbf{x}_k^H \mathbf{w} \right\}, \\
&= 4E \left\{ (|y_k|^2 - R_2) y_k^* \mathbf{x}_k \right\}. \tag{3.33}
\end{aligned}$$

Dropping the expectancy operator for instantaneous gradient estimation, and substituting the result in Equation (3.16) yields the desired iterative algorithm:

$$\mathbf{w}_k = \mathbf{w}_{k-1} - \mu (|y_k|^2 - R_2) y_k^* \mathbf{x}_k, \tag{3.34}$$

where, again, the multiplicative factor was absorbed within the step-size.

To deal with multiple radii constellation signals, a decision-adjusted-modulus algorithm (commonly known as the radius-directed equalizer (RDE)), with much smaller residual error, was proposed in [98, 99]. Essentially, RDE is a variation of CMA, which, for an  $N$ -radii constellation, is given by:

$$\mathbf{w}_k = \mathbf{w}_{k-1} - \mu (|y_k|^2 - M_{\hat{i}}) y_k^* \mathbf{x}_k, \tag{3.35}$$

where  $M_i = r_i^2$  is the squared radius of the  $i^{\text{th}}$  constellation ring, and

$$\hat{i} = \arg \min_{i \in \{1, 2, \dots, N\}} |y_k - r_i|. \tag{3.36}$$

Thus, within each iteration the algorithm decides which of the  $N$  radii is the closest to the equalized symbol, and adjusts the adaptation criterion accordingly.

### 3.7 CARRIER RECOVERY

Carrier recovery in coherent optical systems consists of two subtasks: to compensate for the phase rotation caused by the frequency offset between the carrier and the local oscillator (deterministic component); to compensate for the phase noise, provoked by the laser sources due to their non-null linewidths (stochastic component).

---

<sup>2</sup>Refs. [95, 96] provide a different expression for  $J_{CMA}$ , namely,  $J_{CMA} = 4E \left\{ (|y_k|^2 - R_2) y_k \mathbf{x}_k^* \right\}$ . This is because the references define  $y_k$  as  $y_k = \mathbf{w}^T \mathbf{x}_k$ , rather than  $y_k = \mathbf{w}^H \mathbf{x}_k$ , as in Equation (3.19).

### 3.7.1 Frequency offset compensation

Due to the deterministic nature of the frequency offset,  $\Delta f$ , its compensation resumes in multiplying the equalized symbols  $y_k$  by the corresponding accumulated phase de-rotation [100], given by:

$$\phi_k = e^{-2\pi\Delta f T_s k} = (\phi_1)^k, \quad (3.37)$$

where  $T_s$  is the symbol period. For a QPSK signal, the incremental phase rotation is given by [100]:

$$\phi_1 = \frac{1}{4} \arg [E \{ (y_k^*)^4 (y_{k-1})^4 \}], \quad (3.38)$$

$$(3.39)$$

and can be estimated from an equalized symbol vector of length  $N$  as:

$$\hat{\phi}_1 = \frac{1}{4} \arg \left[ \frac{1}{N} \sum_{k=1}^N (y_k^*)^4 (y_{k-1})^4 \right]. \quad (3.40)$$

$$(3.41)$$

Here, the raising to the 4<sup>th</sup> power eliminates symbol dependency, bringing all symbols to the same phase reference of  $\pi$  rad.

For higher order modulation formats, the algorithm can be seamlessly refined for estimation accuracy. For example, for a 3-radii 16QAM signal, the estimates may include only the inner and outer radii symbols, whose 4<sup>th</sup> power falls onto the  $\pi$  rad phase reference, making the corresponding amplitude and temporal adjustments.

Another method estimates  $\Delta f$  in the frequency domain, as [101]:

$$\widehat{\Delta f} = \frac{1}{4} \max_f [|\text{FFT}(\mathbf{y}^{\circ 4})|], \quad (3.42)$$

where  $\mathbf{y} = [y_1, y_2, \dots, y_N]$  is a vector of length  $N$  of the equalized symbols, and  $(\cdot)^{\circ x}$  denotes element-by-element raising to the  $x^{\text{th}}$  power. Here, the stable tone found via the Fourier transform corresponds to the quadrupled carrier-LO beating frequency.

### 3.7.2 Phase noise estimation

Phase noise is usually modeled as a discrete-time Wiener process, so that the phase of the  $k^{\text{th}}$  symbol is [102]:

$$\theta_k = \sum_{i=-\infty}^k \delta_i, \quad (3.43)$$

or, in recurrence equation form [100]:

$$\theta_k = \theta_{k-1} + \delta_k, \quad (3.44)$$

In Equations (3.43-3.44),  $\delta$  is a random Gaussian variable with zero mean and variance  $\sigma_\delta^2 = 2\pi \Delta\nu T_s$ , being  $\Delta\nu$  the sum of the carrier and the LO linewidths.

Figure 3.9(a) shows the block diagram of a simple hardware efficient scheme for phase error compensation, proposed in [102], and commonly known as the blind phase search (BPS) algorithm [103]. The  $k^{\text{th}}$  equalized symbol,  $y_k$ , is fed in parallel to  $B$  test blocks, whose internal architecture is shown in Figure 3.9(b). Each block rotates  $y_k$  by  $\phi_b$ , where:

$$\phi_b = \frac{b \pi}{B 2}, \quad b \in \{0, 1, \dots, B-1\}. \quad (3.45)$$

or alternatively,

$$\phi_b = \frac{b \pi}{B 2} - \frac{\pi}{4}, \quad b \in \{0, 1, \dots, B-1\}. \quad (3.46)$$

Thus, phases  $\phi_b$  are equally distributed within a phase range of  $\pi/2$ , either from 0 to  $\pi/2$ , or from  $-\pi/4$  to  $\pi/4$ , and  $B$  defines the granularity of the tested values.

After rotation, each block estimates the transmitted symbol using minimum-distance-criterion slicer, yielding  $B$  estimates,  $\{\hat{a}_{k,0}, \hat{a}_{k,1}, \dots, \hat{a}_{k,B-1}\}$ , for which squared distances of the rotated symbols are computed:

$$|d_{k,b}|^2 = |\hat{a}_{k,b} - y_k e^{j\phi_b}|^2. \quad (3.47)$$

To filter out high-frequency noise components, the square errors in each block are integrated (or averaged) over an  $N$ -valued window, and the smallest element  $e_{k,i}$  is extracted from the resulting error vector,  $\{e_{k,0}, e_{k,1}, \dots, e_{k,B-1}\}$ . The phase estimation, therefore, is given by:

$$\hat{\theta}_k = PU\{(\phi_i)_k\} \mid e_{k,i} \leq e_{k,j}, \quad \forall j \in \{0, 1, \dots, B-1\}, \quad j \neq i, \quad (3.48)$$

where  $PU$  denotes the phase unwrapping operation to ensure phase ranging from  $-\infty$  to  $+\infty$  [100]:

$$PU\{(\phi_i)_k\} = \theta_k + \left( \left\lfloor \frac{1}{2} + \frac{(\phi_i)_{k-1} - (\phi_i)_k}{\pi/2} \right\rfloor \right) \frac{\pi}{2}. \quad (3.49)$$

Accordingly, the  $k^{\text{th}}$  transmitted symbol is estimated as:

$$\hat{a}_k = \hat{a}_{k,i} \mid e_{k,i} < e_{k,j}, \quad \forall j \in \{0, 1, \dots, B-1\}, \quad j \neq i. \quad (3.50)$$

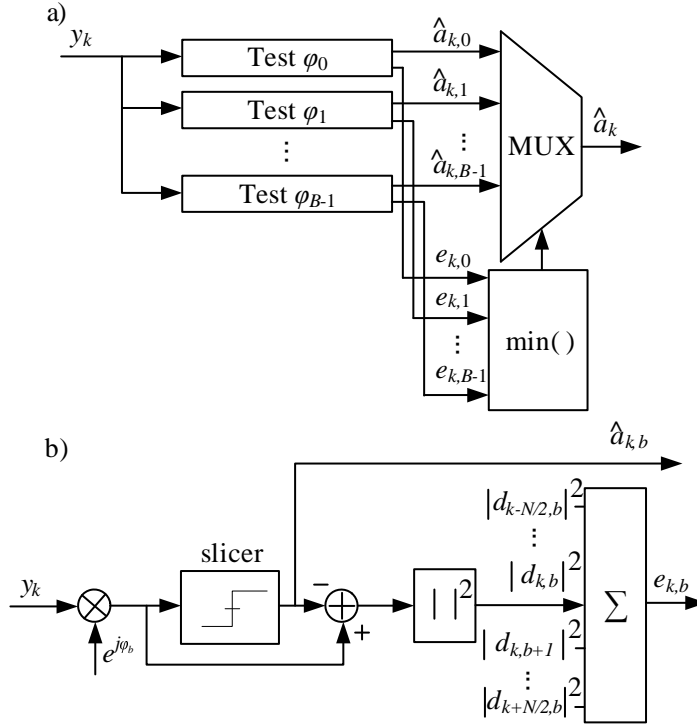


Figure 3.9: Blind phase search algorithm. (a) Block diagram; (b) Test block internal architecture.

### 3.8 NONLINEAR IMPAIRMENTS COMPENSATION

Digital domain nonlinear compensation is a “hot” research topic in optical communications nowadays. This is because in the current state-of-the-art coherent technology, with linear impairments being compensated for with minimum penalty, nonlinearities constitute the main limiting factor, restricting optical power and reducing the signal-to-noise ratio. Additionally, nonlinear compensation is extremely important in the context of the, so called, unrepeated systems, deployed over hostile, or difficult access areas, as, e.g., in island-to-island and Amazon rainforest communities connection. Those systems do not rely on active in-line components (namely, optical amplifiers), and thus, must operate at high launch powers, increasing the effect of nonlinear impairments.

So far, to the best of our knowledge, no commercial device implements nonlinear compensation, because it is still too challenging for the current-state technology from the hardware complexity standpoint. Much work, however, is done to reduce complexity, in order to turn nonlinear compensation by DSP feasible (e.g., [46, 104, 105]). Therefore, taking into account the advances in CMOS fabrication technology (being 14 nm the current state-of-the art), with constant increase in transistor density and power consumption reduction, it is likely that first nonlinear compensation chip prototypes

appear in the near future. In fact, some recent works already assess implementation complexity at the netlist and physical synthesis level [106].

### 3.8.1 Digital backpropagation

Nonlinearities are compensated for in digital domain via the digital backpropagation algorithm (DBP), first proposed in [107]. The key idea behind DBP is to solve the nonlinear Schrödinger equation in the inverse direction, so to reconstruct the original signal. The inverse CNLSE can be obtained from Equation (2.23) as:

$$\begin{aligned} \frac{\partial \mathbf{A}}{\partial(-z)} = & \frac{\alpha}{2} \mathbf{A} + \Theta(z) \left[ \frac{\Delta\beta_0}{2} \mathbf{A} - \frac{\Delta\beta_1}{2} \frac{\partial \mathbf{A}}{\partial t} \right] + \frac{j\beta_2}{2} \frac{\partial^2 \mathbf{A}}{\partial t^2} \\ & - j\gamma \left[ |\mathbf{A}|^2 \mathbf{A} - \frac{1}{3} (\mathbf{A}^H \sigma_3 \mathbf{A}) \sigma_3 \mathbf{A} \right]. \end{aligned} \quad (3.51)$$

Equation (3.51) can be seen as propagation in the opposite direction over a virtual fiber with parameters  $-\alpha$ ,  $-\gamma$ , and  $-\beta$ . Due to its stochastic nature, evolution of the PMD-related terms in Equation (3.51) ( $\Delta\beta_0$ - and  $\Delta\beta_1$ -dependent) cannot be reconstructed, and so, those terms are dropped. As shown earlier, PMD contribution is separately compensated for by the dynamic equalizer. This approximation can be safely applied when DGD is a small fraction of symbol period [59]. For the same reason, the polarization coupling nonlinear term,  $\frac{1}{3} (\mathbf{A}^H \sigma_3 \mathbf{A}) \sigma_3 \mathbf{A}$ , is averaged over all possible state of polarization to  $\frac{1}{9} |\mathbf{A}|^2 \mathbf{A}$ , yielding the Manakov equation for backpropagation:

$$\frac{\partial \mathbf{A}}{\partial(-z)} = \frac{\alpha}{2} \mathbf{A} + j \frac{\beta_2}{2} \frac{\partial^2 \mathbf{A}}{\partial t^2} - j \frac{8}{9} \gamma |\mathbf{A}|^2 \mathbf{A}. \quad (3.52)$$

The last approximation is valid for the condition:  $L_c \ll L_{\text{NL}}$ , which is typical for standard fibers. Here,  $L_c$  is the correlation length, defined as the length over which two polarization components remain correlated, and  $L_{\text{NL}} = (\gamma P_0)^{-1}$  is the nonlinear length that corresponds to the length that yields a 1-rad nonlinear phase shift at maximum signal power [1].

Two observations should be made regarding DBP. Firstly in order to implement DBP, the receive-side requires the knowledge of power and dispersion maps of the optical link. This condition somewhat defies the idea of adaptive transceiver that autonomously estimates the required parameters, however, this information can be provided by the network control plane. Secondly, in WDM systems, DBP is only able

to compensate for the nonlinearities induced by the signals dropped at a particular node, because it lacks the optical field information of the remaining signals.

### 3.8.2 Split-step Fourier method

Since Equation (3.52) has no analytical solution, it is solved numerically in the digital domain. A reference method, used by most commercial simulation tools due to its high reliability, is the split-step Fourier method (SSFM) [56]. The key idea behind the SSFM is that, for a sufficiently small spacial step,  $\Delta z$ , linear and nonlinear terms of Equation (3.52) can, with high accuracy, be treated separately. Thus, linear and nonlinear operators are defined as [63]:

$$\hat{\mathbf{D}} = \frac{1}{2}\alpha + j\frac{\beta_2}{2}\frac{\partial^2}{\partial t^2}, \quad (3.53)$$

$$\hat{\mathbf{N}} = -j\frac{8}{9}\gamma|\mathbf{A}|^2, \quad (3.54)$$

so that:

$$\frac{\partial \mathbf{A}}{\partial(-z)} = (\hat{\mathbf{D}} + \hat{\mathbf{N}})\mathbf{A}. \quad (3.55)$$

These operators are applied successively, interleaved with one another, for each  $\Delta z$ . For better efficiency, linear step is applied in the frequency-domain, while nonlinear step, in time-domain. A pseudo-code of a basic form of SSFM-based DBP is shown in Algorithm 1.

From inspecting Algorithm 1 it becomes clear why SSFM is so computationally complex. It requires FFT and IFFT operation for each step  $\Delta z$ , which is extremely cumbersome to be computed in real-time at elevated transmission rates. Some techniques have been developed to reduce complexity with acceptable penalty. Thus, a step-size  $\Delta z$  may be adapted, so that it is much longer for low power values, where linear effects are predominant. In this case, it is common to define a maximum non-linear phase rotation (practical values about 1-5 mrad) as a criterion for the step-size feasibility [67]. Another technique involves spatial power averaging, so that a single step-per-span can be applied. The power value is taken as the one corresponding to effective length of the span [108].

---

**Algorithm 1** Split-step Fourier method for DBP

---

1: **Define:**

2:  $IN_{x/y}$  – Input X/Y-pol signals

3:  $OUT_{x/y}$  – Output X/Y-pol signals

4:  $\omega$  – Vector of angular frequencies

5:  $LinOp = \exp\left(\frac{\alpha}{2} - j\frac{\beta_2}{2}\omega^2\right)$  – Frequency-domain linear operator

---

**begin program**

6:  $IN\_FD_{x/y} = FFT(IN_{x/y})$      $\triangleright$  Frequency domain transformation

7:  $OUT\_NL_{x/y} = IN_{x/y}$      $\triangleright$  Initialize loop variable  $OUT\_NL$  as the input signal

8: **for** ( $SPAN = 1$  **until**  $SPAN =$  Number of spans;  $SPAN++$ ) **do**

9:     $LENGTH = 0$      $\triangleright$  Propagation length initialization

10:    **while** ( $LENGTH \neq$  Span length) **do**

11:      $LENGTH = LENGTH + \Delta z$

---

$\triangleright$  Linear step:

12:     $OUT\_NL_{x/y} = OUT\_NL_{x/y} \cdot \exp\left(\frac{\alpha}{2}z\right)$      $\triangleright$  Applying power increase

13:     $OUT\_NL\_FD_{x/y} = FFT(OUT\_NL_{x/y})$      $\triangleright$  Frequency domain transformation

14:     $OUT\_LIN_{x/y} = IFFT(LinOp \cdot OUT\_NL\_FD_{x/y})$      $\triangleright$  Applying linear operator  
& time-domain transformation

---

$\triangleright$  Nonlinear step:

15:     $Power = \frac{8}{9} (|OUT\_LIN_x|^2 + |OUT\_LIN_y|^2)$      $\triangleright$  Signal power estimation,  
considering Manakov PMD approximation

16:     $OUT\_NL_{x/y} = OUT\_LIN_{x/y} \cdot \exp(-j\gamma \cdot Power \cdot \Delta z)$      $\triangleright$  Nonlinear phase  
de-rotation.

---

17:    **end while**

18:    **if** ( $SPAN \neq$  Number of spans) **then**

19:      $OUT\_NL_{x/y} = OUT\_NL_{x/y} \cdot \exp\left(-\frac{\alpha}{2} \cdot \text{Span length}\right)$      $\triangleright$  Compensate for the  
amplification stage

20:    **else**

21:      $OUT_{x/y} = OUT\_NL_{x/y}$

22:    **end if**

23: **end for**

**end program**

---

## Chapter 4 DIGITAL-DOMAIN CD COMPENSATION AND COMPLEXITY ANALYSIS

Different trade-offs involved in the static equalizer design impact computational complexity and, thus, have immediate effect on the efficiency of the rate switching method for conventional Tx systems, which constitutes one of the two main contributions of this thesis. In this chapter, therefore, we present different equalizer design approaches and computational complexity analysis. We further infer, by computer simulations, practical values of selected design parameters, investigating NRZ, RZ, and Nyquist-shaped signals, and assess the effective complexity gain that can be achieved with the symbol-repetition-based rate switching.

### 4.1 CD EQUALIZER DESIGN

As stated in Section 2.2.1.1, chromatic dispersion is a polarization-independent, linear, time-invariant impairment. Therefore, it is commonly compensated by specifically-designed static equalizers. Sufficiently long MSE criterion-based dynamic equalizers may, in principle, be employed; however, this solution increases computational complexity. This is because polarization-dependent and polarization-independent impairments cannot be separated by the MSE criterion, so that information of both polarizations must be used for equalization, requiring a “butterfly” equalizer structure that effectively doubles the number of filter taps. Moreover, adaptive tap weight computation also aggregates unnecessary complexity.

#### 4.1.1 Equalizer length estimation

The CD quadratic phase response is translated into temporal spreading of the pulse energy. Therefore, CD equalizer impulse response length should be matched to the fiber pulse broadening due to CD. The temporal broadening of a pulse with spectral width



$\Delta\omega$  is given by [1]:

$$\Delta T = z \frac{d^2\beta}{d\omega^2} \Delta\omega = z|\beta_2| \Delta\omega = |D|z \frac{\lambda^2}{c} \Delta f = |D|z \frac{c}{f_c^2} \Delta f, \quad (4.1)$$

where we used the fiber dispersion parameter,  $D = -\beta_2(2\pi c)/\lambda^2$ . In Equation (4.1),  $z$  is the fiber length,  $\lambda$  is the optical carrier wavelength,  $c$  is the speed of light,  $f_c$  is the carrier frequency, and  $\Delta f$  is the pulse spectral width in Hz. The rightmost form of Equation (4.1) frequently appears in the literature, e.g., in [109–111]. The equivalent finite impulse response (FIR) filter length is related to the temporal pulse broadening via the sampling time,  $T_{Sa}$ :

$$N_{CD} = \left\lceil \frac{\Delta T}{T_{Sa}} \right\rceil, \quad (4.2)$$

where  $\lceil x \rceil$  denotes the nearest integer larger than  $x$ .

In [112], Xu et al. proposed another expression for the FIR impulse response, assuming Gaussian pulse approximation [1]:

$$N_{CD} = 2 \times \left\lceil \frac{1}{\pi c T_{Sa}^2} \sqrt{\pi^2 c^2 T_{Sa}^4 + 4\lambda^4 D^2 z^2} \right\rceil + 1. \quad (4.3)$$

Alternatively, Ip and Kahn, in [72], proposed an empirical relationship:

$$N_{CD} \approx 6.67|\beta_2|zR_s^2(M/K), \quad (4.4)$$

where  $R_s$  is the signal symbol rate, and  $M/K$  is the oversampling rate of the fractionally-spaced equalizer. Here, however, the authors were targeting the residual CD, assuming dispersion-managed links.

Figure 4.1 shows the filter tap weights of an MSE-criterion-based fractionally-spaced dynamic equalizer (oversampling rate = 2) after convergence for three different pulse formats: non-return to zero (NRZ); return to zero (RZ) with 50% duty cycle; and Nyquist, with roll-off factor 0.2. We used a 28 GBd QPSK signal, corrupted by CD of 20 ns/nm, assuming a 3<sup>rd</sup> degree model, in otherwise ideal conditions. Additionally, the signal was filtered by a 50-GHz (passband) 4<sup>th</sup> order Gaussian filter, and a 19-GHz (baseband) 2<sup>nd</sup> order Gaussian filter, to emulate ROADM filtering and receiver (ADC, photodetector and TIA) bandwidth limitations, respectively. Clearly, the length of the optimal impulse response depends on the signal pulse shape. As expected, Nyquist-shaped signals, having the smallest spectral content, yield the shortest impulse response. Nevertheless, the quasi-rectangular energy spread of the Nyquist-case filter indicates a likelihood of more severe signal degradation if under-dimensioned than, e.g., in the case of RZ pulses. In the following sections we investigate these assumptions.

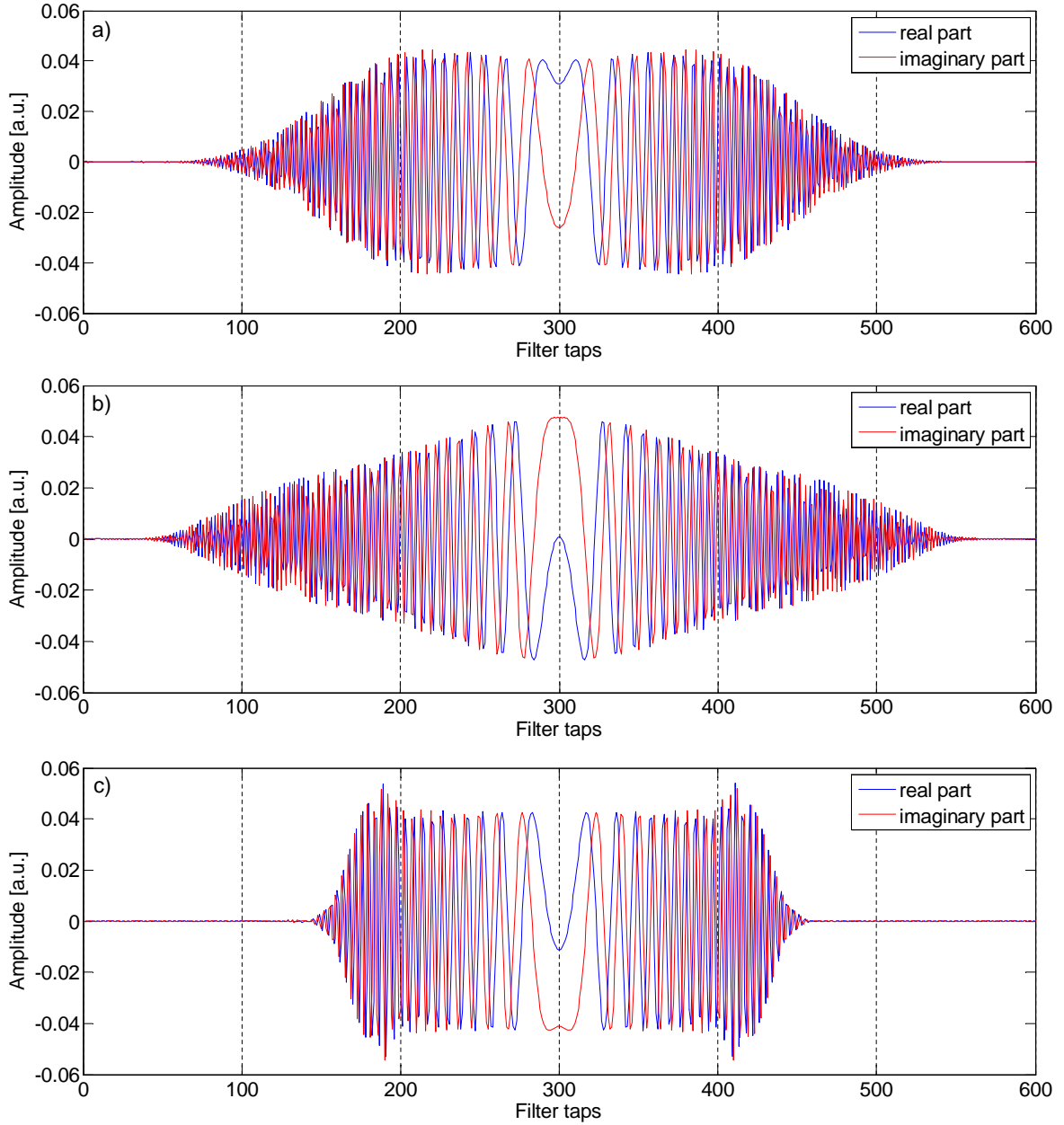


Figure 4.1: Tap weights of an MSE-based dynamic equalizer for different pulse shapes: (a) NRZ; (b) RZ with 50% duty cycle; (c) Nyquist with roll-off factor = 0.2.

#### 4.1.2 Time-domain equalizer design

CD compensating filter may be designed either in time-domain (TD), or in frequency-domain (FD). The time-domain design was proposed in [35]. From Equation (2.7), CD transfer function is:

$$G(z, \omega) = \exp\left(j\frac{\beta_2 z}{2}\omega^2\right) = \exp\left(-j\frac{Dz\lambda^2}{4\pi c}\omega^2\right). \quad (4.5)$$

This transfer function can be transformed into the time-domain via the inverse Fourier transform using the identity [63]:

$$\int_{-\infty}^{\infty} \exp(-ax^2 - bx)dx = \sqrt{\frac{\pi}{a}} \exp\left(\frac{b^2}{4a}\right), \quad (4.6)$$

yielding the impulse response of the dispersive fiber:

$$g(z, t) = \sqrt{\frac{c}{jD\lambda^2z}} \exp\left(j\frac{\pi c}{D\lambda^2z}t^2\right). \quad (4.7)$$

The impulse response of the CD compensating (continuous time) filter,  $g_c(z, t)$  is, therefore:

$$g_c(z, t) = \frac{1}{g(z, t)} = \sqrt{\frac{j c}{D\lambda^2z}} \exp\left(-j\frac{\pi c}{D\lambda^2z}t^2\right). \quad (4.8)$$

Finally, the  $k^{\text{th}}$  digital filter tap weight can be computed from Equation (4.8) as [35]:

$$a_k = \sqrt{\frac{j c T_{Sa}^2}{D\lambda^2z}} \exp\left(-j\frac{\pi c}{D\lambda^2z}T_{Sa}^2k^2\right). \quad (4.9)$$

Observe that Equation (4.8) was derived directly from the fiber CD transfer function of Equation (4.5), which is, essentially, an all-pass filter. Therefore, for a finite sampling rate  $1/T_{Sa}$ , spectral content above the Nyquist frequency will be aliased into the signal band, degrading the signal. Figure 4.2(a) shows the impulse response of a filter, designed using Equation (4.9). Real and imaginary parts of the equalizer coefficients form a periodically repeating frequency chirp pattern, and sum to a constant amplitude throughout the filter length, unlike Figures 4.1(a-c). (Here, the accumulated CD value was reduced to 3.4 ns/nm instead of 20 ns/nm for better visualization.) To combat this effect, the impulse response must be truncated to a finite duration [35]. For a signal, sampled at  $1/T_{Sa}$ , the Nyquist frequency,  $f_n$ , is given by  $f_n = 1/(2T_{Sa})$ , which, in angular representation, corresponds to  $\omega_n = 2\pi f_n = \pi/T_{Sa}$ . On the other hand, the angular frequency is the change in the angle  $\phi(t)$  of the (continuous time) filter impulse response of Equation (4.8):

$$\omega = \frac{\partial\phi(t)}{\partial t} = \frac{2\pi c}{D\lambda^2z}t, \text{ where } \phi(t) = \frac{\pi c}{D\lambda^2z}t^2. \quad (4.10)$$

Restricting the angular frequency to  $|\omega| \leq \omega_n$ , we obtain:

$$-\frac{|D|\lambda^2z}{2cT_{Sa}} \leq t \leq \frac{|D|\lambda^2z}{2cT_{Sa}}. \quad (4.11)$$

Thus, the upper limit on equalizer taps is:

$$N_{\max} \leq 2 \times \left\lfloor \frac{|D|\lambda^2z}{2cT_{Sa}^2} \right\rfloor + 1, \quad (4.12)$$

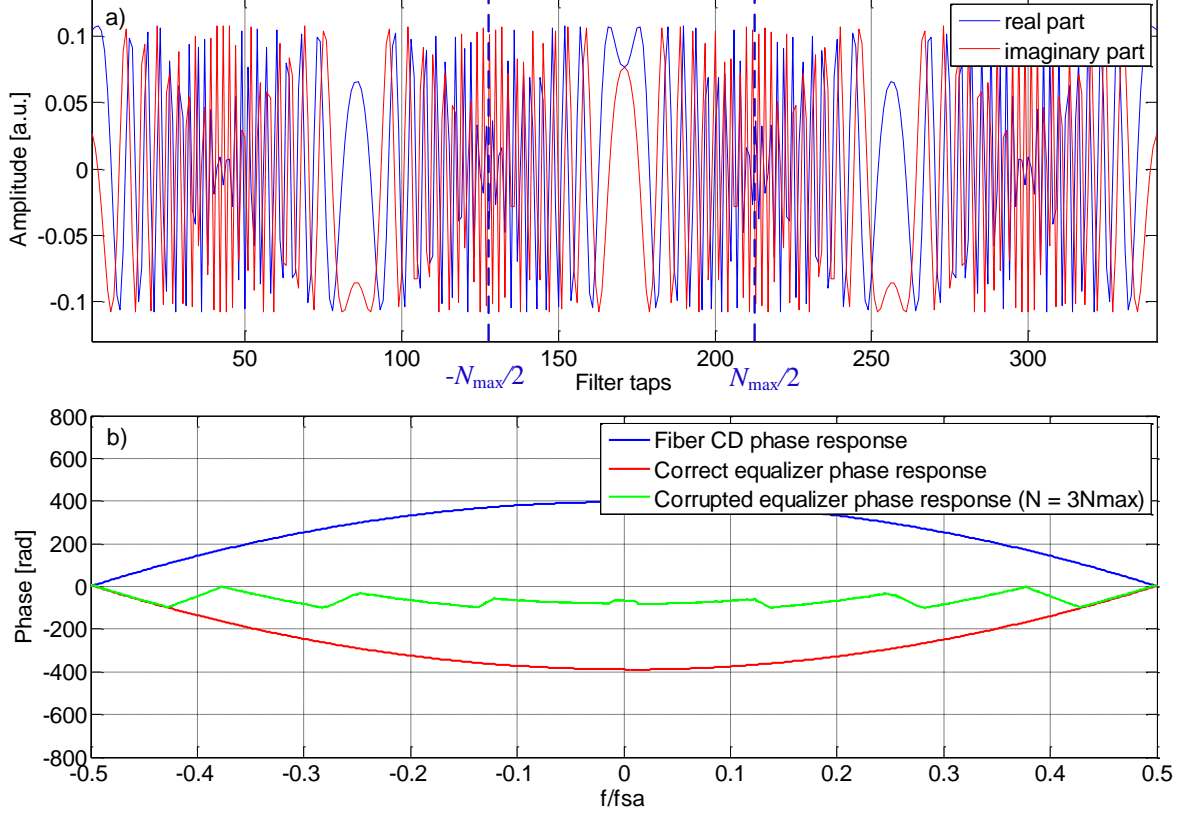


Figure 4.2: (a) Tap weights of a TD CD equalizer, designed using Equation (4.9); (b) Phase response for  $N_{\text{CD}} = N_{\text{max}}$  and  $N_{\text{CD}} = 3N_{\text{max}}$ .

and  $k$  in Equation (4.9) is spread over the interval:  $-\lfloor N_{\text{max}}/2 \rfloor \leq k \leq \lfloor N_{\text{max}}/2 \rfloor$ . This truncation window is also shown in Figure 4.2(a). Equation (4.12) ensures odd number of taps for design convenience. Note, that the existence of an upper bound for  $N$  is a result of a particular form of filter design in [35]. Figure 4.2(b) shows the impact of ill-truncation on the equalizer phase response. The convex and the concave parabolae represent the fiber and the equalizer phase responses for  $N_{\text{CD}} = N_{\text{max}}$ , canceling one another, while the green line shows the corrupted equalizer phase response, when  $N_{\text{CD}} = 3N_{\text{max}}$ .

The encountered upper bound,  $N_{\text{max}}$  can be considerably reduced. For comparison, under the above described simulation conditions with accumulated CD = 20 ns/nm, the upper bound, calculated using Equation (4.12), is  $N_{\text{max}} = 503$ ; while for an NRZ signal, considering  $\Delta f \approx 0.7 \times 2R_s$ , Equations (4.1-4.2) yield:  $N_{\text{CD}} = 343$ . That is  $N_{\text{CD}} \approx 0.68N_{\text{max}}$ , which agrees with the numerical investigation in [35], stating that in practice  $N_{\text{CD}}$  may be reduced down to  $0.6N_{\text{max}}$  with only a minor performance penalty.

Figure 4.3 shows a TD CD equalizer amplitude and group delay response for 50 km (Figures 4.3(a,b)), 500 km (Figures 4.3(c,d)) and 1500 km (Figures 4.3(e,f)) optical links. The corresponding equalizer lengths are 21, 213, and 641 taps, respectively. Note

that, for low accumulated CD values, a small number of taps results in heavy ripple, degrading filter performance. This ripple is reduced with filter length, being “pushed” towards the edge frequencies, approximating the ideal response. Ripple characteristics of the TD equalizer can be further reduced by additional windowing [35].

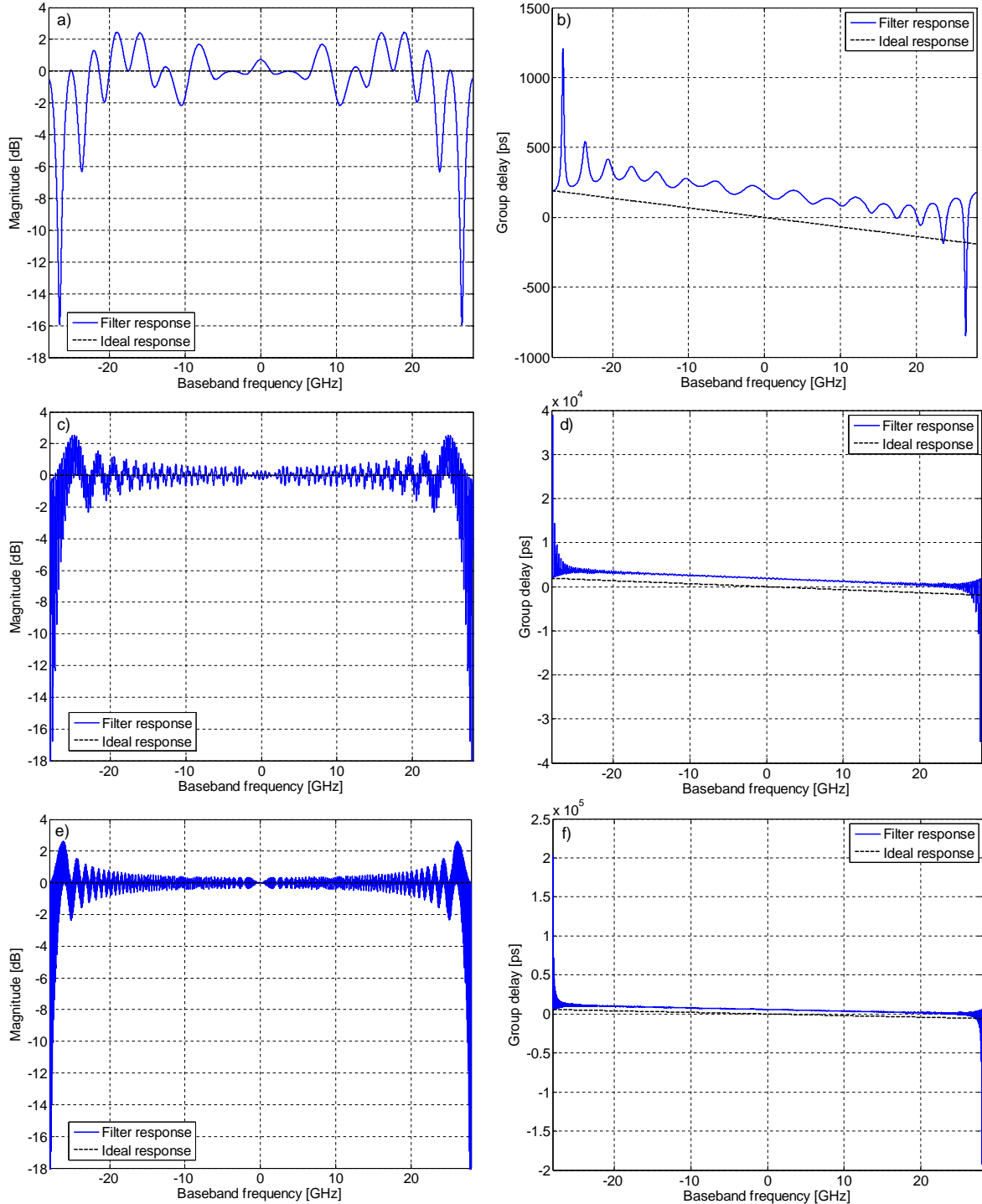


Figure 4.3: Time-domain CD equalizer magnitude (left column) and group delay (right column) response for: (a,b) 50-km propagation; (c,d) 500-km propagation; (e,f) 1500-km propagation.

### 4.1.3 Frequency-domain equalizer design

One way to obtain a frequency-domain CD equalizer is to apply a discrete Fourier transform (DFT) on the time-domain filter, designed using Equation (4.9). In principle, any size of FD equalizer may be employed, provided that  $N_{\text{FD}} \geq N_{\text{CD}}$ . It is accomplished by appending TD filter coefficients with zeros before applying DFT. Complexity implications of the choice for the equalizer size are discussed in Section 4.2. Note, however, that in this case, regardless of its size, the FD equalizer maintains the same ripple characteristics as its TD counterpart (see Figure 4.3).

Alternatively, the CD equalizer may be designed directly in the frequency domain, as described in [111]. The FD equalizer coefficients are directly computed from the CD transfer function of Equation (4.5), over the frequency interval  $[-f_n, f_n]$ . Specifically, filter coefficients are computed as:

$$a_k = \exp\left(j\frac{Dz\lambda^2\pi}{c}f_k^2\right), \quad (4.13)$$

where

$$f_k = -f_n + \frac{k}{N_{\text{FD}}}, \quad k \in \{0, 1, \dots, N_{\text{FD}} - 1\}. \quad (4.14)$$

Unlike in the previous case, the essentially ideal equalizer characteristics (amplitude and group delay response) do not depend on the accumulated CD.

## 4.2 CD COMPENSATION COMPLEXITY ANALYSIS

To assess computational complexity we use the number of required multiplications per transmitted bit as the figure of merit, since multiplication is the dominant power consuming hardware-implemented operation, in comparison with addition and storage [113]. It is well known that thanks to the fast Fourier transform (FFT) algorithm, signal convolution with a sufficiently long FIR filter is more efficiently implemented in the frequency domain, using a data overlapping method (either overlap-&-save, or overlap-&-add) [50]. Since (TD-equivalent) CD compensation equalizer size in high-speed long-haul links may vary from several hundred to thousands taps, it became a recent consensus that CD be compensated in the frequency domain.

Frequency-domain equalization cycle involves the following operations:

1. Computation of the FFT of the new-coming data block.
2. Term-by-term multiplication of the result in step 1 with the FD equalizer coefficients.
3. Computation of the inverse FFT (IFFT) of the result.

The number of (non-trivial) real multiplications,  $M_R$ , required for the computation of an FFT (IFFT) of size  $N_{\text{FFT}}$  depends on the algorithm, optimization degree, and hardware implementation. Here, we assume a radix-2 Cooley-Tukey algorithm. Without loss of generality, we also assume that each complex multiplication is implemented by three real ones.<sup>1</sup> Under these conditions,  $M_R$  is given by [114]:

$$M_R = \frac{3}{2}N_{\text{FFT}}(-3 + \log_2 N_{\text{FFT}}) + 6, \quad (4.15)$$

provided that  $N_{\text{FFT}} = 2^k$ ,  $k \in \mathbb{N}$ . The number of real multiplications per filtering cycle,  $M_{\text{cyc}}$ , is given by:

$$M_{\text{cyc}} = p(2M_R + 3N_{\text{FFT}}), \quad (4.16)$$

where  $p$  is the number of polarizations. In Equation (4.16)  $M_R$  is multiplied by 2 to account for both the FFT and the IFFT, and  $3N_{\text{FFT}}$  is the number of real multiplications in step 2 of the equalization cycle.

From Section 4.1.3,  $N_{\text{FFT}}$  and  $N_{\text{FD}}$  are identical, and the CD-induced pulse broadening, normalized by the sampling period,  $N_{\text{CD}}$ , represents the minimum data overlap, required for CD-free equalization. Therefore, the number of samples obtained in each filtering cycle (for a single polarization) is  $Sa_{\text{cyc}} = N_{\text{FD}} - N_{\text{CD}} + 1$ . Note that for  $N_{\text{FD}} = N_{\text{CD}}$ ,  $Sa_{\text{cyc}} = 1$ , as in TD equalization. The number of bits resulting in one filtering cycle is given by:

$$b_{\text{cyc}} = \frac{pSa_{\text{cyc}}}{\kappa} \log_2 m, \quad (4.17)$$

where  $\kappa$  is the oversampling factor, and  $m$  is the cardinality of the modulation alphabet. Finally, the number of multiplications per transmitted bit,  $M_b$ , is computed as:

$$\begin{aligned} M_b &= M_{\text{cyc}}/b_{\text{cyc}}, \\ &= \frac{\kappa}{Sa_{\text{cyc}} \log_2 m} (2M_R + 3N_{\text{FFT}}), \\ &= \frac{\kappa}{(N_{\text{FFT}} - N_{\text{CD}} + 1) \log_2 m} (2M_R + 3N_{\text{FFT}}). \end{aligned} \quad (4.18)$$

---

<sup>1</sup>Here,  $e + jd = (a + jb) \cdot (c + jd)$  is computed as  $e = (a - b)d + a(c - d)$ , and  $f = (a - b)d + b(c + d)$ , requiring three real multiplications and five real additions [114].

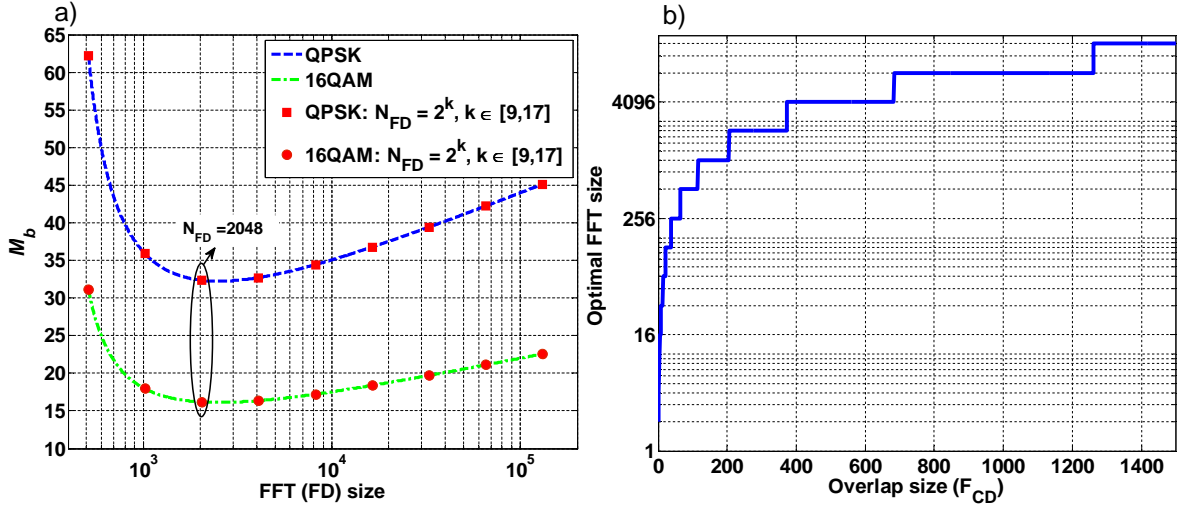


Figure 4.4: a) FFT size optimization for  $N_{CD} = 340$ ; (b) Optimal FFT size vs. overlap.

The  $M_b$  can be further minimized with respect to  $N_{FFT}$ , significantly reducing the complexity [115]. Figure 4.4(a) illustrates this reduction, showing the number of multiplications per transmitted bit for a 340 tap CD compensation filter for QPSK and 16QAM polarization multiplexed signals, as a function of the FFT size. Additionally, Figure 4.4(b) shows the optimum FFT size values for different overlaps, corresponding to a wide range of practical accumulated CD values.

### 4.3 COMPLEXITY GAIN OF THE SYMBOL-REPETITION-BASED RATE SWITCHING

As seen from Section 4.1.1, computing the exact CD equalizer length (or alternatively, the overlap size for FD equalization) is not trivial; in addition to the accumulated CD and the sampling rate, it is considerably affected by the pulse format. In the following, we conduct a computer simulation to infer practical values of the overlap length for frequency-domain CD compensation for the commonly used in optical communications pulse shapes, namely, NRZ, RZ with 50% duty cycle, and Nyquist raised cosine (RC) pulses. Additionally, by varying the symbol rate, we obtain the complexity gain due to CD compensation that can be provided by the symbol-repetition-based rate switching, described in Chapter 5.



### 4.3.1 Simulation setup

Although the number of per-bit operations can be minimized with respect to  $N_{\text{FFT}}$ , physical design constraints turn variable-size FFT challenging to implement; and a fixed-size FFT is a common choice. Therefore, based on practical experience, we chose  $N_{\text{FFT}} = 8192$  for the subsequent simulations.

Table 4.1: Simulation parameters for CD compensation complexity analysis.

Modulation format	QPSK
Pulse format	NRZ, roll-off = 0.2; RZ, duty cycle = 50%; Nyquist (RC), roll-off = 0.15, Pulse-shaping filter length = 512
Simulation rates	Symbol rate = 28/14/7 GBd Samples per symbol = 32
Phase noise	Carrier linewidth = 100 kHz LO linewidth = 100 kHz
Fiber parameters	$D = 16.75$ ps/(nm.km); Dispersion slope = 0.0656 ps/(nm <sup>2</sup> .km)
CD equalizer	$N_{\text{FFT}} = 8192$
Dynamic equalizer algorithm	CMA, Number of taps = 7 step-size = 0.001
AWGN noise	OSNR = 14 dB

The Matlab<sup>®</sup>-built simulation setup, depicted in Figure 4.5 is as follows. Pseudo-random binary strings are mapped onto the digital alphabet. A pulse shaping procedure creates the complex envelopes for X-pol. and Y-pol. signal tributaries, representing each symbol by 32 samples. Three symbol rates, 28, 14, and 7 GBd are investigated. After adding the carrier phase noise, the signal is filtered by a 50-GHz 4<sup>th</sup>-order Gaussian filter to emulate channel optical filtering. Additive white Gaussian noise (AWGN) is added to the signal to yield 14 dB OSNR. Accumulated CD is added using the expansion of the propagation constant,  $\beta$ , in Taylor series up to 3<sup>rd</sup>-order (that is, including dispersion slope [1]), and X-pol. and Y-pol. signals are mixed at a 45° polarization rotation angle. At the receiver, local oscillator (LO) phase noise is added, and the signal is filtered by a 19-GHz low-pass 2<sup>nd</sup>-order Gaussian filter that emulates the receiver photo-detector and transimpedance amplifier bandwidths. For 14 and 7 GBd signals, the filter bandwidth is reduced to 9.5, and 4.75 GHz, respectively, to emulate

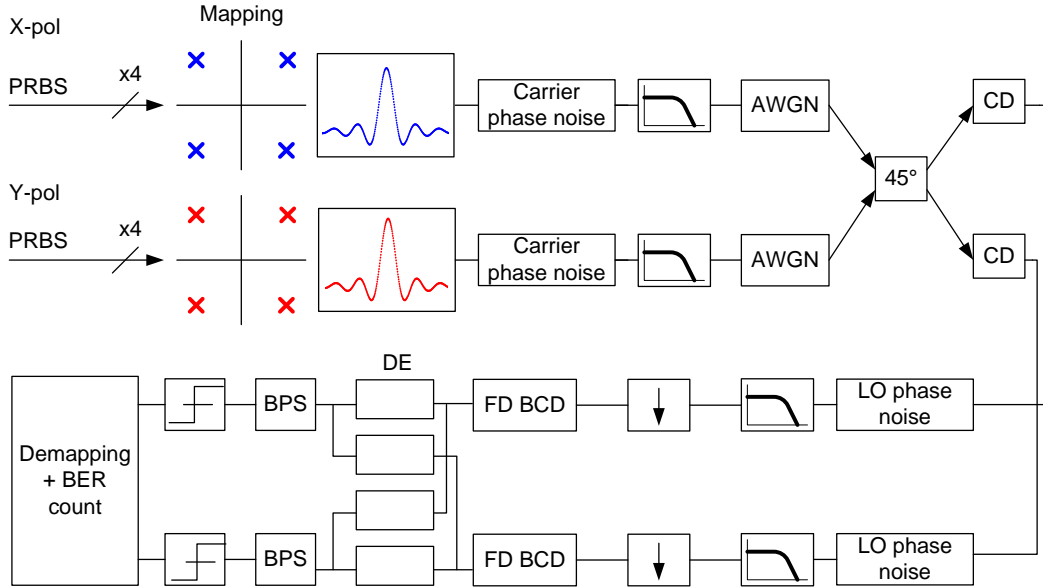


Figure 4.5: Simulation setup for overlap impact investigation.

anti-aliasing digital filtering of the repetition-based rate switching (see Section 5.1 for details), and filter out the out-of-band noise.

The receiver signal processing consists of resampling to 2 samples per symbol ( $\kappa = 2$ ) using native Matlab interpolation; frequency-domain CD compensation (FFT size 8192); adaptive equalization by the constant modulus algorithm; and blind phase search. After symbol decision, differential decoding is applied. Table 4.1 summarizes the simulation parameters.

### 4.3.2 Results and discussion

Figures 4.6(a-c) show the BER, computed over  $10^6$  bits, as a function of the overlap size for NRZ, RZ, and RC-shaped 28 Gb/s PM-QPSK signals, respectively. This rate is typically employed in 100G systems with hard decision FEC. The accumulated CD values vary from 0 to 90 ns/nm in steps of 10 ns/nm, roughly corresponding to transmission distances up to 5,300 km, assuming a standard single-mode fiber with dispersion parameters as in Table 4.1. The obtained overlap values may be used as guidelines for practical frequency-domain CD equalizer design. The figures also indicate the pre-FEC BER limit of  $3.8 \times 10^{-3}$ , consistent with the second-generation, hard-decision concatenated codes with 7% overhead [116].

For penalty-free equalization (with respect to the zero-dispersion curves), the RZ-shaped signals require longest overlap segments, and the Nyquist-shaped signals require

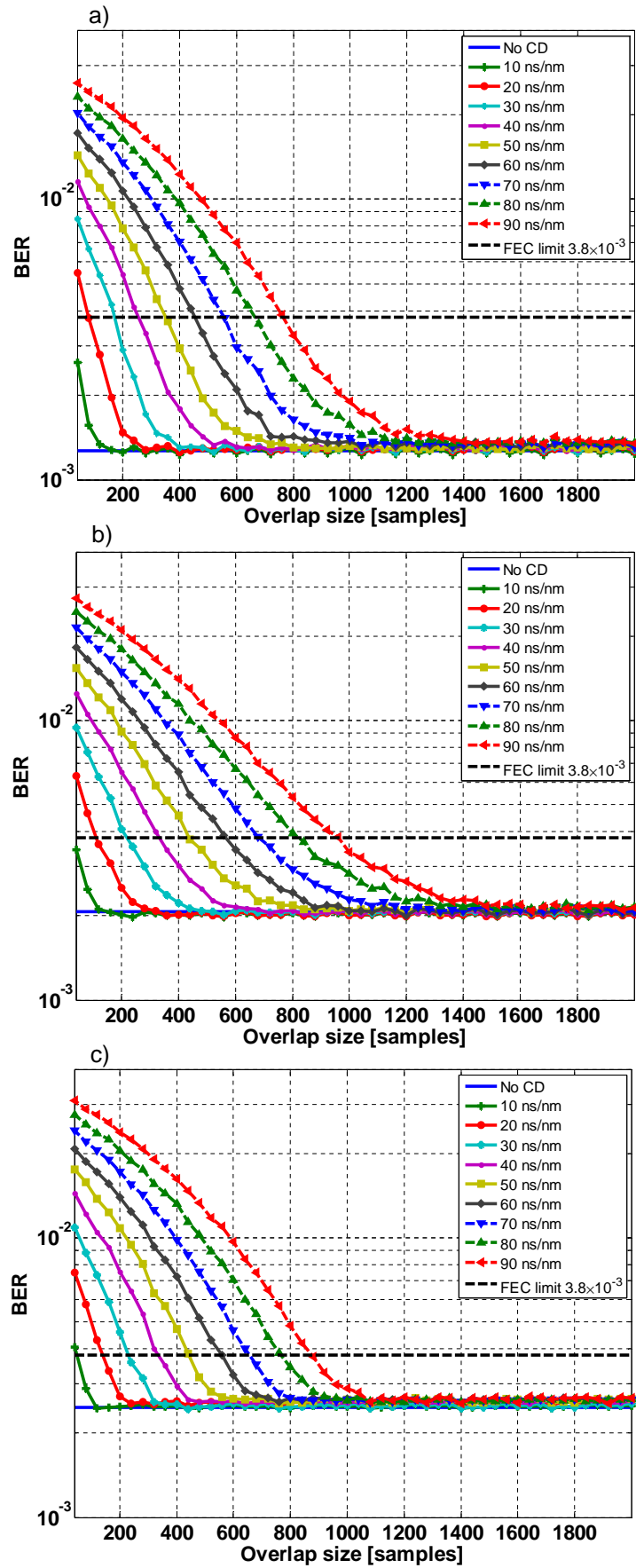


Figure 4.6: BER versus overlap size of the FD CD equalizer at 28 GBd for (a) NRZ-, (b) 50% duty cycle RZ-, and (c) Nyquist RC-shaped signals.

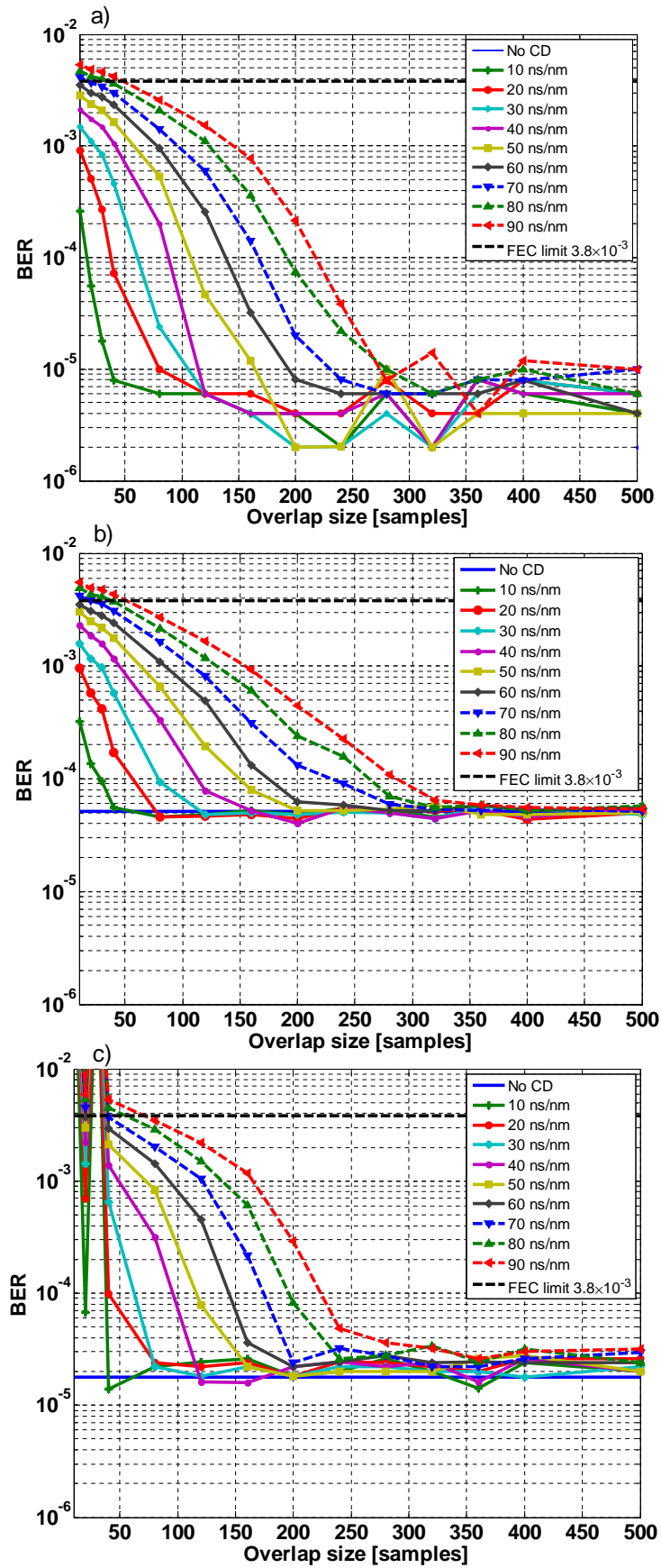


Figure 4.7: BER versus overlap size of the FD CD equalizer at 14 GBd for (a) NRZ-, (b) 50% duty cycle RZ-, and (c) Nyquist RC-shaped signals.

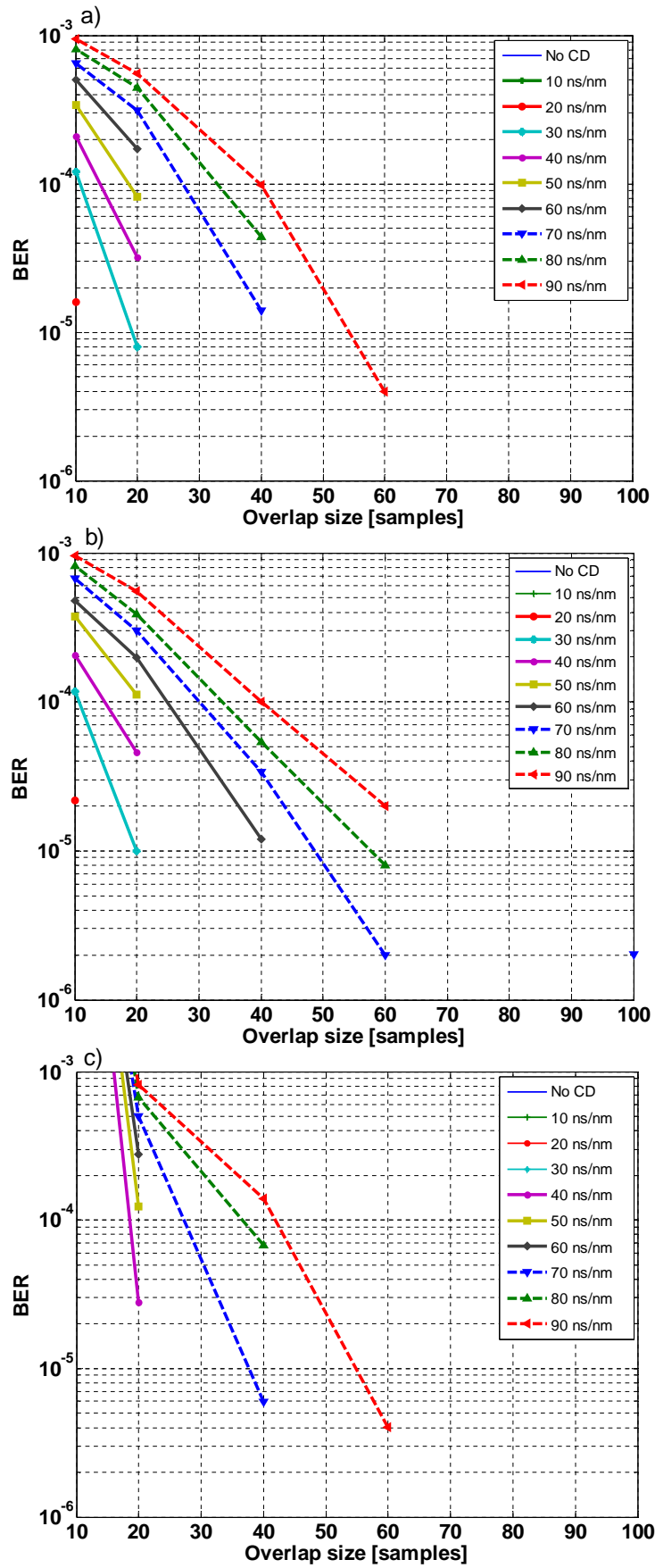


Figure 4.8: BER versus overlap size of the FD CD equalizer at 7 Gbd for (a) NRZ-, (b) 50% duty cycle RZ-, and (c) Nyquist RC-shaped signals.

the shortest ones, as expected from Figure 4.1. Nevertheless, at 28 GBd, those differences might not be so substantial as to justify, e.g., a DSP block design that would support overlap adjustment capabilities according to the signal pulse shape; though, those differences tend to increase with the symbol rate.

Figures 4.7(a-c) show the results for 14 GBd signals, as would result from the twofold symbol repetition of the rate switching scheme. Here, for NRZ and RZ signals, only the  $\geq 70$  ns/nm of accumulated dispersion requires more than 10-sample overlap size. This means that, for this particular setup, dispersion values up to 60 ps/nm (equivalent to a little over 3500 km for SSMF) can be seamlessly accommodated by a dynamic equalizer of  $\geq 17$  taps, completely bypassing static equalization. According to [117], the power dissipation of the CD equalizer for a 100G model by Clariphy constitutes about 21% of the total DSP power budget. Admitting the total power dissipation of 80 W, as specified by the OIF multisource agreement [118], this reduction is equivalent to  $\sim 17$  W.

This remarkable complexity improvement is due to two factors. Firstly, for the same oversampling factor,  $\kappa$ , overlap size decreases quadratically with the symbol rate, as seen from Equation (4.2), because both the temporal symbol spread,  $\Delta T$ , in the numerator is halved, and the sampling time,  $T_{Sa}$ , in the denominator is doubled. Secondly, the optical signal to noise ratio (OSNR) is roughly related to the electrical SNR through the symbol rate,  $R_s$  [7]:

$$\text{OSNR} = \frac{pR_s}{2B_{\text{ref}}}\text{SNR}, \quad (4.19)$$

where  $p = 2$  for polarization multiplexed signals, and  $B_{\text{ref}}$  is the reference bandwidth (commonly, 12.5 GHz). The SNR, in turn, impacts the bit error probability of the QPSK signal through the  $Q$ -function [76]:

$$P_b = Q\left(\sqrt{\text{SNR}}\right). \quad (4.20)$$

Thus, a twofold symbol repetition results in roughly 3 dB increase in signal quality. Conversely, the 14 GHz Nyquist-shaped signal in Figure 4.7(c) shows unstable performance for overlap  $< 40$  samples.

For the fourfold rate reduction in Figure 4.8, the NRZ and RZ signals (Figure 4.8(a,b)) achieved BER lower than the FEC limit for all tested accumulated CD values, allowing to turn off the static equalizer. The Nyquist signal (Figure 4.8(c)), again, showed unstable performance for overlap values  $< 20$ .

To conclude the chapter, we present illustrative computational complexity tables for a PM-QPSK system, for 70 ns/nm accumulated dispersion (circa 4200 km link length). The complexity is provided in Tops/s, and computed as  $M_b \times R_s \log_2 m$ . Table 4.2 shows

Table 4.2: Computational complexity for CD equalization [Tops/s];  $N_{\text{FFT}} = 8192$ ; Accumulated CD = 70 ns/nm; BER =  $3.8 \times 10^{-3}$

	28 GBd	14 GBd	7 GBd
NRZ	3.97	1.85	—*
RZ	4.03	1.85	—
RC	4.02	1.86	0.93

\* CD Equalizer turned off

Table 4.3: Computational complexity for CD equalization [Tops/s];  $N_{\text{FFT}} = 4096$ ; Accumulated CD = 70 ns/nm; BER =  $3.8 \times 10^{-3}$

	28 GBd	14 GBd	7 GBd
NRZ	3.89	1.68	—
RZ	4.03	1.69	—
RC	4.00	1.70	0.84

Table 4.4: Computational complexity for CD equalization [Tops/s];  $N_{\text{FFT}} = 8192$ ; Accumulated CD = 70 ns/nm; No penalty operation.

	28 GBd	14 GBd	7 GBd
NRZ	4.23	1.87	—
RZ	4.33	1.86	—
RC	4.10	1.86	0.93

Table 4.5: Computational complexity for CD equalization [Tops/s];  $N_{\text{FFT}} = 4096$ ; Accumulated CD = 70 ns/nm; No penalty operation.

	28 GBd	14 GBd	7 GBd
NRZ	4.50	1.72	—
RZ	4.75	1.71	—
RC	4.17	1.71	0.84

the complexity for the BER maintained constant at the pre-FEC limit  $3.8 \times 10^{-3}$  for transmission rates. Table 4.3 shows the same analysis for  $N_{\text{FFT}} = 4096$ . Tables 4.4 & 4.5 show the same analysis, but for zero penalty operation relative to the accumulated CD = 0 at 28 GBd, for  $N_{\text{FFT}} = 8192$  and  $N_{\text{FFT}} = 4096$ , respectively.

As the tables show, the mean complexity gain from a 28 to 14 GBd rate reduction is around 55% (slightly higher for smaller  $N_{\text{FFT}}$ , as expected from Equation (4.18)). The fourfold rate reduction allows to turn-off the static equalizers for the NRZ- and RZ-shaped, and reduces the complexity by  $\sim 80\%$  for the Nyquist-shaped signals.



## Chapter 5 RATE SWITCHING IN COHERENT OPTICAL SYSTEMS WITH CONVENTIONAL TRANSMITTERS

In this chapter we present the operation principle behind the symbol-repetition-based rate switching method. The method is designed to target conventional Tx systems – primarily in a static bandwidth allocation scenario – though, there is no impediment to use it with digitally-generated Nyquist pulses. Dynamic bandwidth allocation is also possible, provided that the network nodes support flex-grid operation. We also present a detailed investigation of the technique by computer simulations of PM-QPSK and PM-16QAM modulation formats, for the NRZ, RZ, and Nyquist pulse shapes. In particular, the robustness of the proposed scheme to PMD and signal phase noise is demonstrated. We conclude the chapter by experimental validation of the method using a PM-QPSK setup.

### 5.1 OPERATION PRINCIPLE

The principle of the proposed method is to reduce the transmission rate by repeating each symbol  $N$  times, causing an  $N$ -fold increase of the symbol time. While this approach lacks the flexibility offered by, e.g., a tunable clock reference, it has the advantage of being implemented by software in a way that no bit, frame or phase synchronization is required, allowing hitless rate switching. These software-implemented changes must include transmitter-receiver autonegotiation, appropriate framing and mapping procedures, etc.

The proposed receive-side DSP block architecture is shown in Figure 5.1. Without loss of generality, suppose that the system nominal transmission rate is 100 Gb/s, and the Rx analog-to-digital converters operate at 56 GSa/s, resulting in 2 samples per symbol at the symbol rate of 28 GBd (to include the 5% OTN and 7% hard decision FEC overheads); 4 samples per symbol at 14 GBd; and 8 samples per symbol at 7 GBd. The equalizer in Figure 5.1 is composed of three branches, B1, B2 and B3. The uppermost branch, B1, that operates at the nominal rate of 28 GBd, is identical to a common equalizer block architecture, composed of bulk and adaptive filters. The

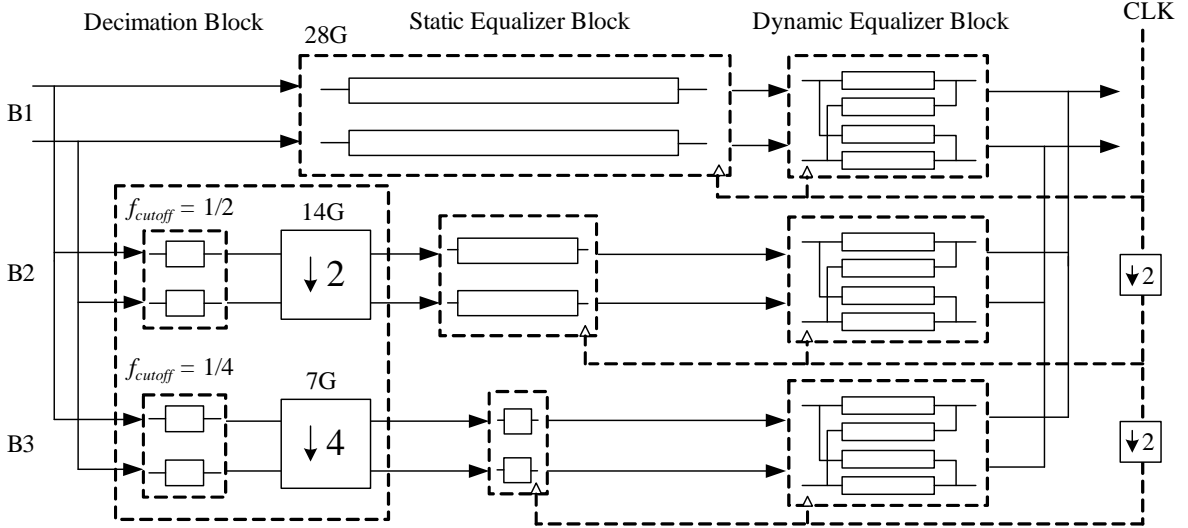


Figure 5.1: Receive-side DSP block architecture for symbol-repetition-based rate switching.

branches B2 and B3 operate at half and quarter the nominal rate (14 and 7 GBd), respectively. In addition to the equalizers, these branches have decimation blocks, composed of anti-aliasing digital filters and downsamplers. The anti-aliasing filters have cutoff frequencies  $f_{cutoff}$  of  $1/2$  and  $1/4$  the Nyquist frequency, or 14 and 7 GHz, and the downsamplers discard every second sample (B2) and every three out of four samples (B3), always resulting in two samples per symbol for the subsequent processing. The clock rates for B2 and B3 are reduced by 2 and by 4, and the increased sampling period allows to reduce the CD compensation bulk equalizer size (or the FFT overlap size for the FD equalization), as discussed in Section 4.2.

Note that the rate reduction factor is not necessarily of the type  $2^k$ ,  $k = 1, 2 \dots$ . For instance, a three-time sample repetition would yield an 18.67-GBd signal, where every two out of three samples are discarded.

The rate switching sequence for  $28 \rightarrow 14 \rightarrow 28$  GBd is shown schematically in Figure 5.2. Initially, the system operates at the nominal rate, and the upper branch B1 is active, producing the system output. The other branches are in a low-energy standby mode. At instant  $t_1$ , due to a reduction in traffic demand, the transmitter begins to repeat symbols, effectively halving the transmission rate. At the receiver, B2 is activated, processing the twice repeated and decimated incoming data in parallel with B1, until its adaptive equalizer converges at instant  $t_2$ . Then, B2 begins to produce the system output, and B1 is put in the standby mode. The up-conversion is performed in a similar way. Note, however, that due to its lower clock rate, B2 cannot process the data at 28 GBd, so the training of B1 must begin before the symbol rate returns to 28 GBd. Hence, B1 is activated at  $t_3$ , and its adaptive equalizer reaches convergence

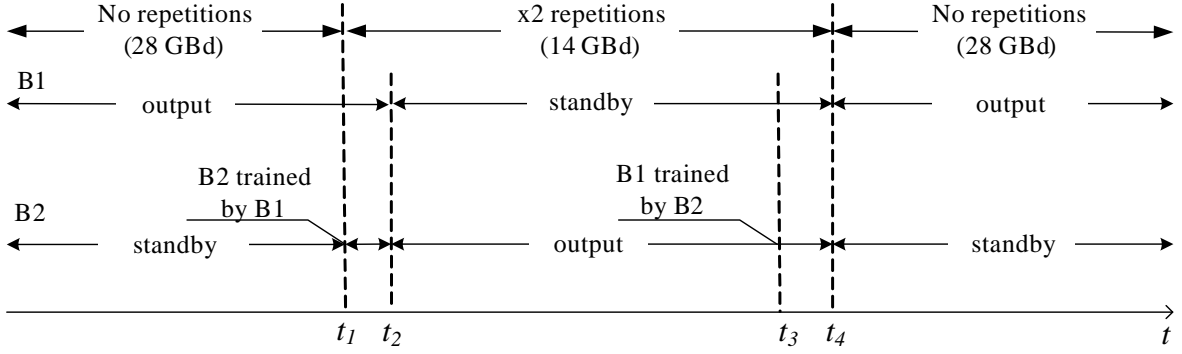


Figure 5.2: Rate switching sequence.

before  $t_4$ , when the transmitter returns to the nominal rate. From  $t_4$  onwards, B1 produces the system output, while B2 is put in standby. With the exception of the convergence period, only one branch is active at the time.

The inter-branch training procedure is depicted in Figure 5.3, showing the relevant parts of the equalizer of Figure 5.1. For down-switching from 28 to 14 GBd, the symbols produced by B1, after decision, are fed back to the adaptive equalizer of B2 to guarantee correct temporal and polarization alignment between the two branches (Figure 5.3(a)). Note that the output of B1 is downsampled by 2, to adjust to the rate of B2. Figure 5.3(b) depicts the situation after convergence, where B1 is in standby, and B2 produces system output. The up-switching (Figure 5.3(c)) is performed by upsampling the output of B2, and feeding it back as a training sequence for B1. After convergence and symbol rate up-switching, B1 produces the system output, and B2 is put in standby (Figure 5.3(d)).

## 5.2 SYMBOL REPETITION FOR DIFFERENT PULSE SHAPES

### 5.2.1 Non-return-to-zero pulses

For NRZ pulses, rate reduction by symbol repetition effectively doubles the time duration of the symbol, and, as a consequence, reduces spectral occupancy. Thus, optical and electrical filtering designed for the nominal rate would be excessively wide for half and quarter rate signals, allowing a substantial amount of noise into the receiver. Fortunately, the lowpass decimation filters (Figure 5.1) suppresses much of that noise.

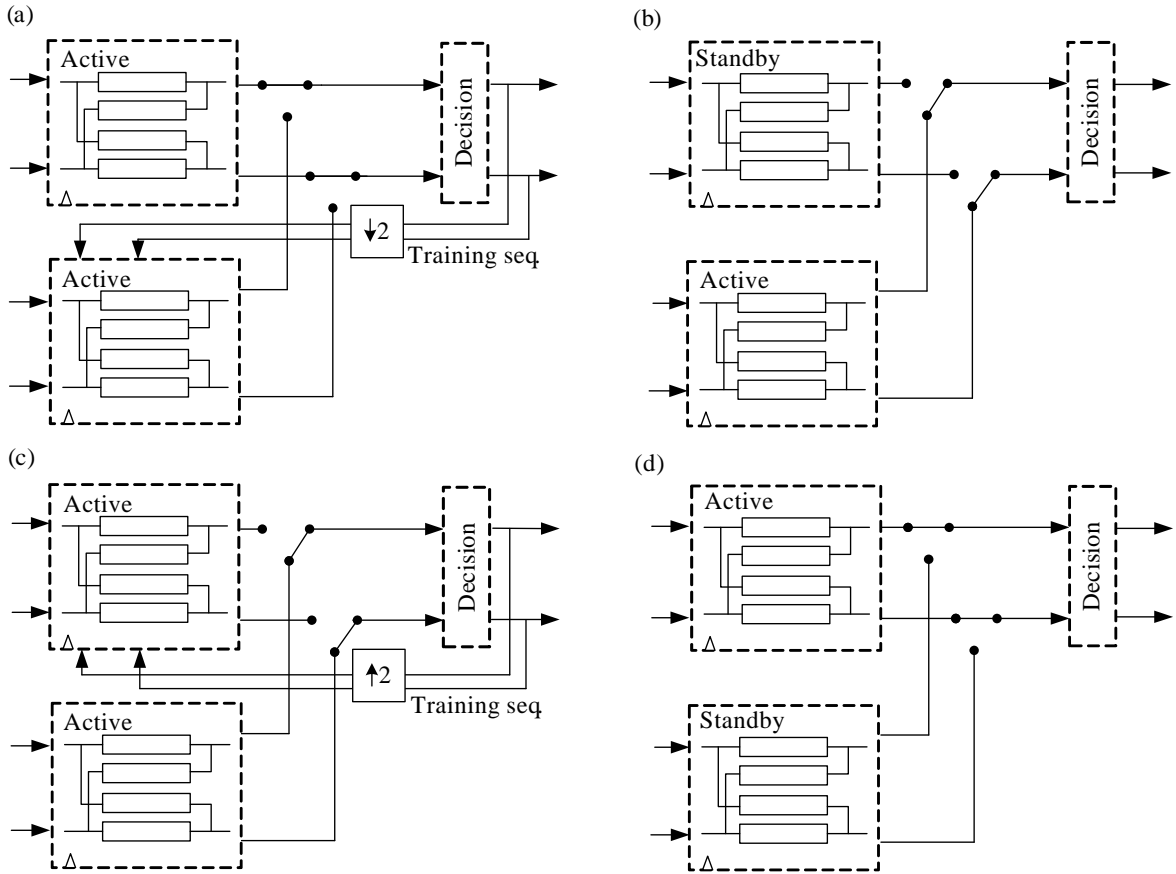


Figure 5.3: Rate switching sequence.

### 5.2.2 Return-to-zero pulses

Usually, analog-to-digital converters operate at (or close to) 2 samples per symbol, making reception more robust to timing issues. In systems with RZ shaping, one possible operating point is depicted in Figure 5.4. Here, the undistorted received signal is sampled at its peaks and valleys. If after analog-to-digital conversion the signal is downsampled by a factor of 2, there is a chance that all samples become zeroes (if the samples at the valleys are selected). Therefore, the use of antialiasing decimation filter is essential for RZ signals to avoid low energy sampling. The smoothing effect of the anti-aliasing filter is shown by the red-dashed curve. Naturally, in real systems some signal filtering is always present due to, e.g., component bandwidth limitations and residual CD, so that the discussed power zeroing scenario is highly unlikely. Still, slowly varying timing errors, as well as changes in PMD, may lead to unstable system performance if not using the anti-aliasing filter.

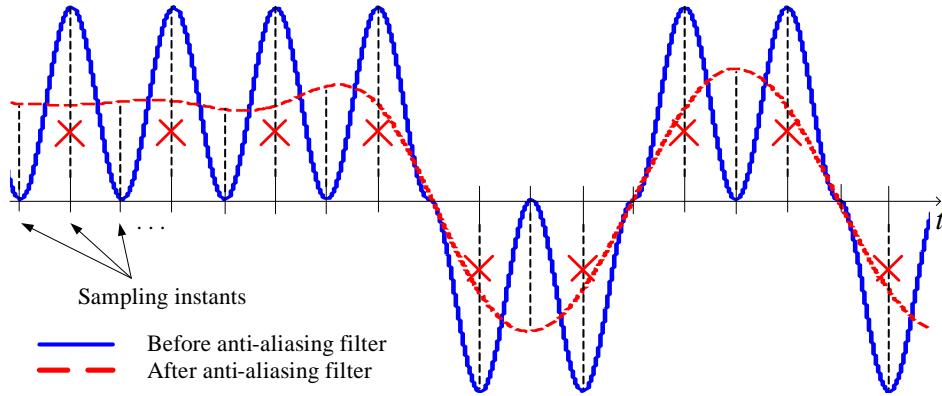


Figure 5.4: Effect of the anti-aliasing lowpass filter on RZ signals.

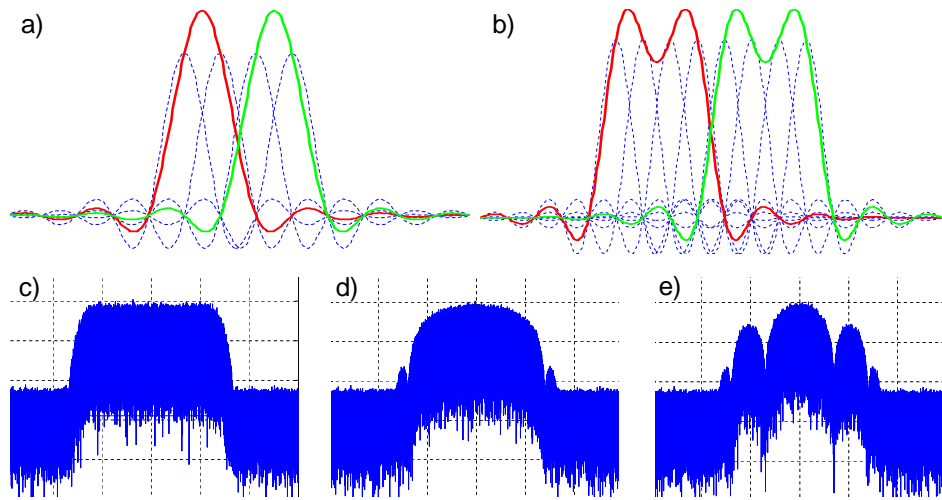


Figure 5.5: Nyquist-shaped symbols with: (a) x2 repetitions, (b) x4 repetitions. Power spectral density: (c) without symbol repetition, (d) x2 repetitions, (e) x4 repetitions.

### 5.2.3 Nyquist pulses

Figures 5.5(a) and 5.5(b) depict two adjacent symbols formed by twice and four times repeated Nyquist symbols, with the original Nyquist symbols shown in the background in dashed blue. The power spectral densities for the original Nyquist-shaped signal, twice Nyquist-symbol-repeated signal, and four times Nyquist-symbol-repeated signal are shown in Figures 5.5(c-e), respectively. Accordingly, the repetition of Nyquist pulses creates new pulse shapes with similar bandwidths, which is consistent with the purpose of reducing power consumption in the DSP in a static bandwidth allocation scenario.

It should be observed that the rate switching scheme can also be adopted to the dynamic bandwidth allocation scenario, where bandwidth adjustment is performed via optical filtering by the flex-grid-enabled wavelength-selective switches (WSSs). This

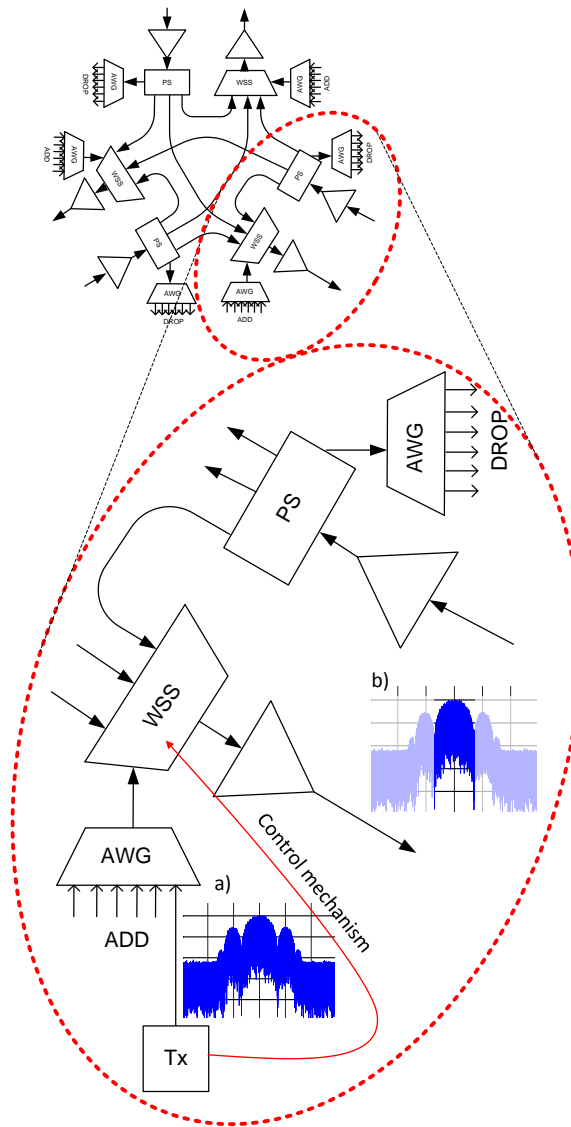


Figure 5.6: Bandwidth adjustment scheme for conventional Tx systems. AWG – arrayed waveguide grating; PS – power splitter; WSS – wavelength-selective switch. Insets: (a) PSD at the Tx output; (b) PSD after optical-domain spectral shaping.

concept is shown in Figure 5.6. The figure depicts a single degree of a 3-degree broadcast-&-select ROADMs. Here, a rate-reduced (by symbol repetition) signal is locally generated at the ADD port, occupying a full spectral window of a nominal rate signal (see Inset (a)). However, the flex-grid-enabled WSS can be set to adapt its passband to the symbol rate by a control mechanism, performing optical-domain spectral shaping, as shows Inset (b).

## 5.3 RATE SWITCHING INVESTIGATION BY COMPUTER SIMULATIONS

### 5.3.1 Simulation setup

The Matlab-built simulation setup is as follows. Pseudo-random binary strings generate the desired repetition pattern, being mapped onto the digital alphabet. A pulse shaping procedure creates the complex envelopes for X-pol. and Y-pol. tributaries, representing each symbol by 32 samples. After adding the carrier phase noise, the signal is filtered by a 50 GHz 4<sup>th</sup>-order Gaussian filter to emulate channel optical filtering. The additive white Gaussian noise (AWGN) is added to the signal to yield a desired optical signal-to-noise ratio (OSNR). Fiber propagation is simulated using a linear fiber model. DGD values are set deterministically. At the receiver, local oscillator (LO) phase noise is added, and the signal is filtered by a 19 GHz low-pass 2<sup>nd</sup>-order Gaussian filter that emulates the receiver photo-detector and transimpedance amplifier bandwidths. The receiver signal processing consists of resampling to 2 samples per symbol using native Matlab interpolation, adaptive equalization by the decision-directed least mean squares (DD-LMS) algorithm with the phase recovery along the equalization process [101]. After symbol decision, differential decoding is applied. Table 5.1 summarizes the simulation parameters.

Table 5.1: Simulation parameters for repetition-based rate switching numeric investigation.

Modulation format	QPSK 16QAM
Pulse format	NRZ, rolloff = 0.2 RZ, duty cycle = 50 % Nyquist (RC), rolloff = 0.2, shaping filt. size = 512
Simulation rates	Symbol rate = 28 GBd Samples per symbol = 32
Phase noise	Carrier linewidth = 200 kHz LO linewidth = 200 kHz
Dynamic equalizer algorithm	DD-LMS step-size = 0.001

### 5.3.2 Results and discussion

#### 5.3.2.1 Baseline performance

We compare the system performance at a specific symbol rate before and after down-switching. To assess the simulation results we adopt the commonly used pre-FEC BER reference of  $3.8 \times 10^{-3}$ , corresponding to second-generation hard-decision codes [116], [7]. Figures 5.7(a)–5.7(c) show the OSNR versus bit error rate (BER) baseline curves for NRZ, 50% duty cycle RZ, and Nyquist pulse formats; for QPSK and 16QAM modulation. The results were obtained by simulating a 28 GBd signal without symbol repetitions, with twice symbol repetition (14 GBd), and with four times symbol repetition (7 GBd). For x2- and x4-repeated signals 11-tap anti-aliasing filters with cutoff frequencies of 14 and 7 GHz were used. The anti-aliasing filters are linear-phase, finite impulse response (FIR) structures, designed by a native Matlab function using Hamming window.

At the pre-FEC BER of  $3.8 \times 10^{-3}$ , the NRZ and Nyquist signals gain about 3 dB in OSNR margin for every twofold reduction in the transmission rate. For the 50% RZ signal this factor is about 1 dB smaller.

Figure 5.7(d) shows the system performance under phase noise. The curves for 16QAM and QPSK were obtained for NRZ signals at OSNR = 20 and 14 dB respectively, including the effects of both the carrier and the LO noise. As expected, BER degrades quicker with the phase noise for the symbol-repeated signals than for the nominal rate signal, in particular, at 7 GBd (green, diamond-marked, dotted curves). Still, the 7% overhead pre-FEC BER limit crossing occurs at the linewidth values as high as 900 kHz for 16QAM, and 7 MHz for QPSK. Those requirements are easily met by commercial external cavity and distributed feedback lasers, whose typical linewidth values are in the range of a  $100 \sim 300$  kHz and  $2 \sim 5$  MHz, respectively. In the rest of the simulations we set the aggregate linewidth to 400 kHz, so that system performance is not limited by the phase noise.

#### 5.3.2.2 Up-switching error transients

The key idea of the proposed algorithms is that equalizer branches working at different rates can be trained for convergence before rate switching. This procedure, however, can lead to error transients during up-switching, because the training signal



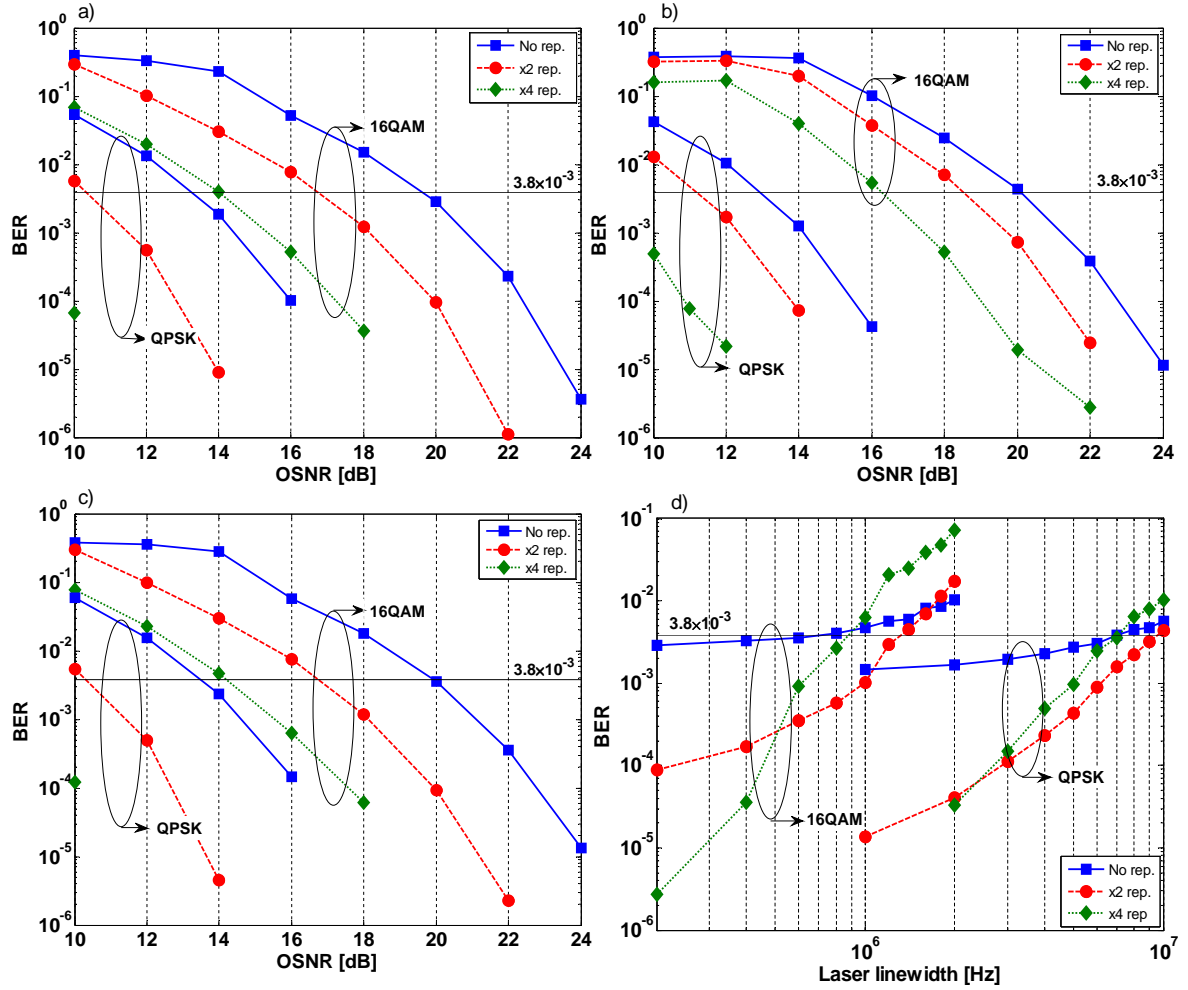


Figure 5.7: OSNR X BER reference curves (before rate switching): (a) NRZ, (b) RZ 50%, (c) Nyquist; (d) Laser linewidth *versus* BER.

from the lower branch lacks high-frequency information content, leading to a suboptimal convergence of the higher rate equalizer. The error transients are highly dependent on the length of the training period prior to switching. To illustrate this dependency, Figure 5.8 shows the transient errors for a  $7 \rightarrow 14$  GBd switching of an RZ-shaped (corresponding to the highest spectral content) 16QAM signal for different lengths of the training period. Accordingly, error transients for the  $14 \rightarrow 28$  GBd switching (not shown) presented a similar behavior. For better visualization, the figures show both the pre-FEC noise load, and the low noise conditions.

The error threshold in Figure 5.8, provided here for reference, is the  $100 - (3.8 \times 10^{-3}) \cdot 100 = 99.62^{\text{th}}$  percentile of the error amplitude at the nominal rate (28 GBd). In this way, symbols whose corresponding error amplitude is higher than the threshold, result in symbol errors with a high degree of probability. Thus, error transients may be avoided by ensuring full and stable convergence before up-switching.

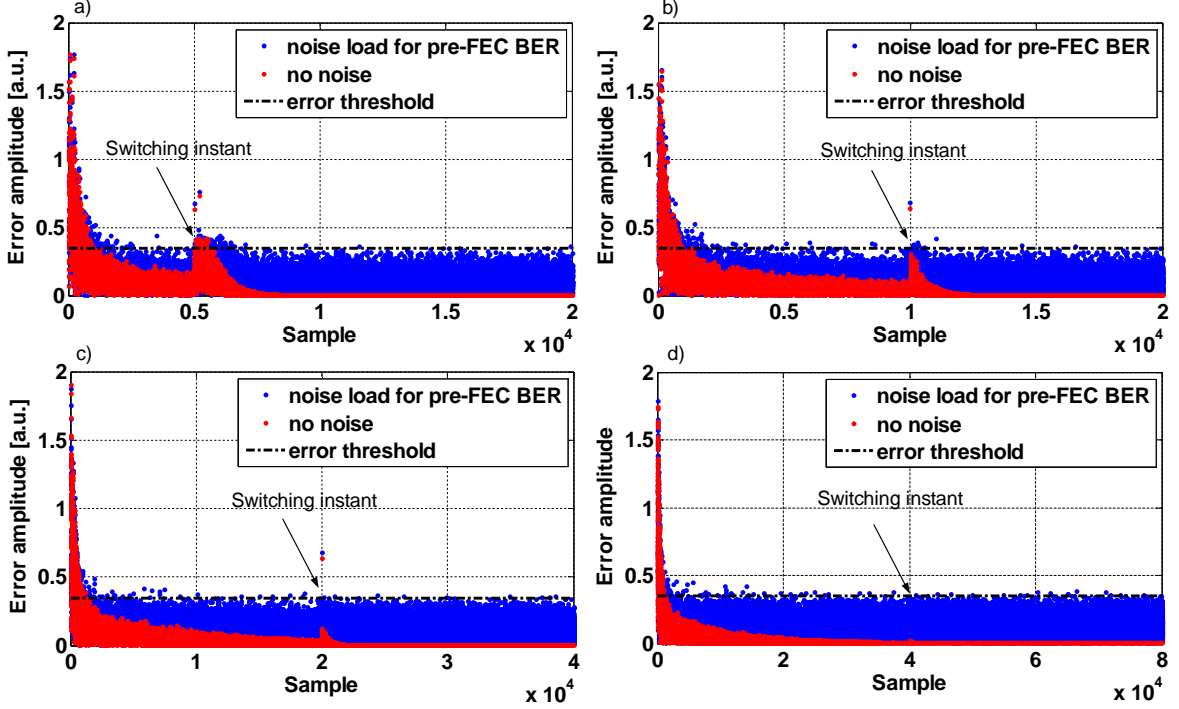


Figure 5.8: Error transients for a 7 → 14 GBd switching of an RZ-shaped 16QAM signal for different lengths training periods: (a) 5,000 symbols; (b) 10,000 symbols; (c) 20,000 symbols; (d) 40,000 symbols.

### 5.3.2.3 DGD tolerance

DGD causes relative time delays between the orthogonal components of the signal, potentially compromising the correct convergence at the switching instants. To investigate this impact we deterministically added different DGD values, maintaining the polarization state azimuth and ellipticity angles  $\varphi = 45^\circ$  and  $\epsilon = 0^\circ$ . Figure 5.9 shows the resulting bit error rates for QPSK and 16QAM signals, computed for OSNR = 14 and 20 dB respectively. Here, the left-column figures (Figures 5.9(a), 5.9(c), and 5.9(e)) show the results for the B1→B2→B1 GBd, or 28→14→28 GBd rate switching, while the right-column figures (Figures 5.9(b), 5.9(d), and 5.9(f)) show the results for the B2→B3→B2 GBd, or 14→7→14 GBd rate switching. Line-wise, the figures correspond to the three investigated pulse shapes: NRZ (Figures 5.9(a) and 5.9(b)); RZ 50% (Figures 5.9(c) and 5.9(d)); and Nyquist (Figures 5.9(e) and 5.9(f)). The results for QPSK are presented in continuous lines, and the results for 16QAM are presented in dotted lines, indicating robustness against DGD even for high values. Observe that, even though the BER for each signal portion is presented separately in Figure 5.9, it is computed by comparison with a single continuous bit sequence. Therefore, had DGD provoked any symbol misalignment between equalizer branches, it would have manifested in catastrophic BER spikes.

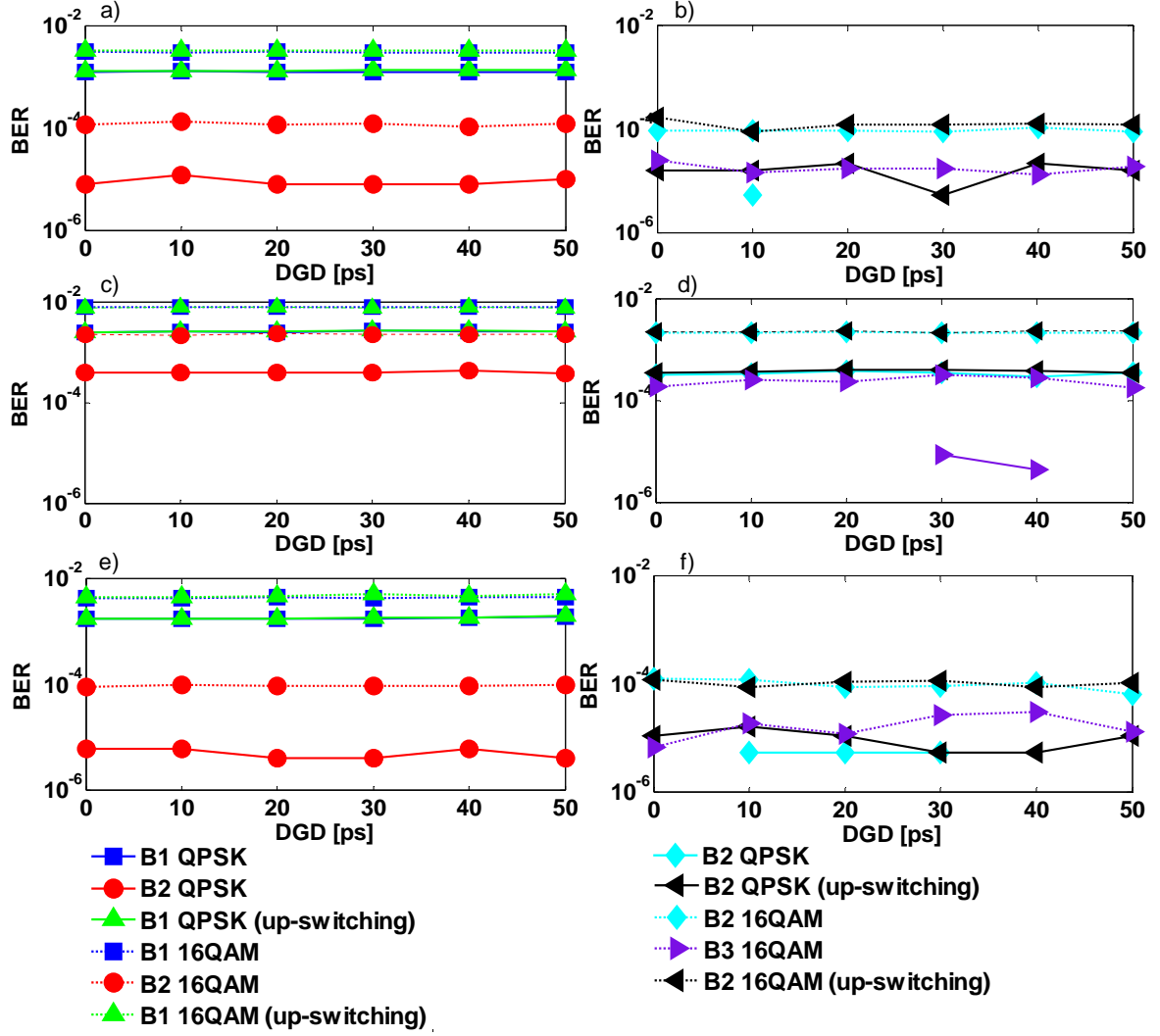


Figure 5.9: Symbol-repetition-based rate switching robustness against DGD for NRZ (a,b); RZ 50% (c,d); and Nyquist (e,f) pulses. Left column (a,c,e): B1→B2→B1 GBd switching. Right column (b,d,f): B2→B3→B2 GBd switching. OSNR = 14 dB for QPSK; OSNR = 20 dB for 16QAM.

## 5.4 EXPERIMENTAL VALIDATION

### 5.4.1 Experimental Setup

We validate the symbol-repetition-based rate switching in a 112 Gb/s PM-QPSK experimental setup, shown in Figure 5.10. A pulse pattern generator (PPG) produces 4x7 Gb/s bit streams, multiplexed into a single 28 Gb/s bit stream. The PPG-generated sequences are designed to yield a 28 Gb/s sequence composed of five parts: (1) A Matlab-generated arbitrary pseudo-random binary sequence (PRBS) with length

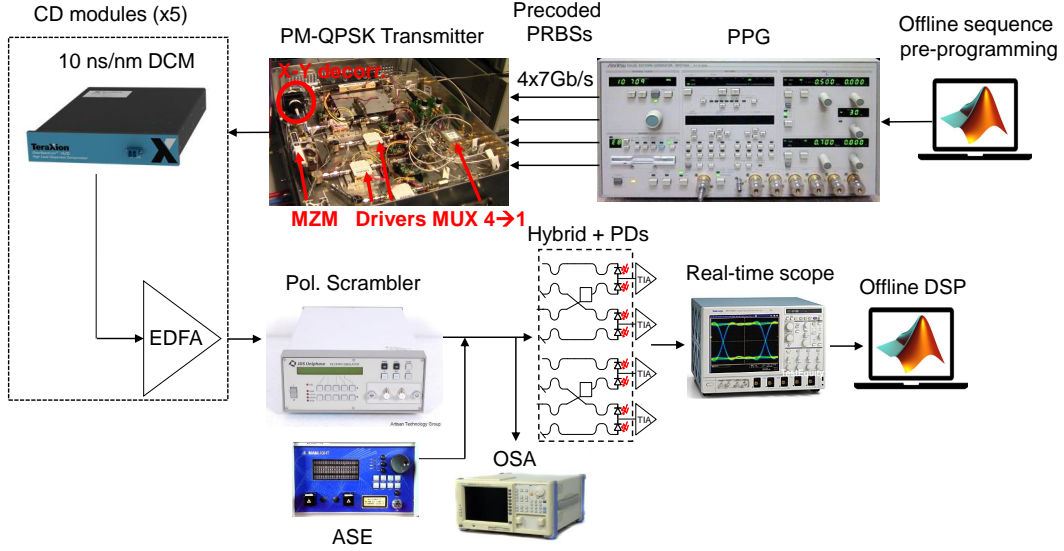


Figure 5.10: Experimental setup for validation of rate switching in conventional Tx systems.

$l \approx 50,000$  bits; (2) the same PRBS with twice repeated bits ( $l \approx 100,000$  bits); (3) the same PRBS with four times repeated bits ( $l \approx 200,000$  bits); (4) same as in (2), to simulate rate increase from 7 to 14 GBd; (5) same as in (1), to simulate rate increase from 14 to 28 GBd. This ratio between the lengths of the sequence components is set to compute the BER over an equal number of bits after decimation. The bit stream and its delayed version drive the in-phase and quadrature components of the QPSK modulator. A delay line produces the signal for the second polarization. Selectively activated, five concatenated 10 ns/nm dispersion modules generate the desired CD conditions. Additionally, polarization scrambling ensured an arbitrary polarization state at the receiver input. Optical noise is loaded to yield an OSNR = 16 dB. The four electrical outputs of a coherent receiver are sampled at 50 GSa/s by a 4-channel real-time oscilloscope and stored for offline post-processing.

For CD compensation we used a time-domain equalization; the corresponding filter lengths are summarized in Table 5.2. The coefficients were computed according to [35]. Adaptive 30-tap filters (for all branches) were blindly updated with the decision-directed least mean squares (DD-LMS) algorithm. The equalizer length was increased

Table 5.2: Lengths of the bulk equalizers [taps].

Branch	No CD	10 ns/nm	20 ns/nm	30 ns/nm	40 ns/nm	50 ns/nm
B1	–	253	507	761	1015	1269
B2	–	63	127	191	253	317
B3	–	15	31	47	63	79

to relieve possible timing error effects. The LP filters are Matlab-designed Hamming-window-based linear-phase FIR structures. The training phases corresponded to 15,000 samples for B1→B2 and B3→B2 switching, 7,500 samples for B2→B3 and 30,000 samples for B2→B1 switching. Note that the training period for all the transitions is 536 ns.

#### 5.4.2 Results and discussion

Figure 5.11(a) shows a single capture of the real-time oscilloscope of the above described rate switching pattern. If carefully observed, the different rate signals can be distinguished, due to their slightly different attenuation by the bandwidth-limited photodiodes and TIAs. The 28 GBd signal portion with no symbol repetition is the most attenuated, and also has the shortest duration. It is surrounded on both sides by the twofold-symbol-repeated sequences that correspond to the 14 GBd transmission. Finally, the fourfold-repeated sequence is the least attenuated, and is of the longest duration (though having the same number of symbols).

Figure 5.11(b) depicts the optical spectrum analyzer (OSA)-generated spectral traces of three individual signals: without symbol repetition; with twofold symbol repetition; and with fourfold symbol repetition (OSA resolution 0.1 nm). It confirms that symbol repetition results in a bandwidth reduction equivalent to that of 14 and 7 GBd signals. The 7 and 14 GBd signals exhibit strong sidelobes, characteristic to NRZ pulses, which should be eliminated in each branch by narrowband filtering. Figure 5.12 shows the obtained results. Figure 5.12(a) indicates the baseline performance for individual 28, 14 and 7 GBd sequences (that is, without rate switching) in a back-to-back (B2B) transmission, varying the length of the anti-aliasing low-pass filter from 0 to 11 taps. The results were averaged over ten independent data captures for each tested condition. Figures 5.12(b-f) show the BER obtained for the switching pattern 28→14→7→14→28 GBd (equivalently, B1→B2→B3→B2→B1), for each rate individually, under accumulated CD values of 10 to 50 ns/nm, respectively, in steps of 10 ns/nm. Here, the equal rates are plotted with the same line color: in solid line when result from down-switching; and in dashed line when result from up-switching (indicated inside figure inset legends as “down” and “up”). Again, the LP filter length varied from 0 to 11 taps.

Evidently, LP filters drastically enhance signal quality, especially, for the 7 GBd signals. This is likely because at 7 GBd more severe sidelobe aliasing occurs between digital spectral images. Yet, even as short as 5-7-tap filters yield great signal quality

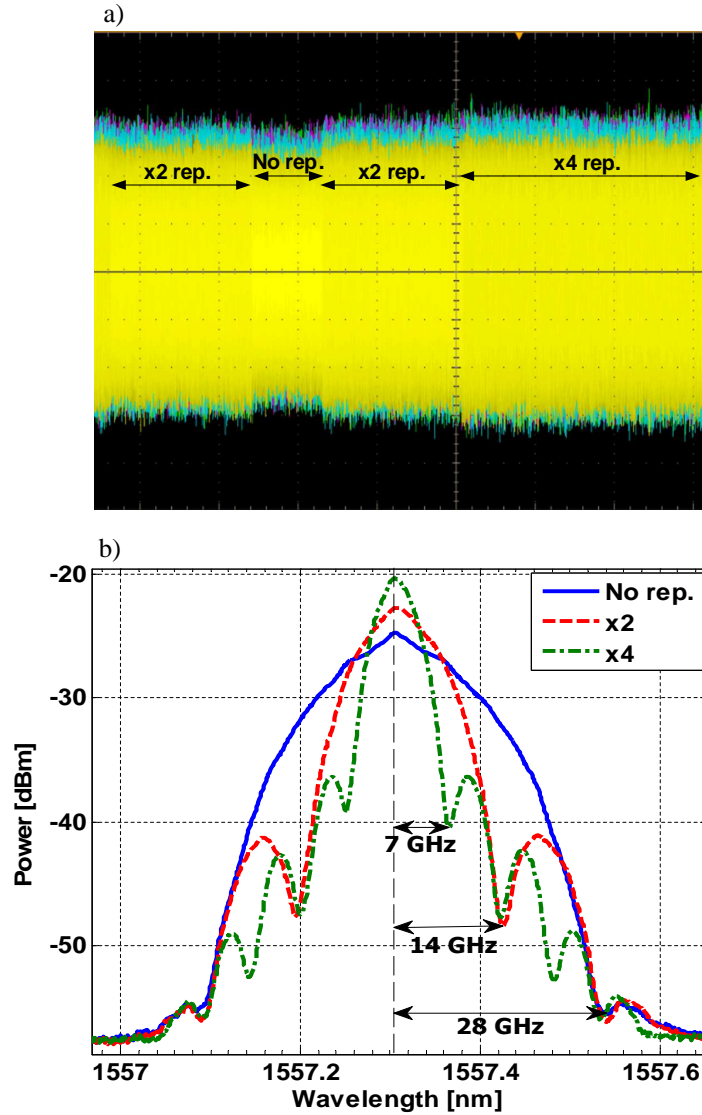


Figure 5.11: (a) Switching pattern observation in a single capture of a real-time oscilloscope. (b) Power spectral density traces of individual sequences, as captured by OSA.

improvement, reaching saturation for higher lengths. Unlike in Figure 5.9, the post up-switching sequences, with the exception of the 14 GBd for 20 ns/nm (Figure 5.12(c)) show slight performance penalty, in comparison with their post down-switching counterparts. This likely occurs due to clock phase error accumulation in the end portion of the sequence. In turn, the accumulated CD appears to have a marginal effect on system performance.

Due to the signal enhancement at lower rates, in addition to reducing power consumption, the proposed architecture is an enabler for software-defined transceivers, where the transparent reach can be traded-off with the client traffic rate. This property allows for more flexible routing during maintenance operations, or in case of optical restoration, compared to fixed-rate interfaces.

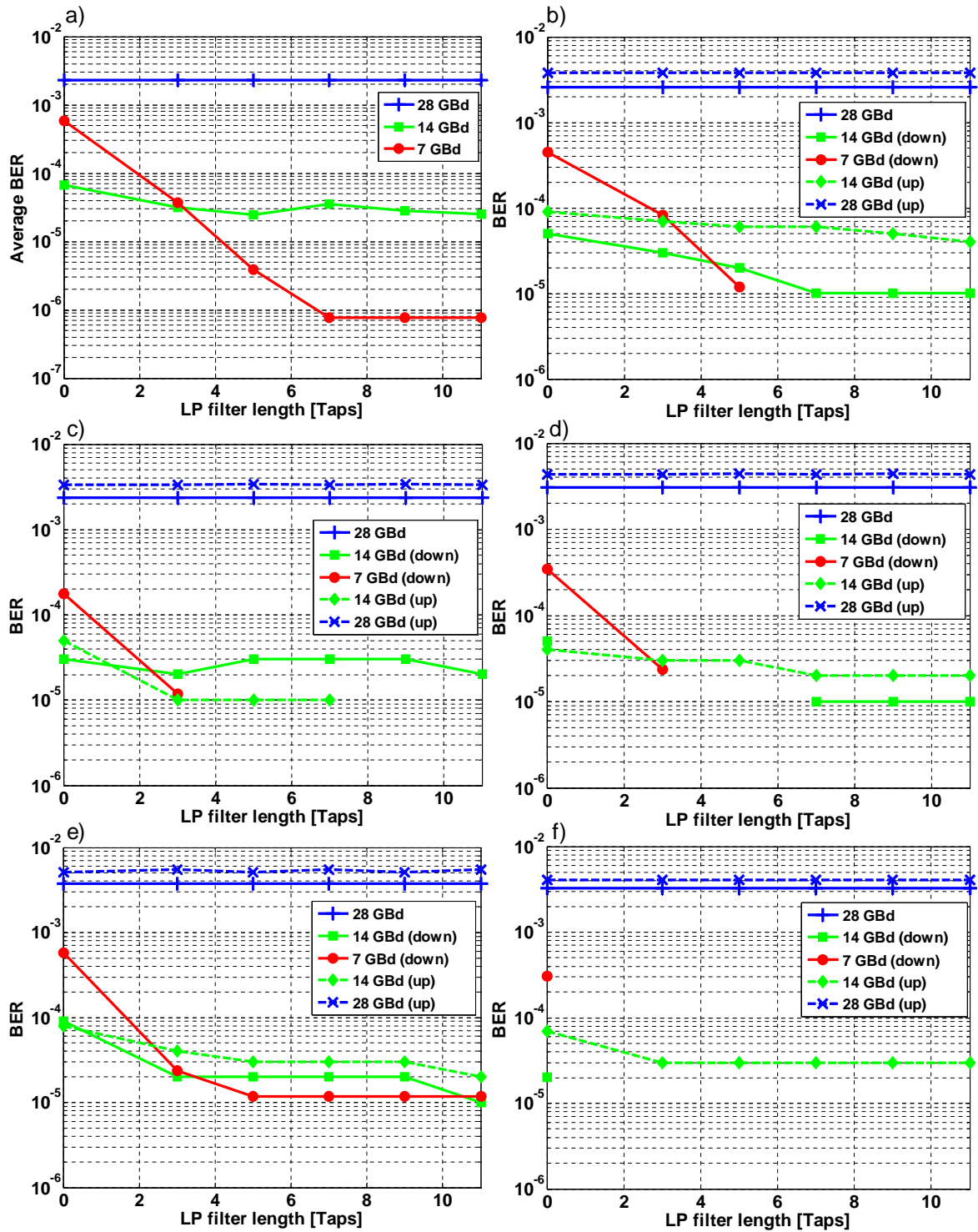


Figure 5.12: BER versus low-pass filter length: (a) Baseline performance for individual sequences in a B2B scenario – BER averaged over 10 data captures; BER for the rate switching pattern 28→14→7→14→28 GBd for (b) CD = 10 ns/m; (c) CD = 20 ns/m; (d) CD = 30 ns/m; (e) CD = 40 ns/m; (f) CD = 50 ns/m. Solid lines indicate results after down-switching, and dashed lines indicate results after up-switching.

## Chapter 6 RATE AND BANDWIDTH SWITCHING IN COHERENT OPTICAL SYSTEMS WITH DSP-CAPABLE TRANSMITTERS

In this chapter we present the operation principle behind the synchronous symbol rate switching method for digitally shaped optical signals, based on mutually synchronized transmit- and receive-side interpolators. We validate the method experimentally, showing that a gradually performed rate adjustment in sufficiently small discrete steps allows the dynamic equalizer at the receiver to successfully track signal changes. We discuss the method's applicability in elastic optical networks for bandwidth optimization. To conclude, we address the Tx-Rx interpolator synchronization.

### 6.1 OPERATION PRINCIPLE

#### 6.1.1 Synchronous rate switching architecture

Figure 6.1 depicts the DSP sequence for Tx signal generation, and the corresponding Rx blocks of the proposed multiple-rate transceiver. Digital symbols,  $a_k$ , are interpolated to the desired transmission rate, and the resulting sequence,  $a'_k$ , is convolved with the (Nyquist) pulse shaping filter. The shaped discrete-time signal,  $g_n$ , feeds the digital-to-analog converter (DAC) to produce a continuous-time signal  $g(t)$  that drives the optical modulator. Since  $g_n$  is sent to the DAC at a constant rate, the transmission rate (and signal bandwidth) is effectively set by the interpolator, with the symbol rate being inversely proportional to the interpolation factor. For example, for the highest supported symbol rate of 32 GBd, an interpolation factor  $L = 4/3$  (every 3  $a_k$  symbols converted to 4 samples of  $a'_k$ ) yields a 24-GBd signal. Accordingly, the number of digital samples of  $g_n$  that represent each transmitted symbol increases as the transmission rate is reduced. At the receiver, the output of the analog-to-digital converter (ADC) is interpolated by  $L^{-1}$ , producing a constant number of samples per symbol (commonly, 2) for subsequent DSP.



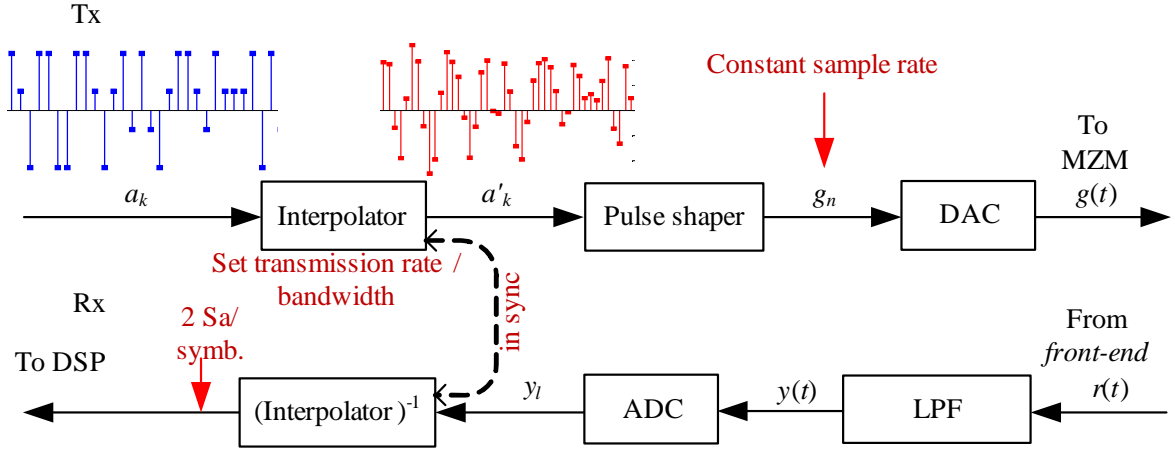


Figure 6.1: (a) DSP for rate switching transmitter. Insets: real part of an arbitrary 16QAM signal (blue); same signal portion after upsampling by factor of 1.5 (red)

Figure 6.2 shows the electrical bandwidth of the interpolator-produced raised-cosine-shaped (roll-off = 0.15) 32-, 24-, and 16-GBd QPSK signals, produced via computer simulation. Observe that here, unlike in Figure 5.5, the rate-reduced spectra remain Nyquist-shaped. This is due to the intrinsic low-pass filtering of interpolation process, absent in symbol-repetition-based switching.

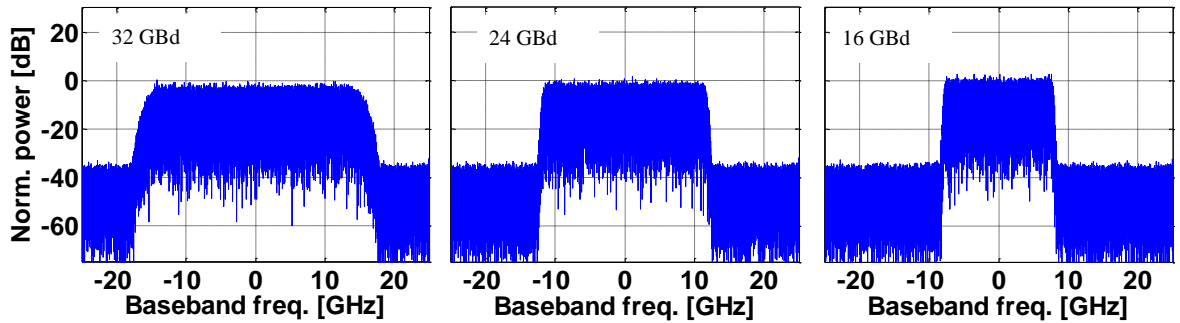


Figure 6.2: Electrical bandwidth of the interpolator-produced raised-cosine-shaped 32-, 24- and 16-GBd QPSK signals.

### 6.1.2 Small-step outage mitigation

So far, the system may be designed to operate at any fraction of the nominal transmission rate. For rate switching, an additional synchronization mechanism is required to ensure that both interpolators are aware of the precise switching instants. However, an attempt to switch online between two distant rates (e.g., between 32 and 16 GBd) would result in the DE perturbation with outage and possible loss of signal

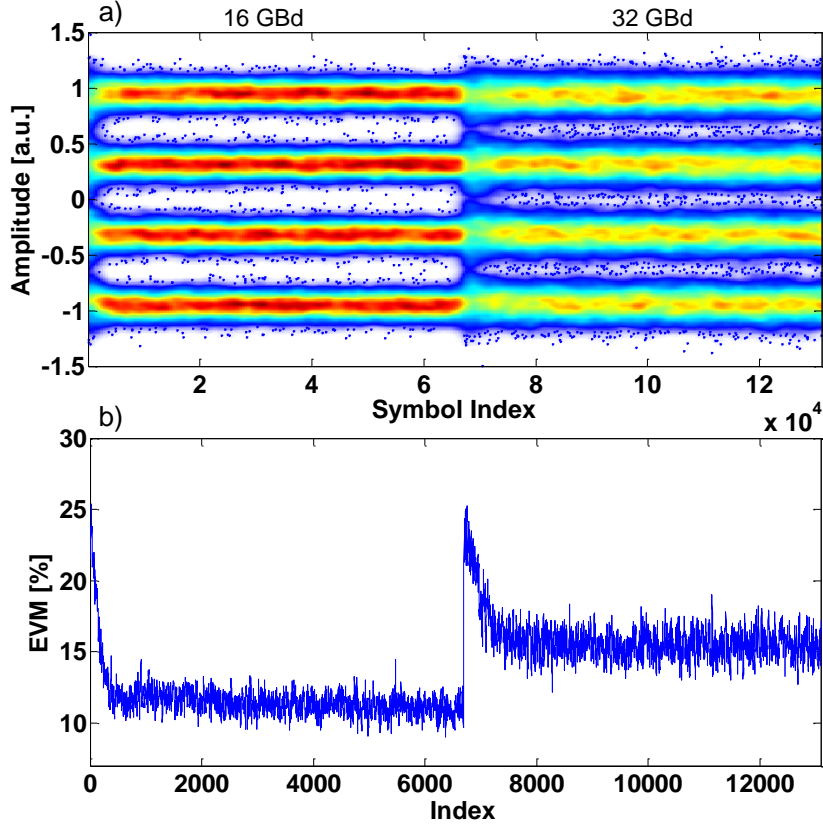


Figure 6.3: Simulation results of 16 to 32 GBd single-step switching for a PM-16QAM signal: (a) temporal evolution of X-pol. in-phase signal component; (b) The EVM computed over 100 symbols.

tracking, requiring system resynchronization. This adversity is most distinctive during up-switching, because the low symbol rate signal lacks the high-frequency channel information, required by the DE adaptive algorithm. For instance, assume a system operating at 16 GBd before up-switching. For a perfect Nyquist-shaped pulse, the first spectral null occurs at half of the symbol rate, and most spectral content is contained at  $[-8 \text{ GHz}, +8 \text{ GHz}]$  around the carrier frequency. An abrupt rate increase to  $R_s = 32 \text{ GBd}$  would generate a high-frequency spectral content between  $[-16 \text{ GHz}, -8 \text{ GHz}]$  and  $[8 \text{ GHz}, 16 \text{ GHz}]$  which is not equalized by the DE, yielding a perturbation.

This condition is avoided if the switching is done in a number of sufficiently small discrete steps, so that the DE is able to track signal changes. To illustrate this phenomenon, Figures 6.3-6.4 shows the results of a computer simulation of symbol rate up-switching from 16 to 32 GBd, for a polarization-multiplexed 16QAM signal. The signal was corrupted by AWGN noise; a 10-ps differential group delay (DGD), added using the waveplate model [56] with 10 randomly coupled waveplates; and phase noise, corresponding to carrier and local oscillator (LO) linewidths of 100 kHz. The receive-side DSP included radius-directed-based adaptive equalization [119] and blind phase

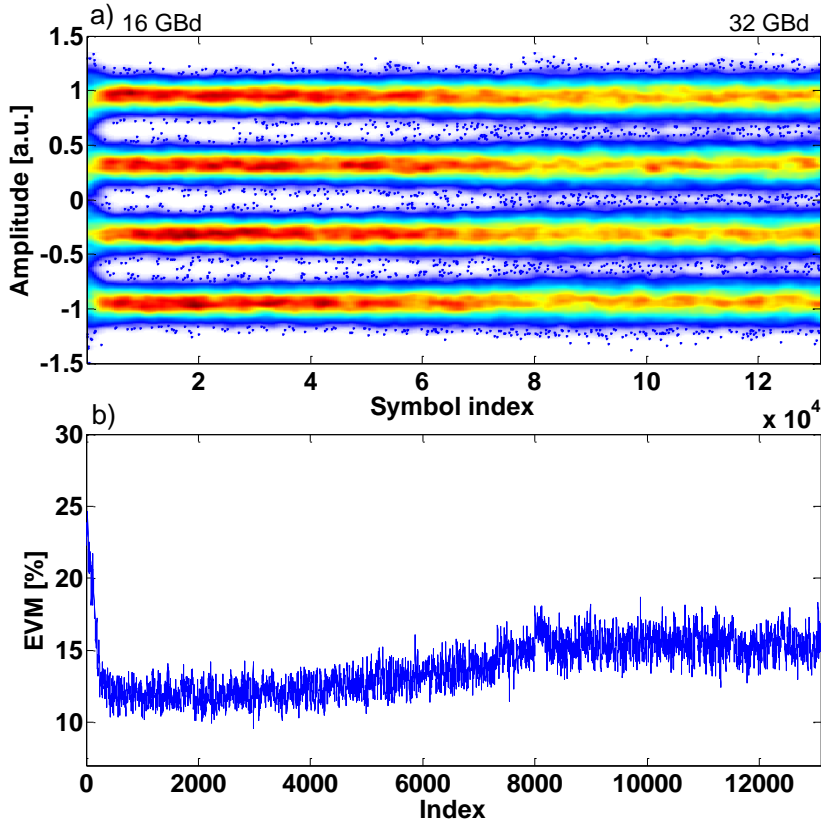


Figure 6.4: Simulation results of 16 to 32 GBd 10-step switching for a PM-16QAM signal: (a) temporal evolution of X-pol. in-phase signal component; (b) The EVM computed over 100 symbols.

search [102].

Figure 6.3 shows the temporal evolution of the real part of the in-phase component of the X polarization of the recovered signal, for a single-step switching, whereas Figure 6.4(a) shows the same result for a 10-step switching. Figures 6.3(b) and 6.4(b) show the respective error vector magnitudes (EVMs), computed for every 100 received symbols. In addition to the expected signal quality reduction with the rate increase, single-step switching shows severe error transients. In fact, the DE loses signal tracking, and has to converge once again. In case of blind equalization, the interplay of the polarization-dependent impairments and noise may provoke convergence to local minima (corresponding to delays/advances of the signal, mutual delays or swapping between polarizations, or singularities), requiring resynchronization. Conversely, the DE successfully tracks the signal during the 10-step switching, not showing any error spikes above the nominal rate (32 GBd) error floor.

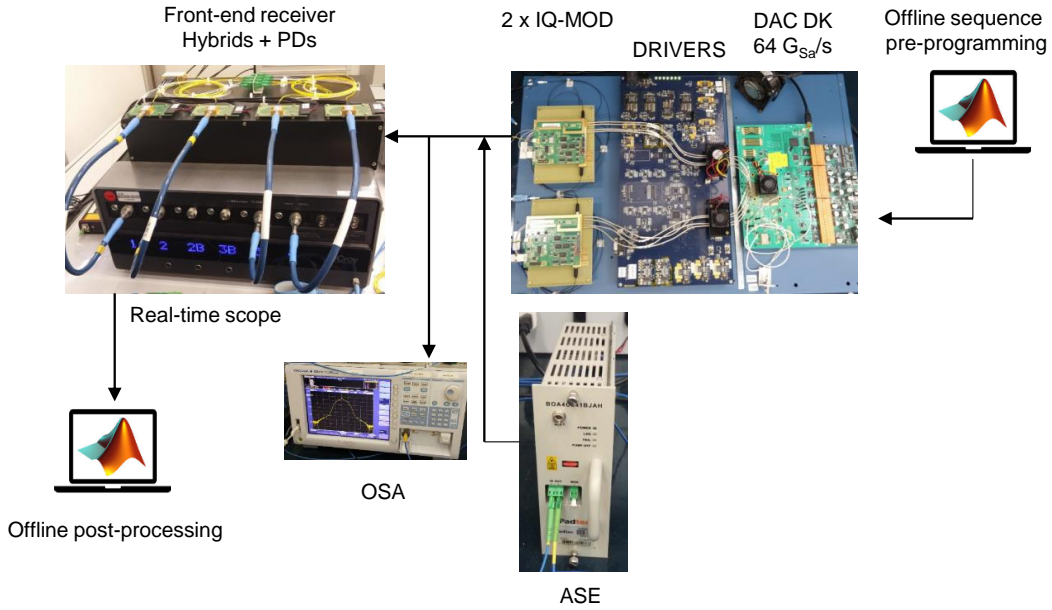


Figure 6.5: Experimental setup for validation of rate switching in DSP-capable Tx systems.

## 6.2 EXPERIMENTAL SETUP AND PROCEDURE

The experimental setup, shown in Figure 6.5 consists of a DAC development kit (DK) operating at 64 GSa/s (8-bit resolution), with memory capacity for recurrently repeating  $4 \times 262144$ -sample sequences, used as the I and Q components for the X and Y-pol. The four DAC outputs drive the dual-polarization IQ modulator to produce a polarization-multiplexed optical signal. Optical noise is loaded to yield a desired OSNR, and the signal is detected by a polarization diversity coherent receiver, whose four outputs are filtered by 16-GHz electrical low-pass filters, and sampled at 80 GSa/s by a 4-channel real-time oscilloscope for offline processing.

The Tx sequence generation and pre-processing is performed in Matlab. Four pseudo-random bit sequences are mapped pairwise onto the QPSK alphabet to produce X and Y-pol symbol sequences. Those are interpolated to create the desired rate and bandwidth switching pattern using native Matlab resampling, with FIR filter order = 25. The resulting samples are convolved with a 512-tap raised-cosine pulse shaping filter (2 Sa/symbol, roll-off = 0.15), adjusted in amplitude, and loaded onto the DK internal memory.

The Rx post-processing includes skew compensation, downsampling to 64 Sa/s, and Gram-Schmidt orthogonalization. Next, the signal is piecewise interpolated by the corresponding factors to produce 2 Sa/symbol, and equalized in a MIMO DE,

adapted by the constant modulus algorithm. Chromatic dispersion is assumed to be compensated by static equalizers at a constant rate prior to interpolation. Lastly, blind phase search is applied to compensate for the aggregate phase noise.

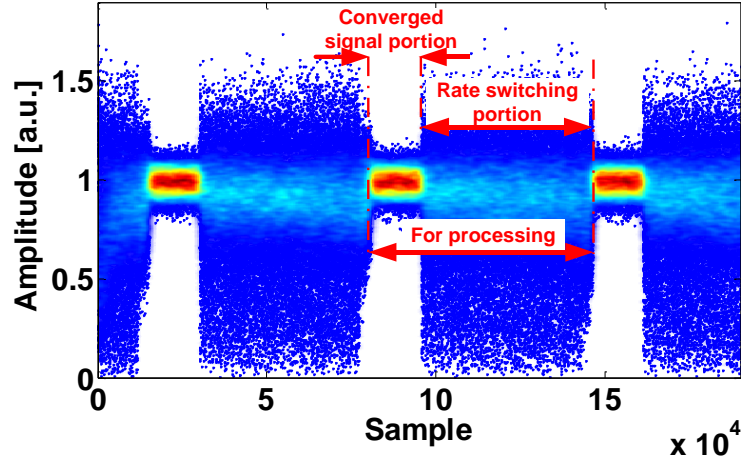


Figure 6.6: Experimental procedure for sequence alignment.

To achieve Tx and Rx interpolators alignment, we ensure that the oscilloscope capture window contain at least two switching pattern sequences. We first process the captured sequence at a constant rate, without applying interpolation. Note that in this case, the DE only converges for the signal portions with two samples, and diverges for the signal portion that contains fractionally-interpolated symbols. We then extract the signal amplitude. For QPSK, this operation maps the CMA-generated annulus onto constant magnitude, resulting in the pattern shown in Figure 6.6. A single period of the recurrent pattern corresponds to the desired sequence, which we extract for subsequent processing. Next, by correlating the converged part of the sequence with the transmitted symbols we pinpoint the exact switching instances.

### 6.3 RESULTS AND DISCUSSION

Figures 6.7(a-b) show the temporal evolution of the in-phase X-pol. component of the received PM-QPSK signal after processing. The OSNR was set to 16 dB to yield a pre-FEC BER of  $\approx 2 \times 10^{-3}$  at 32 GBd. The plots display rate switching from 32 to 16 GBd and from 16 to 32 GBd, respectively, in 10 steps of 7000 symbols. The omitted components (Q/X-pol; I,Q/Y-pol) exhibit similar behavior. The figures also indicate the exact switching instants corresponding to the changes in  $L$  of the Tx and

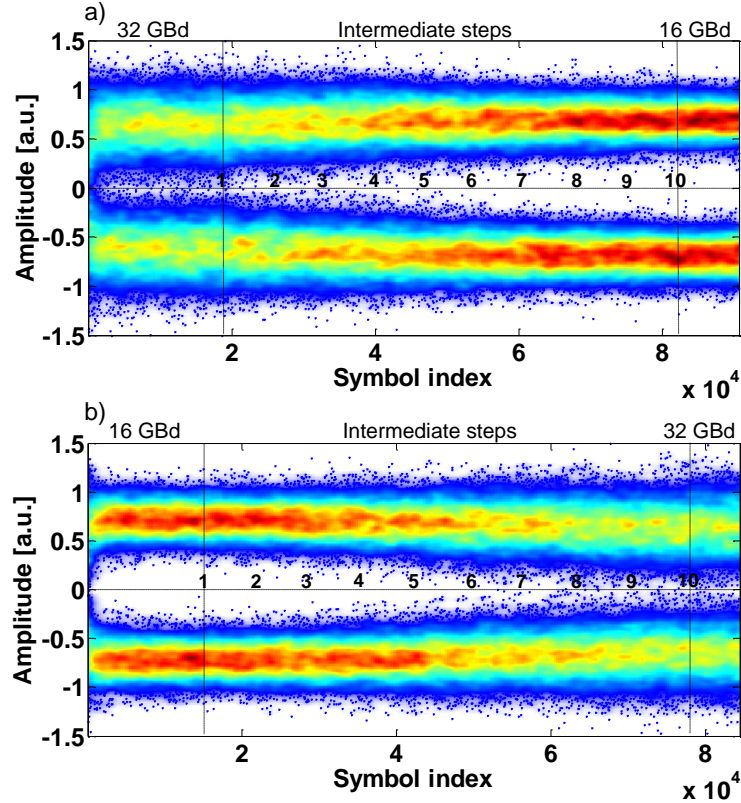


Figure 6.7: X-pol I component at OSNR = 16 dB for (a) 32→16 GBd switching and (b) 16→32 GBd switching.

Rx interpolators. As expected, signal quality improves with rate reduction due to the out-of-band noise filtering by the interpolator LPF.

Figures 6.8(c-d) show the estimated error vector magnitude (EVM), computed for every 100 symbols for the respective switching patterns. Clearly, the 10-step rate switching ensures smooth transitions in both directions for the investigated setup.

For reference, Figures 6.9(a-b) show the signal constellations for individual 32 and 16 GBd PM-QPSK signals, indicating the BER, and Figure 6.9(c) shows the respective power spectral densities at the receiver.

Additional care must be taken with timing error detection (TED), and the digital CD compensation. The TED must be performed after the Rx interpolator, to ensure it is not affected by the rate switching. In turn, to maintain a constant sample rate for CD compensation, the Rx interpolator must be placed after the CD equalizer. Here, the drawback is that the rate adjustment cannot be exploited to reduce CD-compensation-associated power consumption, as in the symbol-repetition-based rate switching (see Section 5.1). Yet, the power consumption of the following DSP blocks may be reduced quasi-linearly because of the decreased throughput. Further, FEC-associated power consumption may be greatly reduced by exploiting the enhanced signal quality.

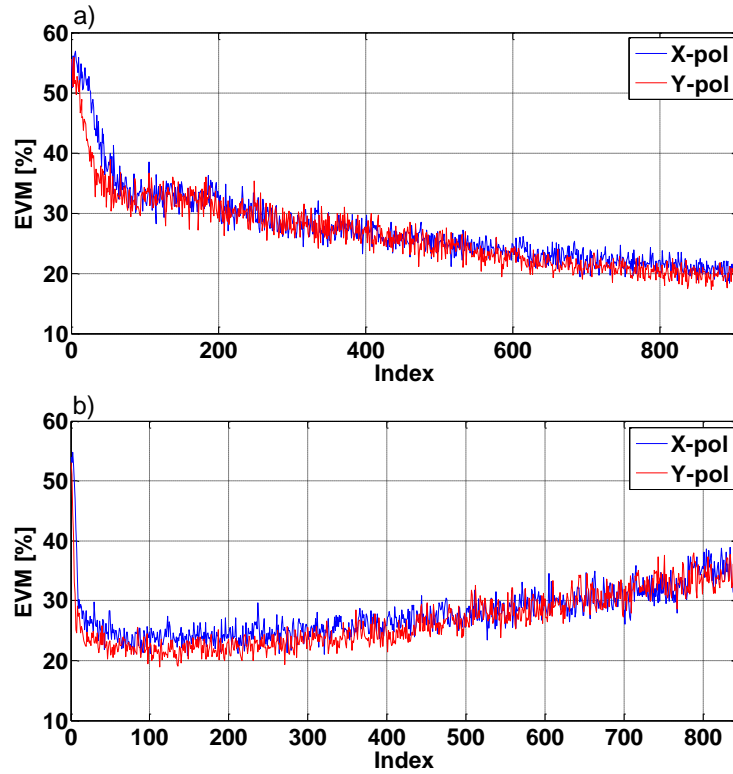


Figure 6.8: 100-symbol averaged EVM for (c) 32→16 and (d) 16→32 GBd.

This benefit cannot be underestimated, since FEC decoder power dissipation in 200G 16QAM systems doubles with respect to their 100G QPSK counterparts, constituting circa 35% of all the DSP consumption [117].

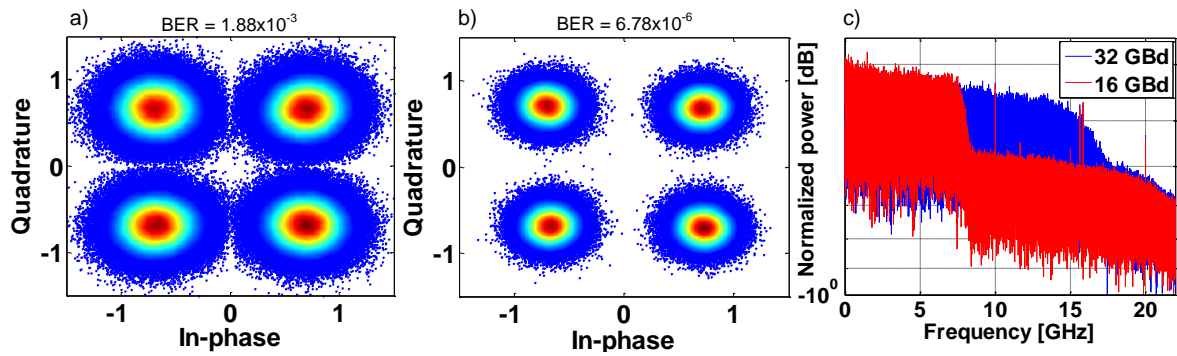


Figure 6.9: Individual constellation plots for (a) 32 and (b) 16 GBd; (c) PSD at the receiver for 32 and 16 GBd.

## 6.4 BANDWIDTH ADJUSTMENT FOR NETWORK OPTIMIZATION

In the context of elastic networks bandwidth optimization, the released spectrum during low traffic conditions may be used to accommodate short-living opportunistic connection demands, such as in data center traffic. This feature may be effectively implemented by combining gradual symbol rate switching with the hitless push-pull defragmentation technique (experimentally demonstrated in [18]), as illustrated by an example in Figure 6.10.

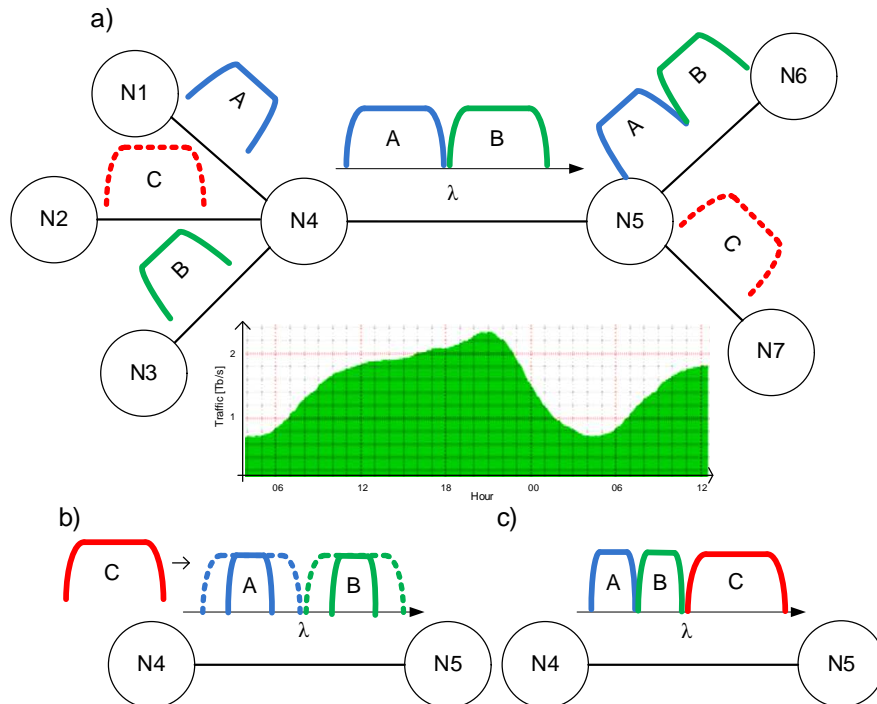


Figure 6.10: Bandwidth release/allocation using symbol rate switching & push-pull defragmentation. (a) Nominal rate operation no available bandwidth between N4-N5 for service request C. (b) Symbol rate reduction induces reduction of the occupied bandwidth. (c) Push-pull defragmentation releases bandwidth for service request C. Inset: aggregate traffic at the London Internet Exchange point (LINX) [34].

Here (Figure 6.10(a)), channels A and B, originated at nodes N1 and N3, copropagate over the same fiber between nodes N4 and N6. If there is a request for a temporary connection between nodes N2 and N7, as may arise during, e.g., a data center backup operation, the request cannot be attended, because there is no available bandwidth between N4 and N5. However, when the client traffic is sufficiently low, request C can be accommodated in two steps. First (Figure 6.10(b)), the symbol rate (and bandwidth) of A and B is adjusted using the gradual symbol rate switching method, and then, both



channels are spectrally grouped (Figure 6.10(c)) by the push-pull technique to release sufficient bandwidth for C. Both steps are hitless from the client-side standpoint. For reference, the inset of Figure 6.10 shows the daily traffic fluctuations of the London Internet Exchange point (LINX), ranging from 0.7 to 2.3 Tb/s [34].

## 6.5 IMPLEMENTATION CONSIDERATIONS

From the hardware complexity standpoint, the principal difference introduced by the rate and bandwidth adjustment scheme are the Tx and Rx multi-rate supporting interpolators. As mentioned earlier, this case is suitable for Lagrange interpolators, implemented via simple transversal FIR structures, due to their ability to interpolate any fractional interval. To recall, given a set of four samples  $Sa_0 - Sa_3$ , taken at instants  $t_0 - t_3$ , a third-order Lagrange interpolator computes a sample  $Sa_\mu$ , corresponding to instant  $t_\mu$ , as:

$$Sa_\mu = \sum_{i=0}^3 w_i Sa_i, \quad (6.1)$$

being  $w_i$  the filter coefficients, and  $\mu$  a fractional interval, so that  $t_1 < t_\mu \neq t_2$ , as shown in Figure 6.11. In turn,  $w_i = f(\mu)$ ; that is, for every  $\mu$ , the four filter coefficients must be recalculated.

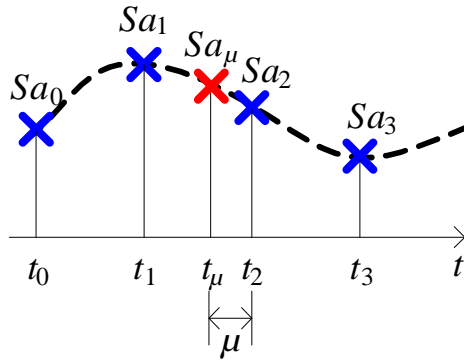


Figure 6.11: Interpolation of a single sample at  $t_\mu$  from four data samples by a 3<sup>rd</sup> order polynomial.

Let us address interpolator implementation through an example. Suppose, the adjustment scheme supports 11 linearly-spaced rates with the corresponding bandwidth

Table 6.1: Rate and bandwidth adjustment exemplary parameters.

Supported rates [GBd]	16	17.6	19.2	20.8	22.4	24	25.6	27.2	28.8	30.4	32
Interp. factors	2	1.82	1.67	1.54	1.43	1.33	1.25	1.18	1.11	1.05	1
Fraction approx.	2	9/5	5/3	3/2	7/5	4/3	5/4	7/6	9/8	15/14	1
Fraction approx. (dec.)	2	1.8	1.67	1.5	1.4	1.33	1.25	1.17	1.13	1.07	1

values from 16 to 32 GBd, as presented in the first line of Table 6.1. If 32 GBd is the nominal symbol rate, 10 steps are required to switch from 32 to 16 GBd. The corresponding interpolation factors are given in the second line of Table 6.1.

For reasons that will soon become clear, let us approximate those interpolation factors by simple fractions with relatively small numerators, as shown in the third line of Table 6.1. For comparison, the corresponding decimal-notation values are provided in the fourth line. The latter approximation has virtually no impact on hitless switching performance.

Each interpolation factor of the form  $x/y$  ( $x > y$ ), that is, every  $y$  original samples yield  $x$  interpolated samples, generates a set of  $x - 1$  different  $\mu$  values, and thus, requires  $x - 1$  different, periodically repeating, 4-tap FIR structures. This feature is illustrated in Figure 6.12 for a  $4/3$  (Figure 6.12(a)), and  $10/7$  (Figure 6.12(b)) upsampling.

Here, the upper blue vertical dashes correspond to the original sample instants, and the lower red vertical dashes correspond to the desired interpolated instants. Observe that, being aligned at  $t = 0$ , the sequences realign at every  $y^{\text{th}}$  sample (alternatively, every  $x^{\text{th}}$  sample, if the interpolated times are taken as reference). Note that the aligned samples do not require calculations, as they are sent directly to the interpolator output. From Figure 6.12 it becomes clear why we should keep small numerator – it is responsible for the number of filters required to implement a single interpolation rate. Also observe that a single set of four samples can generate more than one interpolated sample, as occurred, e.g., in Figure 6.12(b) for the  $5^{\text{th}}$  and  $6^{\text{th}}$  samples (fractional intervals  $\mu_3$  and  $\mu_4$ ).

Thus, for our example, to support 11 symbol rates,  $(2-1)+(9-1)+(5-1)+(3-1)+(7-1)+(4-1)+(5-1)+(7-1)+(9-1)+(15-1) = 56$  4-tap complex FIRs should be used. A direct hardware implementation may employ a  $14 \times 4$  structure, where 14 in our example corresponds to  $x_{\text{max}} - 1$  (interpolation factor 15/14). For every  $i^{\text{th}}$  interpolation rate, a  $(x_i - 1) \times 4$  substructure is activated, and the corresponding filter weights are loaded from a lookup table (LUT). The complexity can be further reduced for more coarse approximations of the interpolation factors, as long as transients are avoided. Naturally, for hardware implementation, parallelization should be used to reduce circuit

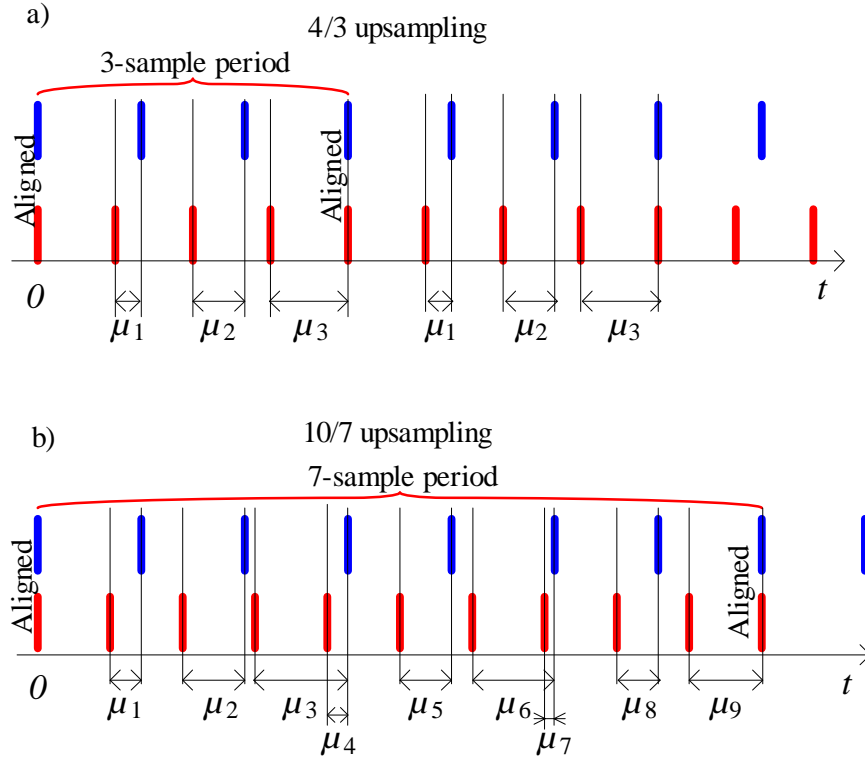


Figure 6.12: Interpolation of a single sample at  $t_\mu$  from four data samples by a 3<sup>rd</sup> order polynomial.

clock rate. Regardless of the particular design, the relative simplicity of the structure is evident, and should not impose serious challenges. The same considerations apply to the Rx interpolator, being a reciprocal structure.

An alternative implementation of multi-rate supporting Lagrange interpolators may rely on the, so called, *Farrow structures* [120], due to their ability to interpolate any fractional interval. Farrow structures are composed of  $M+1$  fixed FIR filters, where  $M$  is the order of interpolation polynomial. We have shown in Section 3.5.1 that weights of a FIR filter that implements a 3<sup>rd</sup>-order Lagrange interpolator are given by:

$$\begin{aligned}
 w_{-2} &= \frac{(\mu + 1)\mu(\mu - 1)}{6} = \frac{1}{6}\mu^3 - \frac{1}{6}\mu; \\
 w_{-1} &= \frac{(\mu + 1)\mu(\mu - 2)}{-2} = -\frac{1}{2}\mu^3 + \frac{1}{2}\mu^2 + \mu; \\
 w_0 &= \frac{\mu(\mu - 1)(\mu - 2)}{2} = \frac{1}{2}\mu^3 - \mu^2 - \frac{1}{2}\mu + 1; \\
 w_1 &= \frac{\mu(\mu - 1)(\mu - 2)}{-6} = -\frac{1}{6}\mu^3 + \frac{1}{2}\mu^2 - \frac{1}{3}\mu.
 \end{aligned} \tag{6.2}$$

Farrow structure implementation of Equation (6.2) is shown in Figure 6.13 (adapted from [121]). Observe that multiplication factors within each row of the structure correspond to the (vertically flipped) coefficients that multiply  $\mu^3 - \mu^0$  in Equation (6.2).

In this way, only different  $\mu$  values are stored in LUT, and not the filter weights.

The figure shows that 19 multiplications, out of which at least 16 are multiplications by constants (implemented as sums and shifts in hardware), and 15 additions per interpolated sample are required, which is doubtlessly an acceptable complexity increase. Further, 7 multiplications out of 19 are trivial (by 0, 1, or -1), and the multiplication by  $\mu$  can also be implemented as multiplication by constant, e.g., using multiplexers. Additionally, there have been demonstrated even more efficient Farrow structure implementations that explore filter coefficient symmetries [121].

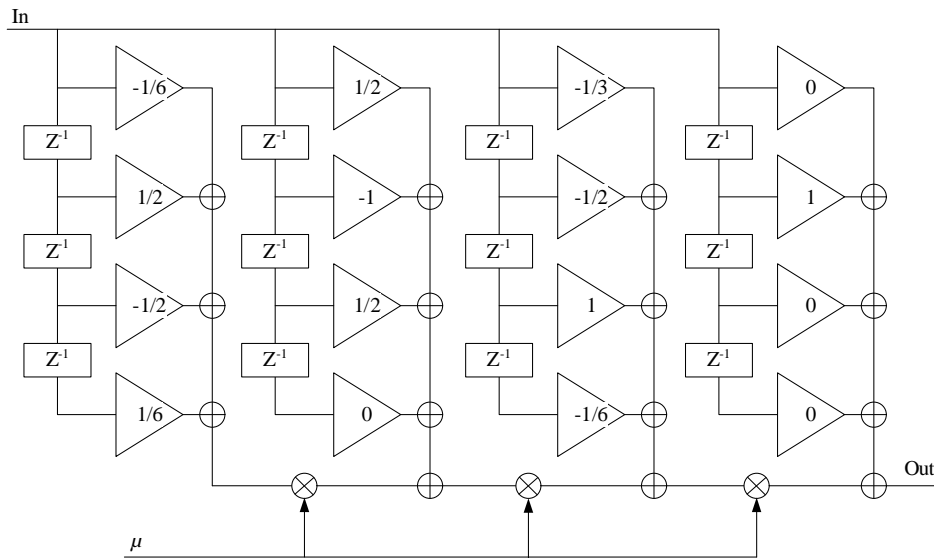


Figure 6.13: Farrow structure for 3<sup>rd</sup>-order polynomial interpolator (adapted from [121]).

## Chapter 7 CONCLUSION

This thesis targets the next-generation elastic optical networks, designed for more efficient use of the spectral resources, reduced capital and operational expenditures, and low power consumption. In the physical plane, adaptive transponders, capable of seamlessly adjusting their operation point according to the time-variable traffic and channel conditions, are highly attractive, as suggest numerous publications. In this scope we proposed two methods for online transmission rate switching, which constitute the major contributions of this thesis. The first method targets conventional transponders without transmit-side DSP capabilities, and is based on symbol repetition, with advanced receive-side equalizer structure. The second method targets more complex, transmit-side DSP-capable transponders, and is based on transmit- and receive-sides synchronous digital interpolators. In addition to rate switching, the methods also support dynamic bandwidth allocation features of elastic networks.

The first method was experimentally validated in a 100G PM-QPSK testbed and offline signal processing. We also conducted extensive computer simulations, including PM-QPSK and PM-16QAM modulation formats, to investigate its applicability to optically-generated NRZ, RZ and digitally-generated Nyquist pulse shapes. Error transients that appear at up-switching are successfully avoided by sufficiently long equalizer training periods (over 40,000 symbols). We also showed that the method is robust against PMD, and withstands the phase noise within acceptable limits. The key advantage of this method is that it allows to reduce DSP-associated power consumption by reducing CD-compensation-associated complexity. To estimate the potential complexity gain we conducted extensive computer simulations to determine the trade-offs between BER and frequency-domain CD compensation overlap size, for different pulse shapes and transmission rates. The results showed that halving the symbol rate allows to reduce about 55% in computational complexity due to longer sample periods and enhanced signal quality; and further reduction to quarter of the nominal symbol rate allows to completely bypass CD equalizer, with the exception of Nyquist pulses, where computational complexity can be reduced by  $\sim 80\%$ . Two limitations of hitless rate switching in conventional systems should be acknowledged. One limitation is the increased design complexity, due to dedicated equalizer branches for each supported transmission rate. Although the branches operate one at a time, still, the rate switching functionality would require larger chip area, with implications to packaging. Another

limitation is the relatively low granularity that the method offers. In this way, practical power savings would highly depend on the traffic pattern of a particular link.

The second method for Tx-side DSP-capable transponders was experimentally validated in a 100G PM-QPSK testbed using a digital-to-analog converter development kit. Unlike the first proposal, this method supports high granularity with marginal complexity increase (higher number of fractional interpolation intervals stored in a LUT). Experimental results for rate reduction/increase in ten discrete steps did not present error transients, yielding hitless transmission. The method can be used to reduce the DSP-related power consumption due to reduced data throughput after the receive-side interpolation. A great deal of additional power savings can be achieved in multiple FEC supporting transceivers by taking advantage of the increased signal quality at lower-than-nominal symbol rates, and switching to lower complexity FEC schemes. An important limitation of this method is that the rate adjustment cannot be exploited to reduce CD-compensation-associated power consumption, as in the previous case.

To make the proposed schemes suitable for physical implementation, much additional research is required. First and foremost, client- and line-side transport/network protocols must be extended to support online rate switching. Secondly, a Tx-Rx synchronization mechanism must be created, so that the receive-side is aware of the exact rate switching instants, to modify signal processing accordingly. Here, an inter-layer approach, that would allow to take advantage of the existing frame synchronization mechanisms, might be attractive. Additional adjustments are also required to avoid bouncing – a situation when client-side transmission rate oscillates around some threshold value, provoking rapid back and forth rate switching at the line-side. Finally, the rate switching scheme for Tx DSP-capable systems (second contribution) should be further improved to include reduction of CD-compensation-associated power, by placing the Rx interpolator prior to the CD equalizer. It is not clear what kind of adjustments in the DSP algorithms are required in this case to avoid transients and yield hitless transmission.

## Bibliography

- [1] AGRAWAL, G. *Fiber-Optic Communication Systems*. 3rd. Ed. : Wiley Interscience, 2002.
- [2] ITU-T Recommendation G.652. *Characteristics of a single-mode optical fibre and cable*. November 2009.
- [3] Corning<sup>®</sup> SMF-28<sup>®</sup> ULL Optical Fiber. *Product Information*. 2008.
- [4] DESURVIRE, E. et al. Science and technology challenges in XXI<sup>st</sup> century optical communications. *Comptes Rendus Physique*, v. 12, p. 387–416, April 2011.
- [5] RICHARDSON, D. J.; FINI, J. M.; NELSON, L. E. Space-division multiplexing in optical fibres. *Nature Photonics*, n. 7, p. 354–362, April 2013.
- [6] ESSIAMBRE, R.-J.; TKACH, R. Capacity trends and limits of optical communication networks. *Proceedings of the IEEE*, v. 100, n. 5, p. 1035–1055, May 2012.
- [7] ESSIAMBRE, R.-J. et al. Capacity limits of optical fiber networks. *Journal of Lightwave Technology*, v. 28, n. 4, p. 662 –701, February 2010.
- [8] MITRA, P. P.; STARK, J. B. Nonlinear limits to the information capacity of optical fibre communications. *Nature*, v. 411, p. 1027–1030, June 2001.
- [9] TUCKER, R. S. Green optical communications – Part I: Energy limitations in transport. *Journal of Selected Topics in Quantum Electronics*, v. 17, n. 2, p. 245–260, March 2011.
- [10] ITU-T Recommendation G.694.1. *Spectral grids for WDM applications: DWDM frequency grid*. February 2012.
- [11] GERSTEL, O. et al. Elastic optical networking: a new dawn for the optical layer? *IEEE Communications Magazine*, v. 50, n. 2, p. s12–s20, February 2012.
- [12] BOSCO, G. et al. On the performance of Nyquist-WDM terabit superchannels based on PM-BPSK, PM-QPSK, PM-8QAM or PM-16QAM subcarriers. *Journal of Lightwave Technology*, v. 29, n. 1, p. 53 – 61, January 2011.

- [13] CHOWDHURY, P. et al. On the design of energy-efficient mixed-line-rate (MLR) optical networks. *Journal of Lightwave Technology*, v. 30, n. 1, p. 130–139, January 2012.
- [14] ZHANG, Y. et al. Traffic grooming in spectrum-elastic optical path networks. In: *Optical Fiber Communication Conference*. 2011. p. 1–3.
- [15] CHRISTODOULOPOULOS, K.; TOMKOS, I.; VARVARIGOS, E. Time-varying spectrum allocation policies and blocking analysis in flexible optical networks. *Journal on Selected Areas in Communications*, v. 31, n. 1, p. 13–25, January 2013.
- [16] SHAKYA, S. et al. Spectrum allocation for time-varying traffic in elastic optical networks using traffic pattern. In: *Optical Fiber Communication Conference*. : Optical Society of America, 2014. p. W2A.58.
- [17] TAKAGI, T. et al. Disruption minimized spectrum defragmentation in elastic optical path networks that adopt distance adaptive modulation. In: *European Conference and Exhibition on Optical Communication*. 2011.
- [18] CUGINI, F. et al. Push-pull technique for defragmentation in flexible optical networks. In: *National Fiber Optic Engineers Conference*. : Optical Society of America, 2012. p. JTh2A.40.
- [19] STIAKOIANNAKIS, I. et al. Dynamic cooperative spectrum sharing and defragmentation for elastic optical networks. *Journal of Optical Communications and Networking*, v. 6, n. 3, p. 259–269, March 2014.
- [20] PERRIN, S. The need for next-generation ROADM networks. In: *JDSU White Paper*. 2010.
- [21] MUHAMMAD, A. et al. Cost-efficient design of flexible optical networks implemented by architecture on demand. In: *Optical Fiber Communications Conference*. 2014. p. 1–3.
- [22] AHMAD, A. et al. Switching node architectures in flexible-grid networks: A performance comparison. In: *International Conference on Optical Network Design and Modeling*. 2014. p. 49–54.
- [23] GRINGERI, S.; BITAR, N.; XIA, T. Extending software defined network principles to include optical transport. *IEEE Communications Magazine*, v. 51, n. 3, p. 32–40, March 2013.



- [24] MELLO, D. et al. Adaptive optical transceivers: Concepts and challenges. *Journal of Communication and Information Systems*, v. 29, n. 1, 2014.
- [25] SEDIGHI, B. et al. Power-efficiency considerations for adaptive long-haul optical transceivers. *Journal of Optical Communications and Networking*, Optical Society of America, v. 6, n. 12, p. 1093–1103, December 2014.
- [26] LIU, X.; CHANDRASEKHAR, S. High spectral-efficiency transmission techniques for systems beyond 100 Gb/s. In: *Signal Processing in Photonic Communications*. : Optical Society of America, 2011.
- [27] RIVAL, O.; VILLARES, G.; MOREA, A. Impact of inter-channel nonlinearities on the planning of 25–100 Gb/s elastic optical networks. *Journal of Lightwave Technology*, Optical Society of America, v. 29, n. 9, p. 1326–1334, May 2011.
- [28] RIVAL, O.; MOREA, A. Elastic optical networks with 25 x 100G format-versatile WDM transmission systems. In: *Optoelectronics and Communications Conference*. 2010. p. 100 –101.
- [29] YAMAZAKI, H.; GOH, T. Flexible-format optical modulators with a hybrid configuration of silica planar lightwave circuits and LiNbO<sub>3</sub> phase modulators. *NTT Technical Review*, NTT Photonics Laboratories, v. 9, n. 4, Apr. 2011.
- [30] CHOI, H. Y.; TSURITANI, T.; MORITA, I. BER-adaptive flexible-format transmitter for elastic optical networks. *Optics Express*, Optical Society of America, v. 20, n. 17, p. 18652–18658, August 2012.
- [31] FREUDE, W. et al. Software-defined optical transmission. In: *International Conference on Transparent Optical Networks*. 2011. p. 1–4.
- [32] GROBE, K. et al. Software-defined optics as solution for next-generation inter-data-center ultra-high-speed DWDM transport. In: *Terena Networking Conference*. 2012.
- [33] Center of Study and Research in Network Technology and Operations – CEPTRON, Brazil. Nov 2014. Available at: <<http://www.ptt.br/>>.
- [34] London Internet Exchange – LINX. June 2015. Available at: <<https://www.linx.net/pubtools/trafficstats.html>>.
- [35] SAVORY, S. J. Digital filters for coherent optical receivers. *Optics Express*, Optical Society of America, v. 16, n. 2, p. 804–817, 2008.

- [36] MOREA, A. et al. Datarate adaptation for night-time energy savings in core networks. *Journal of Lightwave Technology*, v. 31, n. 5, p. 779–785, 2013.
- [37] JINNO, M. et al. Elastic and adaptive optical networks: possible adoption scenarios and future standardization aspects. *IEEE Communications Magazine*, v. 49, n. 10, p. 164–172, 2011.
- [38] TROWBRIDGE, S. Ethernet and OTN: 400G and beyond. In: *Optical Fiber Communications Conference*. : Optical Society of America, 2015. p. Th3H.1.
- [39] ITU-T Recommendation G.7044/Y.1347. *Hitless adjustment of ODUflex(GFP)*. 2011.
- [40] SIMMONS, J. M. *Optical network design and planning*. 2nd. Ed. : Springer, 2014.
- [41] JINNO, M. et al. Spectrum-efficient and scalable elastic optical path network: architecture, benefits, and enabling technologies. *IEEE Communications Magazine*, v. 47, n. 11, p. 66–73, November 2009.
- [42] ITU-T Recommendation G.709/Y.1331. *Interfaces for the optical transport network*. February 2012.
- [43] ARABACI, M. et al. Nonbinary LDPC-coded modulation for rate-adaptive optical fiber communication without bandwidth expansion. *IEEE Photonics Technology Letters*, v. 24, n. 16, p. 1402–1404, August 2012.
- [44] GHO, G.-H.; KLAKE, L.; KAHN, J. Rate-adaptive coding for optical fiber transmission systems. *Lightwave Technology, Journal of*, v. 29, n. 2, p. 222–233, January 2011.
- [45] MELLO, D. et al. Optical networking with variable-code-rate transceivers. *Journal of Lightwave Technology*, v. 32, n. 2, p. 257–266, January 2014.
- [46] ZHANG, Z.; LI, C. Hitless multi-rate coherent transceiver. In: *Advanced Photonics*. : Optical Society of America, 2015. p. SpS3D.2.
- [47] BARROS, D. et al. Bandwidth-scalable long-haul transmission using synchronized colorless transceivers and efficient wavelength-selective switches. *Journal of Lightwave Technology*, v. 30, n. 16, p. 2646–2660, August 2012.
- [48] SHARIF, M.; KAHN, J. Variable-bandwidth superchannels using synchronized colorless transceivers. *Journal of Lightwave Technology*, v. 32, n. 10, p. 1921–1929, May 2014.

- [49] YAN, S. et al. Demonstration of real-time Ethernet to reconfigurable superchannel data transport over elastic optical network. In: *European Conference on Optical Communication*. 2014. p. 1–3.
- [50] PROAKIS, J.; MANOLAKIS, D. *Digital Signal Processing: Principles, Algorithms and Applications*. 3rd. Ed. : Prentice Hall, 1995.
- [51] RAMASWAMI, R.; SIVARAJAN, K. N. *Optical Networks: a Pratical Perspective*. 3rd. Ed. : Morgan Kaufmann Publishers, 2010.
- [52] CVIJETIC, M. *Optical Transmission Systems Engineering*. : Artech House, Inc., 2003.
- [53] LATHI, B. P. *Modern Digital and Analog Communication Systems*. 3rd. Ed. : Oxford University Press, 1998.
- [54] DREXLER, P.; FIALA, P. Optical fiber birefringence effects – sources, utilization and methods of suppression. In: YASIN S. W. HARUN, H. A. M. (Ed.). *Recent Progress in Optical Fiber Research*. : InTech, 2011. Chapter 7.
- [55] SHTAIF, M.; MECOZZI, A. Modelling of polarization mode dispersion in optical communications systems. In: GALTAROSSA, A.; MENYUK, C. R. (Ed.). *Polarization Mode Dispersion*. : Springer, 2005. Chapter 2.
- [56] PACHNICKE, S. *Fiber-Optic Transmission Networks: Efficient Design and Dynamic Operation*. : Springer-Verlag, 2012.
- [57] WADDY, D.; CHEN, L.; BAO, X. Theoretical and experimental study of the dynamics of polarization-mode dispersion. *IEEE Photonics Technology Letters*, v. 14, n. 4, p. 468–470, April 2002.
- [58] MENYUK, C.; MARKS, B. Interaction of polarization mode dispersion and non-linearity in optical fiber transmission systems. *Journal of Lightwave Technology*, v. 24, n. 7, p. 2806–2826, 2006.
- [59] GUIOMAR, F. P. F. *Digital Nonlinear Equalization for Optical Transmission Systems*. Thesis (PhD) — University of Aveiro, 2015.
- [60] YASSER, H. A. Polarization losses in optical fibers. In: YASIN, M.; HARUN, S. W.; AROF, H. (Ed.). *Recent Progress in Optical Fiber Research*. : InTech, 2011. Chapter 6.
- [61] SOLLER, B. J. Second-order PMD in optical components. *Luna Technologies, White Paper*, May 2005.

- [62] AGRAWAL, G. *Lightwave technology telecommunication systems*. : Wiley Interscience, 2005.
- [63] AGRAWAL, G. *Nonlinear Fiber Optics*. 3rd. Ed. : Academic Press, 2001.
- [64] WEINBERGER, P. John Kerr and his effects found in 1877 and 1878. *Philosophical Magazine Letters*, Taylor & Francis, v. 88, n. 12, p. 897–907, 2008.
- [65] SINGH, S. P.; SINGH, N. Nonlinear effects in optical fibers: Origin, management and applications. *Progress In Electromagnetics Research*, EMW Publishing, v. 73, p. 249–275, 2007.
- [66] KUMAR, S.; DEEN, M. J. *Fiber optic communications: fundamentals and applications*. : Wiley & Sons, 2014.
- [67] SERENA M. BERTOLINI, A. V. P. *Optilux Toolbox: User manual*. : University of Parma, 2009.
- [68] PEDDANARAPPAGARI, K.; BRANDT-PEARCE, M. Volterra series transfer function of single-mode fibers. *Journal of Lightwave Technology*, v. 15, n. 12, p. 2232–2241, December 1997.
- [69] CARENA, A. et al. Modeling of the impact of nonlinear propagation effects in uncompensated optical coherent transmission links. *Journal of Lightwave Technology*, v. 30, n. 10, p. 1524–1539, May 2012.
- [70] POGGIOLINI, P. The GN model of non-linear propagation in uncompensated coherent optical systems. *Journal of Lightwave Technology*, v. 30, n. 24, p. 3857–3879, December 2012.
- [71] HO, K.-P. *Phase-Modulated Optical Communication Systems*. 1st. Ed. : Springer Science and Business Media, 2005.
- [72] IP, E.; KAHN, J. Digital equalization of chromatic dispersion and polarization mode dispersion. *Journal of Lightwave Technology*, v. 25, n. 8, p. 2033–2043, August 2007.
- [73] ITU-T Recommendation G.810. *Considerations on timing and synchronization issues*. November 1988.
- [74] MOLER, C. *Numerical Computing with Matlab*. Mathworks, online Ed., 2004. Available at: <<http://www.mathworks.com/moler/chapters.html>>.

- [75] FATADIN, I.; SAVORY, S.; IVES, D. Compensation of quadrature imbalance in an optical QPSK coherent receiver. *IEEE Photonics Technology Letters*, IEEE, p. 1733–1735, 2008.
- [76] BARRY, J. R.; MESSERSCHMITT, D. G.; LEE, E. A. *Digital Communication*. 3rd. Ed. : Kluwer Academic Publishers, 2003.
- [77] DINIZ, J. C. et al. Hardware-efficient chromatic dispersion estimator based on parallel Gardner timing error detector. In: *Optical Fiber Communication Conference*. : Optical Society of America, 2013.
- [78] GARDNER, F. M. A BPSK/QPSK timing-error detector for sampled receivers. *IEEE Transactions on Communications*, v. 34, n. 5, p. 423–429, May 1986.
- [79] ZHOU, X. et al. All-digital timing recovery and adaptive equalization for 112 Gbits/s POLMUX-NRZ-DQPSK optical coherent receivers. *Journal of Optical Communications and Networking*, Optical Society of America, v. 2, n. 11, p. 984–990, 2010.
- [80] KUSCHNEROV, M. et al. Adaptive chromatic dispersion equalization for non-dispersion managed coherent systems. In: *Conference on Optical Fiber Communication*. 2009. p. 1–3.
- [81] XIE, C. Chromatic dispersion estimation for single-carrier coherent optical communications. *IEEE Photonics Technology Letters*, v. 25, n. 10, p. 992–995, May 2013.
- [82] SUI, Q.; LAU, A.; LU, C. Fast and robust blind chromatic dispersion estimation using auto-correlation of signal power waveform for digital coherent systems. *Journal of Lightwave Technology*, v. 31, n. 2, p. 306–312, January 2013.
- [83] MEYR, H.; MOENECLAHEY, M.; FECHTEL, S. A. *Digital communication receivers: synchronization, channel estimation and signal processing*. 2nd. Ed. : John Wiley & Sons, 1998.
- [84] Technical Presentation. Analyzing digital jitter and its components. In: *High-Speed Digital Design Seminar*. Agilent Technologies, 2004. Available at: <[www.keysight.com/upload/cmc\\_upload/All/Analyzing\\_Digital\\_Jitter\\_and\\_its\\_Components.pdf](http://www.keysight.com/upload/cmc_upload/All/Analyzing_Digital_Jitter_and_its_Components.pdf)>.
- [85] GARDNER, F. Interpolation in digital modems. I. Fundamentals. *IEEE Transactions on Communications*, v. 41, n. 3, p. 501–507, March 1993.

- [86] STOJANOVIC, N. et al. Timing recovery in Nyquist coherent optical systems. In: *Telecommunications Forum – TELFOR*. 2012. p. 895–898.
- [87] STOJANOVIC, N. et al. Modified Gardner phase detector for Nyquist coherent optical transmission systems. In: *Optical Fiber Communication Conference*. 2013. p. 1–3.
- [88] ERUP, L.; GARDNER, F. M.; HARRIS, R. Interpolation in digital modems – Part II: Implementation and performance. *IEEE Transactions on Communications*, v. 41, n. 6, p. 998–1008, Jun 1993.
- [89] PASKOV, M.; LAVERY, D.; SAVORY, S. Blind equalization of receiver in-phase/quadrature skew in the presence of Nyquist filtering. *IEEE Photonics Technology Letters*, v. 25, n. 24, p. 2446–2449, December 2013.
- [90] RIOS-MULLER, R.; RENAUDIER, J.; CHARLET, G. Blind receiver skew compensation and estimation for long-haul non-dispersion managed systems using adaptive equalizer. *Journal of Lightwave Technology*, v. 33, n. 7, p. 1315–1318, April 2015.
- [91] BOTTOU, L. Online learning and stochastic approximations. *On-line learning in neural networks*, Cambridge University Press, v. 17, n. 9, p. 25, 1998.
- [92] MANOLAKIS, D.; INGLE, V.; KOGON, S. *Statistical and Adaptive Signal Processing: Spectral Estimation, Signal Modeling, Adaptive Filtering and Array Processing*. : Artech House, 2005.
- [93] NEVES, A. et al. Sobre critérios para equalização não-supervisionada. *Controle & Automação*, Sociedade Brasileira de Automatica, v. 17, n. 3, September 2006.
- [94] WINZER, P. et al. Spectrally efficient long-haul optical networking using 112-Gb/s polarization-multiplexed 16-QAM. *Journal of Lightwave Technology*, IEEE, v. 28, n. 4, p. 547–556, 2010.
- [95] GODARD, D. N. Self-recovering equalization and carrier tracking in two-dimensional data communication systems. *IEEE Transactions on Communications*, IEEE, v. 28, n. 11, p. 1867–1875, 1980.
- [96] TREICHLER, J.; AGEE, B. A new approach to multipath correction of constant modulus signals. *IEEE Transactions on Acoustics, Speech and Signal Processing*, v. 31, n. 2, p. 459 – 472, April 1983.

- [97] JOHNSON R., J. et al. Blind equalization using the constant modulus criterion: a review. *Proceedings of the IEEE*, v. 86, n. 10, p. 1927–1950, October 1998.
- [98] SETHARES, W.; REY, G.; JOHNSON, C. Approaches to blind equalization of signals with multiple modulus. In: *International Conference on Acoustics, Speech, and Signal Processing*. 1989. p. 972–975 vol.2.
- [99] READY, M.; GOOCH, R. Blind equalization based on radius directed adaptation. In: *International Conference on Acoustics, Speech, and Signal Processing*. 1990. p. 1699–1702 vol.3.
- [100] GARCIA, F. A.; MELLO, D. A.; WALDMAN, H. Feedforward carrier recovery for polarization demultiplexed signals with unequal signal to noise ratios. *Optics Express*, Optical Society of America, v. 17, n. 10, p. 7958–7969, May 2009.
- [101] SAVORY, S. J. et al. Electronic compensation of chromatic dispersion using a digital coherent receiver. *Optics Express*, OSA, v. 15, n. 5, p. 2120–2126, 2007.
- [102] PFAU, T.; HOFFMANN, S.; NOE, R. Hardware-efficient coherent digital receiver concept with feedforward carrier recovery for M-QAM constellations. *Journal of Lightwave Technology*, v. 27, n. 8, p. 989–999, April 2009.
- [103] LI, J. et al. Laser-linewidth-tolerant feed-forward carrier phase estimator with reduced complexity for QAM. *Journal of Lightwave Technology*, v. 29, n. 16, p. 2358–2364, August 2011.
- [104] GUIOMAR, F. et al. Parallel split-step method for digital backpropagation. In: *Optical Fiber Communications Conference*. 2015. p. 1–3.
- [105] LI, L. et al. Implementation efficient nonlinear equalizer based on correlated digital backpropagation. In: *Optical Fiber Communication Conference*. 2011. p. 1–3.
- [106] PARAHYBA, V. et al. Performance against implementation of digital backpropagation for high-speed coherent optical systems. *Electronics Letters*, v. 51, n. 14, p. 1094–1096, 2015.
- [107] LI, X. et al. Electronic post-compensation of WDM transmission impairments using coherent detection and digital signal processing. *Optics Express*, Optical Society of America, v. 16, n. 2, p. 880–888, January 2008.
- [108] ROSA, E. S. et al. Nonlinear effects compensation in Optical Coherent PDM-QPSK Systems. *Journal of Microwaves, Optoelectronics and Electromagnetic Applications*, Scielo, v. 12, p. 707 – 718, 12 2013.

- [109] SPINLER, B. Equalizer design and complexity for digital coherent receivers. *Journal of Selected Topics in Quantum Electronics*, v. 16, n. 5, p. 1180–1192, September 2010.
- [110] SHIEH, W.; ATHAUDAGE, C. Coherent optical orthogonal frequency division multiplexing. *Electronics Letters*, v. 42, n. 10, p. 587–589, May 2006.
- [111] KUDO K. ISHIHARA, T. K. R.; TAKATORI, Y. Frequency domain equalization design for coherent optical single carrier transmission. *NTT Technical Review*, v. 8, n. 7, 2010.
- [112] XU, T. et al. Chromatic dispersion compensation in coherent transmission system using digital filters. *Optics Express*, Optical Society of America, v. 18, n. 15, p. 16243–16257, July 2010.
- [113] FARIA, A. et al. Comparative analysis of power consumption in the implementation of arithmetic algorithms. In: *International Conference on Trust, Security and Privacy in Computing and Communications*. 2011. p. 1247–1254.
- [114] BLAHUT, R. *Fast Algorithms for Signal Processing*. : Cambridge University Press, 2010.
- [115] GEYER, J. C. et al. Efficient frequency domain chromatic dispersion compensation in a coherent Polmux QPSK-receiver. In: *Optical Fiber Communications Conference*. 2010.
- [116] ITU-T Recommendation G.975.1. *Forward error correction for high bit-rate DWDM submarine systems*. 2004.
- [117] AGAZZI, O. Design trade-offs in practical ASIC implementations. In: *Optical Fiber Communications Conference*. 2015. p. Th1B.3.
- [118] Optical Internetworking Forum (OIF). *Multisource Agreement for 100G Long-Haul DWDM Transmission Module – Electromechanical*. June 2010.
- [119] SAVORY, S. J. Digital coherent optical receivers: Algorithms and subsystems. *IEEE Journal of selected topics in quantum electronics*, IEEE, v. 16, n. 5, p. 2120–2126, 2010.
- [120] FARROW, C. A continuously variable digital delay element. In: *IEEE International Symposium on Circuits and Systems*. 1988. p. 2641–2645 vol.3.



- [121] SHIUE, M.-T.; WEY, C.-L. Efficient implementation of interpolation technique for symbol timing recovery in DVB-T transceiver design. In: *IEEE International Conference on Electro/information Technology, 2006*. 2006. p. 427–431.